A MECHANO-CHEMICAL COMPUTATIONAL MODEL OF DEEP VEIN THROMBOSIS

FOR MSc THESIS

WRITTEN BY:

QUDUS BOLUWATIFE JIMOH-TAIWO

SUPERVISED BY:

Dr MALEBOGO NGOEPE

SUBMITTED ON:

14/03/2021

PLAGIARISM DECLARATION

I, Qudus Boluwatife Jimoh-Taiwo hereby declare that this thesis is based on my original work except which is properly acknowledged. I declare that I understand the meaning of plagiarism and its consequences. I understand that neither the whole work nor part of has been, is being or will be submitted for another degree. I confirm I have the consent of my supervisor to submit this thesis as any concerns that might arise has been resolved.

I have applied the IEEE referencing style in this thesis. I give the university the right to reproduce the whole or part of this thesis for research.

Signature: . Signed by candidate …

Date: ……14/06/2021……

ABSTRACT

Deep Vein Thrombosis (DVT) is the formation of a blood clot in a vein, usually in the body's lower extremities. If untreated, DVT can lead to pulmonary embolism (PE), heart attack and/or stroke, which can be fatal. According to literature, DVT affects 0.2% of people in developed countries and about 0.3%-1% in developing countries. In the past, various computational models of DVT were developed. Most models account for either the mechanical factors or biochemical factors involved with DVT. Developing a model that accounts for both factors will improve our understanding of the coagulation process. This study developed a three-dimensional DVT computational model in idealized and realistic common femoral vein (CFV) geometries. The model considers the biochemical reactions between thrombin and fibrinogen, pulsatile blood flow, and clot growth within the vessel. The model was validated using a simplified experimental setup with flow, thrombin, and fibrinogen.

Computational fluid dynamics (CFD) simulations were carried out using the ANSYS modelling suite. The Navier-Stokes equations were solved to determine the fluid flow. Based on a clinical dataset of pulsatile blood flow, the laminar flow of blood with a Poiseuille velocity profile was applied at the inlet. Darcy's law was used to account for porosity changes in the clot, with the clot represented by zones with lower porosities. The transport equations were used for changes in the concentration of the biochemical protein species. Thrombin was released into the bloodstream from an injury zone on the wall of the vein. The Michaelis-Menten equation was used to represent the conversion of thrombin and fibrinogen to fibrin, the final product of the coagulation process. The computational model solves the blood flow pattern proximally, locally, and distally to clot formation at the injury zone. The model also predicts the size of the clot and the rate of clot growth.

The model was first developed in a two-dimensional geometry. This model was used to investigate clot formation under different cases comparing how introducing thrombin as a flux value differs from specifying it as a fixed concentration. It was confirmed that to apply the flux condition, the thrombin concentration needs to be divided by a factor derived by multiplying the area of the injury zone and the time step size. The same model was then used to conduct a parametric study to determine the effects of varying parameters such as inlet velocity, vein diameter, and peak thrombin concentration on the size and shape of clot formed. Peak thrombin concentration was the key factor driving the initiation and propagation of clot in the vein.

The model was then extended to an idealized three-dimensional geometry. This computational model was validated using results from an experimental clot growth study. The experiment comprised a steady flow of fibrinogen in a cylindrical pipe, with an injection of thrombin into the flow at the injury site, resulting in fibrin formation. A qualitative comparison was then made between the experimental clot and the clot formed *in silico*. Although quantitative measurements were not made, there were similarities in the shapes and sizes of the clots. The validated computational model was used to compare

clot formation under steady and pulsatile flow conditions. Realistic clot growth was observed and compared to the steady flow condition. It was found that a larger clot formed under pulsatile conditions. Clot formation with the presence of valve activity was also investigated. The effect of opening and closing of the valves was achieved by varying the blood flow diameter at the inlet instead of modelling the valves as solid walls and accounting for the leaflet movement by solving the governing equations for the fluid-solid interaction (FSI), as used in existing models.

The model was then applied to a patient-specific geometry. Realistic clot growth was achieved using this model, and the clot was compared to a clot formed *in vivo*, as depicted in the original imaging scan. The model helps us better understand the clot growth process in the femoral vein on a patient-specific level. It also shows that the presence of venous valves increases the size of clot formed compared to steady flow. However, the high strain rate present makes the clot formed smaller than in standard pulsatile flow cases.

ACKNOWLEDGEMENTS

I would first and foremost like to give thanks to almighty Allah for granting me life and making the completion of this research possible. Alhamdulillah for ensuring the progress and success of this work.

I would then like to give thanks to my supervisor, A/Prof Malebogo Ngoepe for your support, guidance and encouragement over the course of the study. I appreciate you for giving me the opportunity to achieve this feat, your patience and insight throughout the project are sincerely appreciated. I cherish your motivation and will to help complete such an interesting topic.

I would like to say thank you to the University of Cape Town EBE staffs. Sincere appreciation also goes to Denise Botha for your assistance, guidance and support with the multiple administrative issues I had during my program.

Thank you to the National Research Foundation University Research Committee for making my research possible. Your generous financial support made the last year a dream come true.

Thanks to the University of Cape Town's ICT High-Performance Computing Team for granting me access to the cluster. Special thanks go to Andrew Lewis for your help and guidance through the process.

A huge thank you to my friends and colleagues for your constant support, understanding and assistance. Thank you to my flatmates at Flat 10 Orpington House for being there for me through this process. A special thank you to Bruno Fernandes for giving me 18 reasons to believe in a better future.

Finally, I would like to sincerely thank my family for your love, prayers, and encouragement. Thank you my beautiful wife Lateefah, for standing by me as we went through this process. To my parents, my brothers Yusuf, Faruq and Adam, thank you for keeping me grounded, for reminding me only Allah can make thing possible. I appreciate the love you have shown me.

CONTENTS

LIST OF FIGURES

LIST OF TABLES

ACRONYMS AND ABBREVIATIONS

DVT	Deep vein thrombosis
PE	Pulmonary embolism
CFV	central femoral vein
OCP	Oral contraceptive pill
VTE	venous thromboembolism
CFD	computational fluid dynamics
FEM	finite element method
FSI	fluid-solid interactions
FVM	finite volume method
PIV	Particle Image Velocimetry
CT	Computed tomography
MRI	magnetic resonance imaging
HIV	human immunodeficiency virus
IVC	Inferior Vena Cava
UFH	unfractionated heparin
LMWH	low-molecular-weight heparins
INR	international normalized ratio
GCS	graduated compression stocking
IPC	intermittent pneumatic compression
TF	Tissue Factor
PT	prothrombin time
aPTT	activated partial thromboplastin times
vWF	von Willebrand factors
GE	governing equation
ODE	ordinary differential equations
ADP	Adenosine diphosphate
3-D	Three dimensional
CDR	convection-diffusion-reaction
NS	Navier Stoke's
DPD	dissipative particle dynamics
CPM	Cellular Potts model
SDPD	smooth dissipative particle dynamics
AMG	algebraic multigrid
PRESTO	PREssure Staggering Option

PISO	pressure-implicit with splitting of operators
FAS	full approximation storage
UDS	User-defined scalar
UDF	User-defined function
CAT	calibrated automated thrombogram
ETP	endogenous thrombin potential
TTP	time to peak
TAMV	time-averaged maximum flow velocity
GIT	grid independence test

1. INTRODUCTION

This chapter gives a brief introduction to the research performed in this work by providing background on deep vein thrombosis and thromboembolism and how they affect South Africa's social and economic wellbeing. The application of computational fluid dynamics for clinical imaging is also discussed. Finally, the chapter summarises the research's objectives, scope and plan of development of the thesis.

1.1. Background

Deep vein thrombosis (DVT) is the formation of blood clots within the deep veins, and usually occurs in the veins of the leg, but can sometimes occur in the arms and in the mesenteric or cerebral veins [1]. Deep vein thrombosis is a common medical problem. Vessel endothelium injury exposes the subendothelial layer, promoting blood clot formation and reducing the venous blood flow. In severe cases, the blood clot, known as a thrombus, can break loose from the deep vein and travel through the bloodstream. The dislodged clot, or embolus, can get trapped in the smaller vessels leading to thromboembolic disease such as pulmonary embolism (PE). PE is a major concern and can be fatal [2].

Globally, about 10 million DVT cases occur yearly, thereby making venous thromboembolism the third most common vascular disease after acute myocardial infarction and stroke [3]. Over 200,000 people suffer from DVT in South Africa each year. Due to most DVT's mysterious nature, the actual incidence is unknown, and about 60% of DVT cases lead to embolism. The incidence of venous thromboembolism increases with age for both genders. The incidence rate increases exponentially to about 1 in 100 for people older than 80 years. From 45 years onwards, the risk of developing DVT is 8% [4]. The risk does not differ significantly by sex, although it is prevalent in women particularly in cases of pregnancy and OCP [3]. Compared to people of European descent, the incidence is higher amongst people of African descent and lower amongst people of Asian descent. The cause of this is yet to be discovered [5]. About 20% of the time, patients die from PE before diagnosis or shortly after the incident, especially if the embolism is related to haemodynamic instability. In the long term, 30% of all patients with venous thromboembolism (VTE) have a recurrence within ten years [3].

The Department of Statistics South Africa (Stats SA) found that thromboembolic disease is responsible for 20,000 deaths every year in South Africa [6]. Little research has been done to quantify the economic impact of DVT on South Africa, but it is predicted to be enormous as shown in a review conducted in high-income countries illustrating the economic impact on the healthcare system. Cushman *et al.* focused on determining DVT incidence in two groups of people in the United States [7]. It was found that the incidence of first-time DVT was 1.92 per 1000 persons per year. Dealing with VTE costs the United States about 7 to 10 billion dollars, majorly spent on the initial diagnosis and treatment of VTE treatment and managing recurrent hospitalization [8].

It is vital to develop improved methods to effectively diagnose and treat DVT patients if the cost, both socially and financially, can be mitigated. In the case of early diagnosed DVT, developing methods that predict embolism occurrence will also be vital. Clot formation during DVT is based on the flow and biochemical properties of blood in the vein. With the introduction of computational fluid dynamics (CFD) into biological and haemodynamic studies, these properties can be simulated to create models. These models have a high potential for improving the information available to clinicians when they are applied to a patient-specific case. Drug testing is another potential avenue for CFD model development, where anticoagulants could be tested on the models to estimate their effect on different patients [9].

Attempts to model DVT using CFD have met a level of success. Many of these models made significant assumptions to either simplify the model or reduce the computational expense to achieve this. One of the major assumptions made is that blood flow in the vein is steady as a simplification of the pulsatile flow. Although this assumption has been proven to be acceptable to a degree regarding the clotting outcomes, there is a need to investigate further how this assumption affects the initiation and propagation of clot growth under flow. Another assumption made in previous models is that the complex coagulation process can be accounted for solely by the thrombin concentration. In this case, a clot is said to form when thrombin concentration exceeds a threshold value. There has been no research addressing the effect of this assumption on the clotting process in DVT.

Most of the *in silico* DVT models are flow-based. They usually predict clot formation from stagnation or vortices in the flow. Stagnation might result from the vein's complex geometry or the presence of a valve in that area. Few models have predicted clot formation considering the biochemical reactions under complex flow, and none of the models has taken the effect of the venous valves on flow into account. To fully understand the clotting process and justify these assumptions, there is a need to consider these features in a single model and compare the clot formed to existing models.

1.2. Objectives

The main objective of this research is to develop a computational fluid dynamics model of DVT that can be applied to a patient-specific geometry. For the development of the model, the patient-specific geometry, velocity, pressure, and biochemical data are derived from literature. Data derived using clinically accessible techniques are considered to make the model accessible to clinicians. The complex coagulation process is simplified and represented by the reaction between thrombin and fibrinogen, resulting in fibrin production. The clot formed will be simulated as porous media. The model should produce relevant and understandable results that are capable of providing clinicians with an insight into the clot formation process in this pathology. The model will produce the size and shape of the clot formed under different physical and biochemical conditions. The developed model is then to be used to carry out the following studies:

- Investigation of the clot formation process differences when thrombin is introduced into the flow as a flux value versus a fixed concentration.
- A parametric study of the blood velocity, peak thrombin concentration and vein geometry to understand which parameter has the most significant effect on clot size and the effects of changing these parameters on the initiation and propagation of clot.
- Comparison of the clot formation, under steady and pulsatile flow conditions, in an idealized 3-dimensional geometry, which also examines the effect of valve activity on blood flow.
- Comparison of clot formation between idealised and patient-specific geometries
- Validation of computational results with the outcomes of an experimental clot growth study.

1.3. Scope of Research

This work's overall scope is to develop a CFD model that simulates clot formation applying a simplified coagulation cascade. The code simulating the boundary conditions could be re-written into any chosen programming language, and the numerical simulations can be performed on any commercial CFD software package that can solve for laminar flow and species transport and reaction.

Simpleware ScanIP (Synopsys, California, United States) was used for image segmentation [10]. Plot Digitizer and Python 3.8.5 were used for data processing, ANSYS Meshing (19.2 Academic License) for finite volume meshing, numerical simulation and post-processing. Also, the extraction and compilation of the data used by the numerical solver (ANSYS Fluent) are not automated in this project. These processes required manual input for each case.

The data used in this project are derived from literature. The project acknowledges that there are different methods used in literature by which the data could be obtained. However, the model was designed to take its velocity data from echocardiography and Computed tomography (CT) scans. The thrombin data is derived from thrombogram measurements, and other constants used are from experimental procedures found in literature. The patient-specific geometries were derived from Radiopedia.org (Radiopaedia Australia Pty Ltd)[11]. The modalities considered were CT scans and magnetic resonance imaging (MRI).

A grid independence study was carried out to obtain adequate refinement of the mesh. However, the analysis of different meshing techniques was out of the scope of the project. A parametric study was carried out varying the velocity, geometry, and biochemical concentrations. The parametric study considers how these parameters affect the initiation and propagation of the clot. The porosity and permeability of the clotted region are derived from literature. Other parameters that might affect clot formation were not considered in this parametric study.

Before applying on a patient-specific geometry, the model was developed and tested on an idealised geometry, assuming that the wall of the vessels is rigid, and flow is Newtonian. This work acknowledges

various numerical schemes and solvers, but this project was constrained to those offered by ANSYS Fluent.

The model was used to compare the size and shape of the clot formed under varying flow and biochemical conditions. The initiation time and propagation period of the clot were also investigated. Other properties of the clot were not considered in this project. The coagulation process included two reactions between three biochemical species (thrombin, fibrin and fibrinogen). While coagulation is a much more complex process, these are the essential proteins that result in fibrin mesh formation. In literature, venous valves are modelled as physical structures using fluid-structure interaction (FSI). However, in this project, the valve activity was modelled by simulating the valve's effect on the flow at the inlet. Finally, the results that are obtained are validated with an experimental clot growth study.

1.4. Plan of Development

The report begins by giving a background on DVT, its pathophysiology and the available treatment techniques. It then describes the coagulation process and the different approaches to its modelling, in literature. The implementation of CFD numerical modelling in haemodynamic studies is then discussed and CFD models of both the coagulation process and DVT are presented. The review of these models is presented and informs the model development methodology. The report then describes the fundamental theoretical principles that are needed for numerical modelling and simulations. The report also describes the experimental methodology taken to run these simulations and the clot growth study.

The model is then used to study the flux vs fixed concentration relationship and the results are presented. The procedures and results of the parametric study are then described. The results are discussed in light of other findings in the literature. The report then describes the need for advancement in the complexity of the model. The features added to the model are discussed and the clot formation process is investigated. The model is then applied to a patient-specific geometry and the results are presented. The material needed and procedures for the experimental clot growth study are described and the result of the experiment is compared to the computational results. Finally, the conclusion of the study are presented and recommendations for future works are proposed.

2. LITERATURE REVIEW

This chapter gives an overview of the background of deep vein thrombosis, its pathophysiology and the treatment techniques available. It also discusses the need for computational modelling of deep vein thrombosis. The chapter then investigates coagulation and deep vein thrombosis experimental and computational models developed in literature to inform the model development methodology.

2.1. Deep Vein Thrombosis

2.1.1. Overview

DVT must not be confused with the natural clotting process known as haemostasis, or superficial thrombophlebitis which affects the superficial veins. The distinction is essential, as a thrombus in the superficial veins does not carry the risk of embolism. An exception to this is when the vein segment affected is close to a junction with a deep vein. These cases are treated in the same way as deep vein thrombosis because of the risk of extension into the deep system [12].

2.1.2. Vein of the Legs

Veins are essential parts of the human body. Buescher *et al.* explained that the veins in the legs could be considered as long thin collapsible tubes containing a series of one-way bicuspid valves [13]. The vein's primary function is to return deoxygenated blood to the heart. There are two major types of veins: the superficial and deep veins shown in Figure 2.1. The superficial veins are just under the layer of the skin and are visible (green colour) while the deep veins are deep inside the muscle tissue. Perforating veins connect the superficial veins to the deep veins. The deep veins of the legs are well covered and supported by the muscle tissues around them. These veins produce between 90 and 95% of the blood outflow from the leg [14] [15].

The flow in the deep veins occurs with the help of the vein valves and the leg muscles. The muscles compress the vein and help the blood flow against gravity and the valves restrict the flow in the opposite direction. During the muscle’s contraction, the pressure in the veins increases forcing blood flow against gravity. When the muscles relax, the blood tends to flow backwards, so the valves come closer and form a seal. The venous valves eliminate the retrograde flow of blood; hence they are unidirectional valves [15]. There are two types of valves namely parietal and ostial valves. Parietal valves are the most common in the human body. Parietal valves are also known as pocket valves and contain cusps, the valvular agger, cornua and sinus. Ostial valves are found in the intersections where small veins transform into a large vein [16].

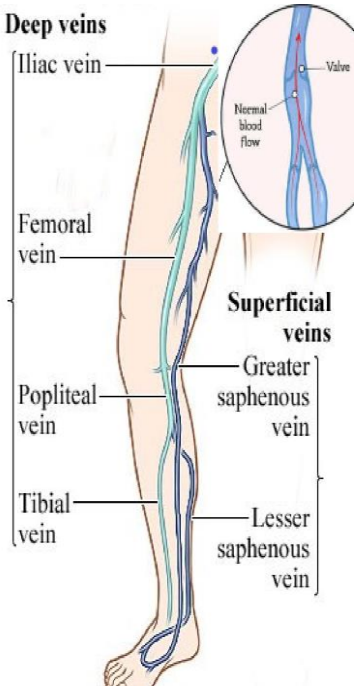

Figure 2.1: Veins of the legs [17].

The superficial femoral and popliteal veins in the thighs and the peroneal and tibial veins in the calves are commonly affected by DVT. Calf vein DVT possesses less risk of forming large emboli but can grow to the proximal thigh vein and cause PE [15]. The earliest formation of valves in the vein was seen in embryos at about 3.5 months. Parimi claimed that over 80% of the total body's vein valves are non-existent in a 70 years old adult[15]. The reduction can be due to thromboses of the vascular sinus which occurs frequently. Valves furthermore do not just disappear, but rather become impotent as the age increases due to over dilation of the venous wall.

2.1.3. Risk Factors of DVT

Almost half of the venous thromboembolism cases recorded in the past decade's research do not have identifiable environmental factors and are classified as unprovoked. The rest of the cases are provoked by transient or persistent factors that increase the risk of venous thromboembolism [3], [18]–[20].

In South Africa, the most common risk factors are HIV and tuberculosis, accounting for 51.85% and 35.80%, respectively. Other risk factors observed were smoking (25.93%), recent hospitalisation (34.57%), previous DVT (19.75%) and congestive cardiac failure (18.52%) [8]. Thrombophilia had a low percentage of occurrence in the study therefore an explanation was not established [21].

There is an association between multiple long-distance air flights and DVT. A study was carried out in New Zealand on 1000 subjects who travelled for at least 10 hours with a mean total duration of 39 hours. It was discovered that 1.4% of the subjects had DVT using radiological assessment [22]. A case-control study found that a significant proportion of the population undertaking long-haul flights tends to be younger and fitter than the general population, reducing the risk [23].

Hospital patients are recognized to be at risk of developing DVT. It is well established that patients undergoing surgery are at higher risk [23]. The thrombotic risk level depends on the type of surgery and the presence of additional risk factors. Orthopaedic surgeries, major vascular surgeries and neurosurgeries carry high risk (up to 25%). The likelihood of postoperative thrombosis is increased by factors such as advanced age, obesity, previous thrombosis, cancer and comorbid medical disorders [2] [24].

Thrombophilia is generally inherited and is detected in about 50% of patients diagnosed with spontaneous thrombosis. It involves distinct abnormalities in the coagulation system. DVT risk can increase when a patient is exposed to temporal risk factors such as surgeries, trauma and pregnancy. Pregnancy, in general, also increases the risk of DVT. This risk is due to a combination of immobility, hormonal effects and the compression of the Inferior Vena Cava (IVC) and iliac veins. The increased risk is noticeable in the first trimester and has a value of approximately 0.13%. Hormonal causes of DVT are also present in individuals who utilise oestrogen-containing Oral Contraceptive Pills (OCP), which have been seen to double the DVT risk. This risk tends to be attenuated since OCP consumers are young and fit but critical to consider when coupled with other risk factors [23] [25].

2.1.4. Detection and Diagnosis of DVT

The ability to detect DVT is essential, especially in cases that might lead to PE. Oedema is the accumulation of fluid in intercellular tissue resulting from an abnormal expansion in fluid volume. Limb oedema is the swelling of the lower legs or hands. To detect DVT, a physical examination is performed on the limb to check if the limb oedema is unilateral or bilateral, if the skin of the affected area is red or hot, and if the veins are dilated. The tenderness of the area and the presence of pain in the area is examined as well [1]. Clinical diagnosis of DVT is unreliable, and therefore, clinical probability scores have been developed to increase the effectiveness of diagnosis [23]. Wells *et al.* developed the most widely used model for clinical probability prediction for DVT. The predictive features and their scores are indicated in

Table 1. The Wells' score is widely used for its high sensitivity (77-98%) [26].

If a patient is suspected of having DVT, more advanced diagnostic techniques are applied. Two primary diagnostic techniques can detect DVT and PE, namely an invasive and non-invasive technique. The invasive technique involves making an incision to access the affected region. This technique might be painful and sometimes affects previously unaffected areas. The non-invasive technique involves accessing the affected area only without affecting other parts [15]. The application of non-invasive techniques has improved the process of detecting DVT in patients as they are rapid and cost-effective [2], [27], [28].

Table 1: Clinical model developed by Wells et al., for predicting pre-test probability for DVT. The corresponding scores are added when the features are present [27].

Clinical Feature	**Score**
Active cancer (treatment ongoing or within previous 6 months or palliative)	1
Paralysis, paresis, or recent plaster immobilisation of the lower extremities	1
Recently bedridden for more than 3 days or major surgery, within 4 weeks	1
Localised tenderness along with the distribution of the deep venous system	1
Entire leg swollen	1
Calf swelling by more than 3 cm when compared with the asymptomatic leg (measured 10 cm below tibial tuberosity)	1
Pitting oedema (more significant in the symptomatic leg)	1
Collateral superficial veins (non-varicose)	1
Alternative diagnosis as likely or greater than that of deep-vein thrombosis	-2
Clinical probability simplified score	
DVT likely	≥ 2
DVT unlikely	≤ 1

Venography is an invasive technique whereby venous contrast (dye) is injected into the vein on the foot's dorsum. The main reason for introducing the dye into the vein is to make that vein visible under X-ray. The DVT appears in high resolution as a filling defect. Other methods have been superseded due to the risk of contrast reaction and its invasive nature [23].

Duplex ultrasound involves a combination of B-mode imaging and pulsar Doppler to provide information on blood velocity. B-mode ultrasound imaging is the centrepiece of DVT investigation and is widely available, relatively inexpensive and non-invasive. Ultrasonography uses ultrasonic waves to produce an image of the underlying structures [12]. Areas of "no flow" due to thrombus show up as black ("hypo-echoic") against the colour flow. The technique has high sensitivity and specificity (90 and 94% respectively) for the detection of proximal symptomatic DVT [23], [29]–[32].

D-Dimer tests are increasingly being used to diagnose patients suspected of DVT. D-Dimers are fibrin degradation products that are produced during the immediate fibrinolytic response to thrombin formation. In this test, the plasma levels rise if thrombin is present. However, this test has limitations, as plasma levels are also raised during pregnancy, infections or malignancy. Due to its high sensitivity, the D-Dimer test is more effective for low-risk patients than other tests [23], [33].

Magnetic resonance imaging (MRI) is increasingly being applied to investigate DVT, mainly during pregnancy. It is a non-invasive and effective confirmatory test. It has a sensitivity and specificity for

DVT of 91.5% and 94.8%, respectively. The main challenge is that it is expensive, and availability is limited. Computed tomography (CT) is useful for diagnosing central venous occlusion and peripheral venous thrombosis. Indirect CT, with a single slice, was first proposed by Loud *et al.* [34]. CT venography has shown a sensitivity of 97% and a specificity of 100% for DVT. Both techniques may occasionally be used to detect isolated iliac vein thrombosis that may be missed on the ultrasound scans [23], [34]–[37].

Venous Occlusion Plethysmography is a non-invasive technique that is widely used to detect DVT. The venous outflow rate is compared with the maximum calf volume change, to determine the presence of major venous outflow obstruction [2]. A probe containing an infrared light-emitting diode and a sensor is placed on the calf above the knee. The infrared becomes attenuated by blood, and the pulse can be recorded. The intensity of light reflected predicts the amount of blood in that area at the time. There is little consensus about the best diagnostic strategy for DVT in published work. An untreated thrombus can be fatal, and administering anticoagulant in the absence of a thrombus is irresponsible[2], [38], [39]. Kyrle and Eichinger proposed a systematic step by step diagnostic procedure for DVT illustrated in Figure 2.2. It indicates situations where the patient needs to be treated for DVT and when DVT should be excluded, using non-invasive, rapid and cost-effective diagnosis techniques [2], [18].

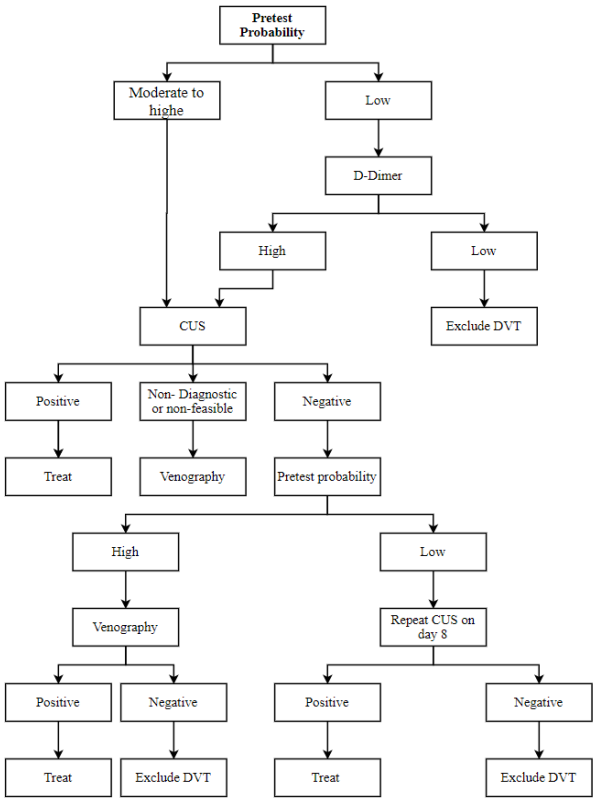

Figure 2.2: Diagnostic procedure for DVT developed by Kyrle and Eichinger.

2.1.5. Treatment

DVT therapy aims to prevent the growth of the thrombus, acute PE, thrombosis recurrence, and post-thrombotic syndromes development. The treatment of isolated calf vein DVT is variable, and there is no clear evidence to guide treatment. Some medical centres do not treat the condition, while others carry out a series of scans to detect thrombus progression. Some clinicians administer aspirin, while others make use of different anticoagulant drugs [12]. What is certain is that about 8.6% of superficial thrombophlebitis cases may extend into the femoral vein, increasing PE risk [40].

Above-knee DVT is treated with anticoagulant medication, due to the risk of potential PE [12]. Anticoagulants are widely accepted as the standard therapy before the widespread use of current diagnostic modalities. Anticoagulants inhibit the clotting cascade and shift the imbalance, allowing fibrinolysis to occur [12].

Initially, the treatment usually involves administering a therapeutic dose of unfractionated heparin (UFH), low-molecular-weight heparins (LMWH) or fondaparinux [41]. UFH and LMWH are effective pharmacological agents for the prevention and treatment of DVT. Studies have shown that the incidence of DVT or PE has been significantly reduced by the administration of a low dose of UFH. Kesieme et al. explained that the efficacy of treatment using heparin is dependent on the ability to achieve a critical therapeutic ratio within the first 24 hours of treatment. The advantages LMWH has over UFH make it preferable for treating acute DVT. However, UFH is preferred in patients with severe renal failure as LMWH is usually excreted from the kidney [41].

Warfarin is the primary drug of choice for long-term treatment once acute anticoagulation is achieved. LMWH is preferred in pregnancy and patients with cancer for long-term treatment as warfarin is contraindicated. Also, using LMWH is more effective in these cases as it prevents recurrent venous thrombosis without statistically significant bleeding risk [41].

Overlapping heparin with warfarin is essential because factors II, IX, X will not be affected until five days after the start of treatment, keeping the intrinsic clotting pathway intact. Heparin is initially given with warfarin and stopped after 4-5 days. At this time, the international normalized ratio (INR) should be within the therapeutic range (2.0 to 3.0). The treatment duration for uncomplicated first-episode lower limb DVT is three months, which may extend to 6 months depending on the presence of ongoing risk factors [12].

In the case whereby the patient is unable to be safely anticoagulated such as recent major head trauma, a device known as an inferior vena cava (IVC) filter may be deployed [12]. IVC filter is a basket-like device deployed into the IVC, using an endovascular approach, thus preventing any thrombo-emboli from flowing to the lung. This method does not prevent emboli from other parts of the body, like the upper limbs, from reaching the lung [12]. The filter's effectiveness has been studied and it was revealed

that significantly fewer patients suffer PE in the short term. The rate of recurrent DVT increased in the longer term. Complications of IVC filters include haematoma over the insertion site, filter migration, DVT at the insertion site, filter embolization, filter erosion through the IVC, and, IVC obstruction [41], [42].

Thrombotic therapy involves intravenous catheter-directed administration of a thrombolytic agent to breakdown clots in the vein. The thrombolytic agents available include tissue plasminogen activator, urokinase, and streptokinase. The risk of significant bleeding involved with this procedure should be weighed against the benefits of complete and rapid lysis of thrombi [41].

In cases where there is a bleeding risk, physical preventive methods that focus on encouraging the blood flow, instead of altering the biochemistry, are applied. Physical methods such as the use of a graduated compression stocking (GCS), intermittent pneumatic compression (IPC), and electrical muscular stimulation are used to prevent the onset of DVT and PE in patients [43], [44].

2.2. Coagulation and Deep Vein Thrombosis

2.2.1. Overview

Initially, it was thought that when blood is exposed to air, coagulation begins. In the mid-19th century, it was proposed that the ability of blood to clot was a function of a specific component of blood. The coagulation models developed in the 20th century described the stages of coagulation where fibrinogen is converted to fibrin by thrombin. Over the decades, the plasma component of coagulation was sorted into specific proenzymes that could be converted into enzymes [45]. It is vital to develop a clear understanding of the clotting process, as clot's mechanics influences clot behaviour and formation.

2.2.2. Platelets

The platelet is an irregularly shaped, non-nucleated blood fragment. It usually has a diameter of about 2 to 4 microns. There are approximately 250000 platelets per mm^3 of healthy blood, comprising less than 1% of the total blood volume. Platelet's primary function is to aid haemostasis (stopping bleeding) by forming a thrombus or clot [46]. Platelets exist in the activated and inactivated state. When a platelet activates, its shape changes from a variable disk shape to a star-like shape. It also releases chemicals such as adenosine diphosphate and thromboxane A2, contributing to clot formation [46].

2.2.3. Normal Blood Flow in the Deep Veins of the Leg

Blood consists of white blood cells (leucocytes), red blood cells (erythrocytes), and platelets (thrombocytes) suspended in plasma. The plasma is an aqueous solution of 96% water and 4% protein. Red blood cells make up more than 99% of the total cells and 40-45 % of the blood (plasma plus cells) [47]. At this haematocrit, blood has a viscosity of $4 \times 10^{-3}\ kg/ms$ and a density of 1050 kg/m^3 [48]. The diffusivities of thrombin and fibrinogen were found to be $7.0 \times 10^{-8}\ kg/ms$ and $2.1 \times 10^{-8}\ kg/ms$, respectively [49].

Normal blood flow in the veins is laminar with a higher velocity at the vein's centre than at the walls due to friction. This usually leads to a parabolic velocity profile of Hagen–Poiseuille flow. Table 2 below shows the blood flow properties measured as used in literature.

Table 2: Blood flow properties used in Literature.

Properties	**Value**	**Reference**
Mean Peak Blood Flow Velocity (cm/s)	12 ± 0.6	Abraham *et al.* 1994 [50]
	13.87	Fronek *et al*. 2001 [51]
	13 ± 5	Moneta *et al.* 1988 [52]
	9.8 ± 3.4	Coffman *et al.* 1975 [53]
Femoral Venous diameter (mm)	5.4 ± 0.9	Abraham *et al.* 1994 [50]
	11.84	Fronek *et al*. 2001 [51]
	11.2	Lattimer *et al*. 2014 [54]
	11.1±2.8 (max) 8.3±2.2 (rest)	Jeanneret *et al*. 1999 [55]
	9.0 ± 1.6	Moneta *et al.* 1988 [52]
	9.76 ± 2.21	Hayakawa *et al.* 2019 [56]
Mean Blood Pressure (mmHg)	82 ± 6	Coffman *et al.* 1975 [53]
	80 – 90	Eberhardt *et al*. 2014 [57]
CFV Blood pressure	21.4 ± 7.3	Kurstjens *et al*. 2016 [58]
CFV Reynolds number	450 – 700	Fronek *et al*. 2001 [51] Caro *et al*. 2012 [59]

Blood was originally considered to be a Newtonian fluid [60]. It was then discovered that blood changes viscosity depending on the amount of stress that is applied. This viscoelastic property makes blood a non-Newtonian fluid. However, at high shear rates (> 100 s^{-1}), red blood cells cannot aggregate, rendering the viscosity constant. It was later discovered that the viscosity of blood could be assumed to be constant in larger vessels (> 1 mm radius), but the viscosity decreases significantly when the radius drops below that value [60]–[62].

Some researchers concluded that considering blood as a non-Newtonian fluid for larger vessels such as the femoral vein is crucial [63], [64], while others believe it is an unimportant assumption [65], [66].

2.2.4. Coagulation Cascade

The cascade model consists of a sequence of steps where proenzymes generate. Most of the steps happen on phospholipid membrane surfaces, platelets, and endothelium. The split of fibrinogen by thrombin is the most notable exception to the membrane requirement [45].

2.2.4.1. Early Models of Blood Coagulation

In the 1960s, two biochemists proposed a coagulation model that comprised a series of steps detailing how each clotting factor's activation led to another's activation, which eventually led to a burst of thrombin generation. Each factor in this model is a proenzyme and could be converted into an active enzyme. The model was divided into extrinsic, intrinsic, and common pathways. The extrinsic system localizes outside the blood and consists of tissue Factor (TF) and FVIIa, while the intrinsic system is localised within the blood. By contrast, the factors in the intrinsic system were all thought to be intervascular. Both the intrinsic and extrinsic pathways could activate factor X, which eventually converts prothrombin to thrombin. In this model, the components of the extrinsic pathway are reflected in the prothrombin time (PT), while those of the intrinsic pathways are reflected in the activated partial thromboplastin times (aPTT) [45], [67]. The modern coagulation cascade consists of three phases:

- Initiation phase
- Amplification phase
- Propagation phase

2.2.4.2. Initiation Phase

A significant amount of evidence, to date, has indicated that TF initiates coagulation *in vivo*. The initiation step is localized to the cells that express TF. These cells are generally found outside the blood, thus preventing the coagulation initiation under normal flow circumstances. Circulating cells such as monocytes or tumour cells may also express TF on their membrane surface, but this TF is assumed to be inactive or encrypted. Some researchers believe that the inactivity of circulating TF is a result of the additional bond that must be broken for activity, while others argue it is due to the membrane surface not being a PS-containing pro-coagulant membrane [45], [67], [68].

Once blood flow is exposed to a TF bearing cell due to injury, the initiation phase begins. FVIIa rapidly binds to TF. This also activates more FVII, which in turn activates small amounts of FIX and FX. FXa associates with its cofactor, FVa, to form prothrombinase complexes on the TF bearing cell's surface. FV can be activated by FXa, although the process occurs slowly. Any FXa that dissociates from the TF-bearing cell is inactivated rapidly by either TFPI or ATIII. Thus, the presence of inhibitors effectively restricts the generated FXa to the TF-bearing cell surface on which it was generated. FIVa is not inhibited by TFPI and it is inhibited relatively slowly by ATIII, hence it can move from the TF-bearing cell to a nearby platelet or another cell surface [45], [67], [69].

The low-level activity of the TF pathways occurs within the extravascular space. The coagulation proteins leave the vasculature, diffuse through the tissues, and are found in the lymph. This results in the binding of FVII to extravascular TF, even when there is no injury. This ongoing process does not lead to clot formation under normal circumstances because large components of the coagulation process such as platelets and von Willebrand factors (vWF) are confined to the vascular space. Clot formation begins in the amplification phase when these components can spill out into the extravascular tissues and bind with the TF-bearing cells at the injury site [67].

2.2.4.3. Amplification Phase

Amplification allows for subsequent large-scale thrombin generation in the propagation phase. A small amount of thrombin is generated on the surface of the TF-bearing cell in the initiation phase. This thrombin has several vital functions. The primary function is to activate platelets leaked from the vasculature at the injury site. The thrombin's binding process to platelets changes the platelet's surface properties, resulting in shape change. During activation, the platelets release FV in their partially activated form to its surface [67]. Another function of thrombin is the activation of cofactors V and VIII on the activated platelet's surface. In addition to this, thrombin cleaves FXI to FXIa [45]. In the process, the FVIII (vWF) complex is dissociated, which allows vWF to mediate platelet adhesion and aggregation. The released FVIII is then activated by thrombin to FVIIIa [45], [67], [70].

2.2.4.4. Propagation Phase

The propagation phase occurs on the surface of the activated platelets. Once a few platelets have been activated, the release of granule content triggers the recruitment of more platelets at the injury site. Firstly, FIXa activated during the initiation phase binds to FVIIIa on the platelet surface. Then, additional FIXa can be supplied by the platelet bound FXIa. Since FXa cannot effectively move from the TF-bearing cell to the activated platelet, factor IXa/VIIIa complex provides FXa directly on the platelet surface. The FXa rapidly reacts with FVa bound to the platelet during the amplification phase. The completion of the prothrombinase assembly results in a burst of thrombin generation leading to cleavage of magnitude substantial amount of clot fibrinogen[45], [67].

The propagation phase of coagulation can only occur effectively on platelet cells. The platelet surface is specialized to coordinate the assembly of the tenase (FVIIIa/IXa) and prothrombinase (FVa/Xa) complexes. The role of FXIa is to enhance the amount of platelets-surface FIXa. This augments the supply of platelet surface FXa and thereby controls the amount and rate of thrombin released [45], [67].

2.2.5. Pathology of Deep Vein Thrombosis

Virchow's triad, shown in Figure 2.3, was developed by Rudolph Virchow in 1858 and clarified the clotting system of the human body. Virchow proposed that three main factors contribute to the development of a thrombus. These included blood flow stasis, endothelial injury, and

hypercoagulability. Hypercoagulability occurs when the blood tends to clot more than it is usually expected to [15].

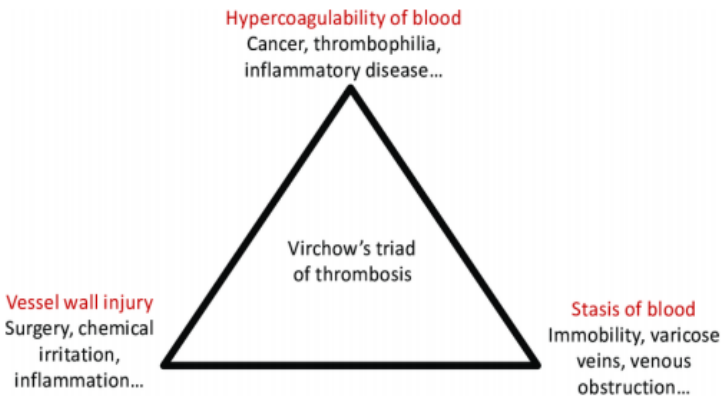

Figure 2.3: Virchow's Triad [71]

According to Virchow, there should be at least two factors in the triad present for a clot to develop. The triad has laid a path to help clinicians develop methods of reducing blood clotting [71]. Endothelial cells typically produce plasminogen activator inhibitor-1 and plasminogen activator. These factors need to be balanced with prostacyclin, nitric oxide and cell surface glycosaminoglycans to prevent DVT. Trauma to the endothelial wall exposes the membrane of the vein and upset the balance causing platelet activation. Trauma and surgery cause the tissue factor (TF) release from extravascular tissue and the adventitia [23]. Immobility leads to reduced or stagnant flow within the vein. This, coupled with other risk factors, may lead to thrombus formation in the vein valve [23].

2.3. Implementation of CFD in Deep Vein Thrombosis

2.3.1. Overview

To fully model thrombus formation in a vein, the blood flow dynamics and the blood clot formation are considered. Modelling flow dynamics mainly involves applying various mathematical techniques to solve the governing equation (GE). The modelling of blood clot formation is a more complex process. Therefore, the various protein reactions and polymerizations and their effects on different time and length scales. This makes it difficult to model this process using one method [72].

2.3.2. Haemostasis Models

Using the above-mentioned methods, the models of the processes involved in thrombosis can be integrated to simulate the development of a thrombus in time and space. These are mainly biological and biochemical models, including coagulation reactions, platelet activation, platelet adhesion and blood flow [73].

2.3.2.1. Coagulation Pathway Models

In the coagulation cascade steps; protease generation depends on the enzymes' actions on a precursor molecule (zymogen). Based on biochemical research, the components and pathways describing their interaction are mostly known, but it is also essential to develop computational models to understand the relationships between the elements quantitatively [73].

Lo *et al.* developed the first comprehensive system using ordinary differential equations (ODE) models to describe the TF pathways, assuming a uniformly-mixed and static blood environment [74]. The model compared well to experimental data. Although there was no new information derived from the model, the ability to simulate the pro coagulation pathway provided a quantitative description of the catalytic events that lead to thrombin generation. A kinetic Monte Carlo model was introduced to simulate coagulation when blood zymogens and enzymes' concentration is low. These Monte Carlo models help elucidate the coagulation dynamics with a small number of TF molecules in a small volume of blood, which is usually difficult to observe in experimental studies [73].

Hockin *et al*. also developed a model of the extrinsic blood coagulation system, which included the anticoagulants. The model includes TFPI, AT-III, FVIIA, FIXa and, FXa. The simulations are initiated by exposing TF to factors II, IX, X, VII, VIIa, V, and VIIII, and the anticoagulants TFPI and AT-III at concentrations associated with coagulation pathology. Thrombin generation proceeds through the phases discussed previously. The model results are compared with empirical data, and it is illustrated that most experimentally observable parameters are captured by the model [75].

ODE models were also introduced to integrate the blood coagulation reactions with haemodynamic factors and platelet interactions. This explores the significance of surface binding sites for coagulation reactions [73]. Another study focused on using an ODE to represent the dynamics of thrombin formation in the vascular and non-vascular systems, assuming a uniformly mixed, static fluid environment. The model also proved that lipid concentration might influence the effectiveness of the inhibitory pathways [73].

2.3.2.2. Fibrin Network Models

Due to the complexity of fibrin polymerization, few modelling studies have been conducted. To model this process, the molecular dynamics for fibrinogen assembly and protofibrils' structures must be considered. Neither molecular dynamics, kinetics, nor continuum approaches can accomplish this goal.

A kinetic model developed by Weisel *et al.* helped understand the fibrin assembly mechanisms that account for experimental observations. The model predicts that polymerization is divided into three steps; fibrinopeptide A cleavage, protofibril formation, and lateral aggregation protofibril to fibres. As predicted by the model, the effects of changing the rate of cleaved fibrinopeptides and fibre aggregation were consistent with the experimental observations [76].

Yang *et al*. proposed a model of fibrinogen assembly based on the structures of fibrin and fibrinogen fragments. Therefore, this presented proof that coagulation proteases diffuse within a polymerizing fibre by forming cross-links between αC-domains. Fibrin network models can also be designed to predict the relationship between change in fibrin monomer's supply rate and the fibrin gels' branch concentration [73], [77].

2.3.2.3. Platelet Activation Models

These models have been extensively studied, enabling identification of the components of the signal transduction pathways that respond to specific platelet activators. A model was developed using a set of ODEs to simulate adenosine diphosphate (ADP) activation. The model is divided into four sections: Ca^{2+} release and uptake, P2Y_1 G-protein signalling, phosphoinositide metabolism, and protein kinase C regulation of phospholipase Cβ. The model predicts the resting steady-state concentrations of Ca^{2+} and inositol 1,4,5-trisphosphate. It also has been refined to identify the principal components that regulate the system [73].

2.3.2.4. Platelet-Platelet Adhesion and Platelet-Vessel wall Interaction Models

Adhesion of platelets onto the vessel wall during thrombogenesis is a critical process. It involves the binding of multiple platelet receptors to one or more ligands. Mori *et al.* proposed a computational model that simulates platelet adhesion and aggregation, taking the two plasma proteins' distinct properties into account. The simulation agreed that thrombus development does not require just vWF but also fibrinogen [78].

A model showing shear-induced platelet adhesion to vWF at the injury site was developed. The platelets were modelled as rigid spheres. The model suggested that the platelets' dynamic characteristics flowing closest to the surface are different from the rest and these differences result from the difference in relative positions between platelets [73].

2.3.2.5. Integrated Thrombogenesis Models

Improvements have been made on integrating spatial and temporal subprocesses involved in thrombogenesis due to computational modelling tools' advances. A model that simulated embolus growth in a vessel wall resulting in haemorrhage showed that blood flow affects the thrombus structure and the coagulation process. A second model was used to simulate the initial phase of thrombus growth, showing that the thrombus's growth is dependent on the blood velocity and the rate of chemical reaction [73].

Pivkin *et al.* developed a 3-D model of thrombus formation in the blood vessel, considering each platelet as a sphere and the suspension of red blood cells as a continuum. The model accounts for the movement of each platelet. The model indicated the dependence of thrombus growth rate on blood velocity as obtained in experiments [79].

2.3.3. Computational Modelling Methods of Blood Clots

2.3.3.1. System-Level Methods

System-level methods model the blood flow and clot formation from a birds-eye view, applying mathematical relationships to converge towards experimental results. The mathematical relationship used is the convection-diffusion-reaction (CDR) equations with experimentally estimated constants. This method is advantageous as it is less complicated and can simulate the qualitative behaviour of blood clotting related events [72]. A simple application of the method is the simulation of fibrin clotting time using ordinary differential equations (ODEs). In this case, the blood coagulation factors are modelled as time-dependent concentrations, chemical reaction are simulated using ODEs and the clotting time of fibrin is simulated and matched with experiments [72], [80], [81].

Kinetic models can be developed at different stages using rate equations and can be combined with spatial information to improve accuracy. This method's major drawback is the dependency on different empirical models and experimental values for rate constants, which increases error [76].

2.3.3.2. Continuum Methods

Continuum methods focus on understanding the clotting process when physical geometries are considered. Therefore, this is important when studying blood clots in complex geometries and under various environmental and mechanical factors. Blood is modelled in its simplest form as an incompressible Newtonian fluid flowing between two parallel plates, giving rise to Poiseuille flow [82]. Most of the available continuum models assume that the blood vessels are rigid walls and that blood constituents are massless particles. The flow pattern is then disturbed when the thrombus is formed near the plate/wall [72], [83]–[85].

The complexity of these models is dependent on the level of detail of the blood constituents that are considered. The continuum model combines Navier Stokes (NS) equations for flow dynamics and the CDR equations. By increasing the platelets' concentration, the thrombus is modelled, fibrin, and other blood constituents [72], [86].

2.3.3.3. Discrete Particles Methods

The application of the dissipative particle dynamics (DPD) method has caught the attention of researchers due to its versatile fluid simulation capabilities at micro and nanoscales. The DPD method involves modelling platelets as beads and fibrin fibres as polymer chains connecting the beads. The pressure and velocity boundary conditions are defined as external forces to the system and can be solutions of a simple Poiseuille flow [87].

A significant challenge of the DPD method is the simulation of thrombus formation or dynamic bead adhesion to the wall. Filipovic *et al.* employed an additional force-based model F_w^a to represent the attractive force between the wall and the bead. The distribution of blood factors, obtained from the

method, are compared with the experimental results, and an effective spring constant is derived. This method can be improved by incorporating CDR equations for thrombin concentrations, fibrin concentrations, and basic coagulation pathway models [72], [87]–[90].

2.3.3.4. Multiscale Methods

The multiscale methods involve coupling two or more computational methods together at different lengths or time scales [72]. A multiscale model was developed using CDR equations and a discrete Cellular Potts model (CPM) to simulate platelet activation, migration, and binding behaviour. The fibrin concentration is represented by a rate equation related to the concentration of activated platelets. Improvements are made to the model by adding a set of CDR equations representing surface-mediated clot formation and ODEs to represent fibrin polymerization [72], [91].

Instead of applying CPM and CDR equations, the variational multiscale method and smooth dissipative particle dynamics (SDPD) were used to simulate multiscale blood flow. For this model, other criteria, such as the role of blood factors, need to be taken into account [72], [73].

Xu *et al.* developed a multiscale model of thrombus growth. The model breaks down the coagulation process into sub-models. The Navier-Stokes equations account for the macroscale dynamics of blood flow. The microscale interactions between platelets, fibrinogen, and the vessel wall are described by the cellular Potts model. The Mann model accounted for the biochemical processes which are described using partial differential equations. The model was used to show the dependency of the clot's size formed on the blood flow rate. Preliminary experimental data validated the results of the simulation. The different types of cells that participate in the model's thrombus growth are shown in Figure 2.4 [91].

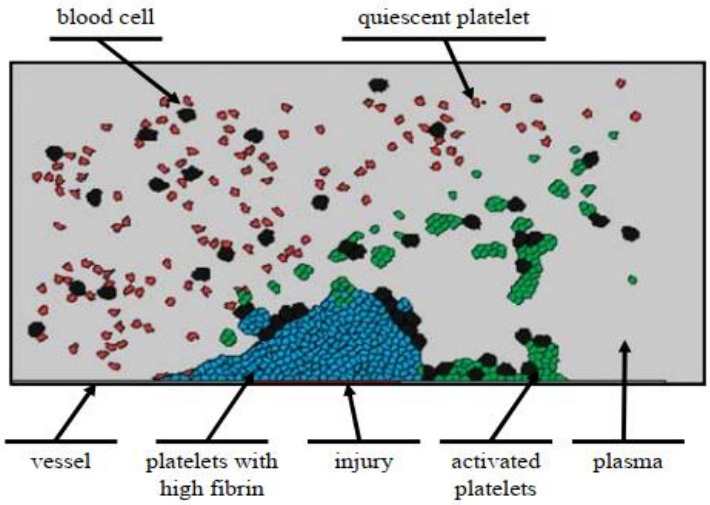

Figure 2.4: Multiscale model developed by Xu et al. The cells interact on a microscale level and the blood flow as a continuum [91].

Shadden and Hendabadi developed a predictive model for potential regions for platelet activation in a stenosed vessel. Blood was modelled as platelets ($\approx 2\mu m$) suspended in plasma. The prediction of the activation potential (AP) $\alpha(x_0, t_0; t)$ for a platelet at position $x_0 = x(t_0)$ was done by solving the Lagrangian integral of the strain rate.

$$\alpha(x_0, t_0; t) = \int_{t_0}^{t} \|e(x(s), s)\|_F \, ds$$

Where $x(s)$ is evaluated along the platelet's trajectory and e is the strain/deformation tensor.

This model integrates the principal stresses along the platelet trajectory with the platelets modelled as finite elements [92]. The assumption that platelet activation occurs solely through fluid mechanics was made. The model showed that maximum platelet activation occurs close to the stenosis peak, which indicates that thrombus growth will propagate there (see Figure 2.5)[93].

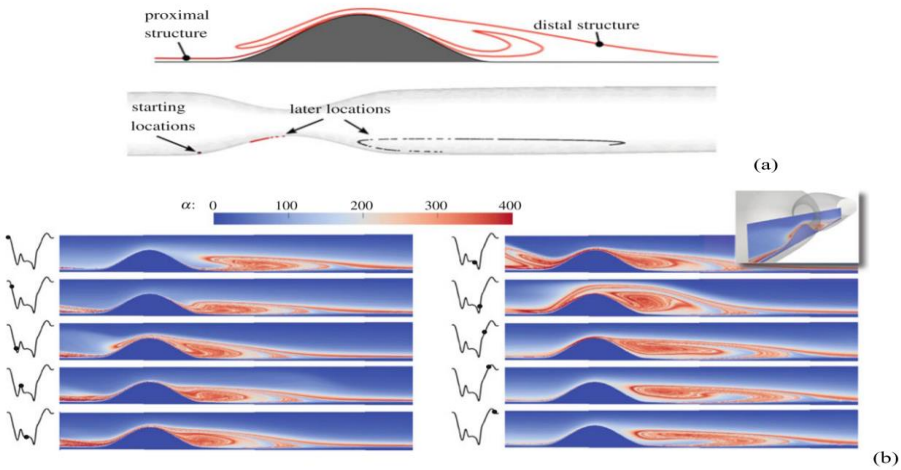

Figure 2.5: Predictive model of Activation Potential of platelets in a stenosed vessel developed by Shadden and Hendabadi. (a) The starting and later location after one cardiac cycle. (b) The instantaneous AP contours at different points of the cardiac cycle [93].

The interaction between blood flow, biochemical reactions, and the effect of thrombus growth was studied by Bodnar and Sequeira [94]. They developed a simplified variation of the model presented by Anand *et al*. The model studied clot formation and lysis integrating biochemical, physiological, and rheological factors. Blood flow was described by the Navier Stokes equations, ignoring the viscoelasticity of blood. A network of twenty-three advection-diffusion-reaction equations described the changes in biochemical concentrations and transport of enzymes. The model was simulated in three-dimensional cylindrical geometry. The clot growth was studied by tracking the fibrin concentration in all cells, and when the value exceeds the set threshold, the cell was said to have clotted. The viscosity is capped at a value that is 100 times higher than that of blood. The time integration was solved using an explicit Runge-Kutta scheme. The simulation begins with no clotted cells, and as the fibrin concentration increased, is clotting initiated and propagated [94].

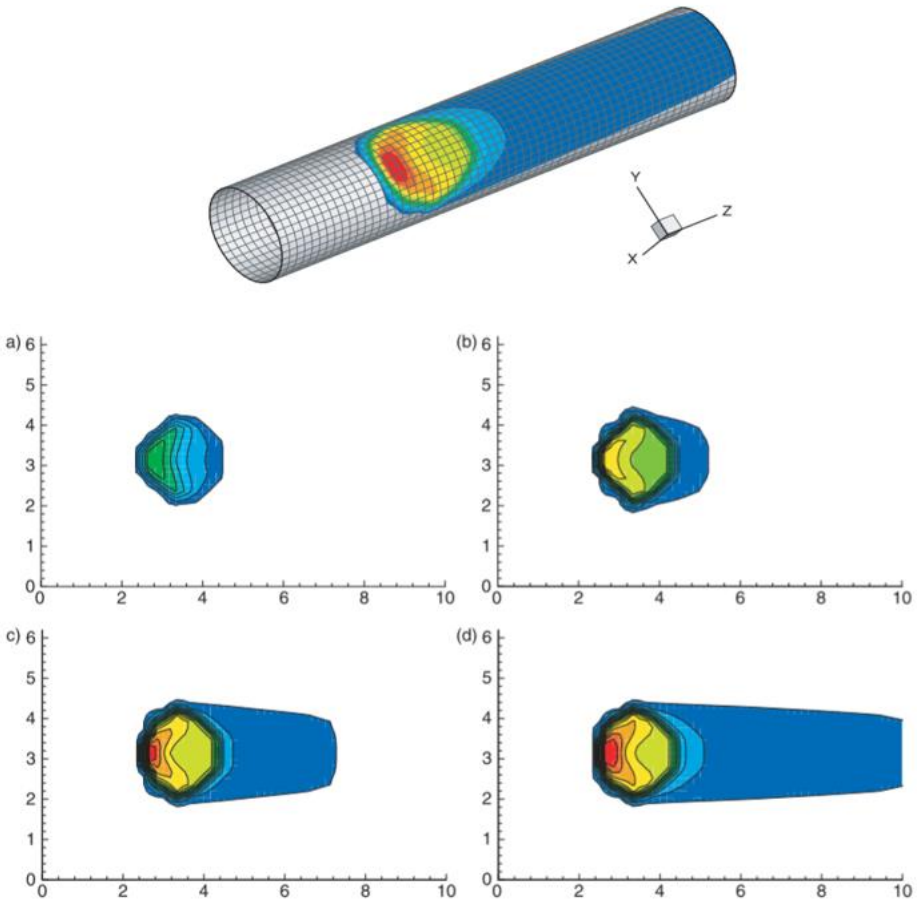

Figure 2.6: Three dimensional Model developed by Bodnar and Sequeira showing the evolution of fibrin concentration on the vessel surface at (a) the 30s, (b) 40s, (c) 50s, (d) 60s. [94]

2.3.4. Deep Vein Thrombosis CFD Models

The previous sections describe the models of coagulation. In this section, some models that focus on CFD models of deep vein thrombosis are described.

Ramunigari *et al*. proposed a model that predicts unidirectional blood flow in a vessel in the presence of venous thrombosis. The mechanism of thrombus formation or the biochemistry involved was not examined. The model purely accounts for blood flow dynamics by solving the Navier Stokes equations, as the density of the blood clots was manipulated. The model showed a strong inverse correlation between clot density and flow velocity [95].

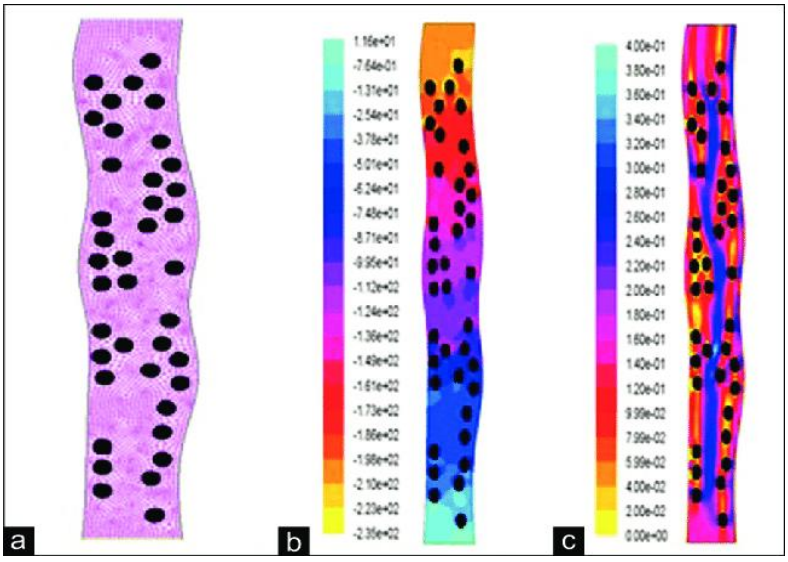

Figure 2.7: Model of venous thrombosis presented by Ramunigari et al., (a) Geometry and mesh (b) Pressure contour (c) Velocity contour. The model accounts for clots as spherical elements forming lumps on the vein wall [95].

At higher fluid shear rates, platelet adhesion is facilitated by the vWF [96]. This led to the development and validation of a predictive model of thrombus growth under the high shear rate by Mehrabadi *et al*. The model allowed flow under constant pressure or volumetric flow rate in a cylindrical channel. Thrombus growth was given as a function of time, wall shear rate, and channel radius.

A model by Ibrahim *et al*. was used to analyse the effect of valve opening in the popliteal vein on pressure, velocity, and vorticity of blood flow. Therefore, this model assumed that blood is a non-Newtonian fluid under isothermal conditions. Two cases were examined. The first case A modelled the first and second valve openings at 50% and 70% (Case A), respectively. The other case B modelled valves opened at 50% and 30% (Case B), respectively. It was found that case B produced larger vorticity than A at the second valve, which indicates a higher possibility of clotting around the valve [97].

Simao *et al*. developed a model that showed the effects of DVT on the venous valves and the implication of valve failure on the blood flow circulation in the vessel. The model applied a finite element method (FEM) with particular boundary and element characterizations to solve the fluid-solid interactions' governing equations (FSI). Blood is considered a non-Newtonian fluid under laminar flow, and the wall

is considered a flexible material. Three venous valves were simulated, comparing the blood flow in a normal and an abnormal valve operation. The model was validated using *in vivo* echo-Doppler measurements, shown in Figure 2.8. The model showed that a clot forms during abnormal functioning of a venous valve, impairing blood flow in the vein and resulting in numbness or even paralysis [98].

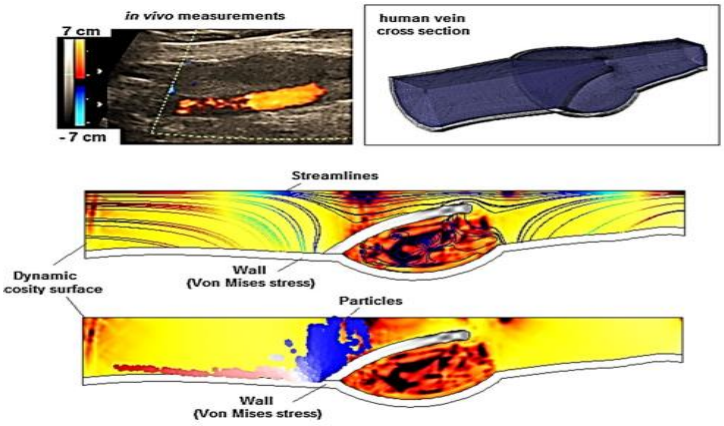

Figure 2.8: Simao et al showing the clot formed in an abnormal venous valve operation, comparing the simulations to the in vivo measurements [98].

Xu *et al*. presented a multi-phase model, illustrated in Figure 2.9, that was used to study the impact of shear flow conditions on the deformation and embolization of a growing clot. The Navier-Stokes equations and the Cahn-Hilliard equations were used to describe blood flow and deformation of the clot. It was assumed that the blood clot has two components, namely the core and shell. The volume fraction of platelets to plasma was 0.7:0.3 in the core and 0.3:0.7 in the shell. The model showed that the clot's changes in shape and size due to flow are mostly dependent on the attachment of platelets to the exterior of the clot and the removal of large clot pieces due to shear. It also showed that the higher the blood clot's permeability, the more prone it is to embolization [99].

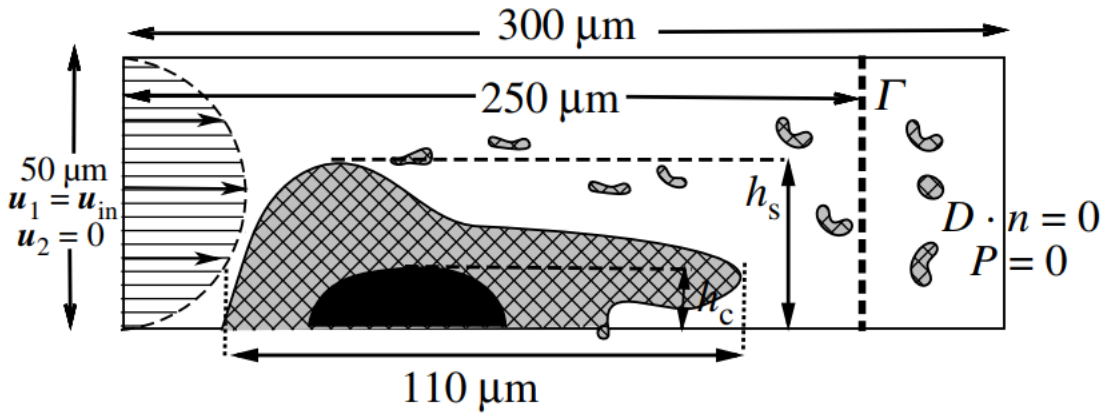

Figure 2.9: Schematic diagram of the model developed by Xu et al, Constant inlet flow of blood. u_1 and u_2 are the longitudinal and average velocities along and perpendicular to the vessel wall. The black filled indicated the core and the meshed region represented the shell [99].

A patient-specific DVT model was developed by Fortuny *et al*. The model simulates the flow of blood in a realistic popliteal vein geometry generated from *in vivo* CT images from a patient with a thrombus above the knee. The conservation equations were solved to simulate the incompressible flow of blood. The model was used to study anticoagulants' effects on blood dynamics around a thrombotic area in a vein by varying the blood viscosity. The effect of blood flow on the wall shear stress level was studied using both Newtonian and non-Newtonian viscosity models. The velocity and wall shear stress contour derived from the model is illustrated in Figure 2.10 [100].

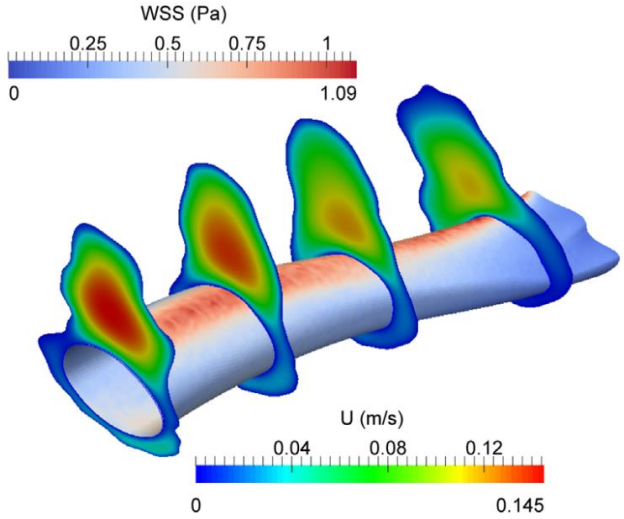

Figure 2.10: DVT model proposed by Fortuny et al, illustrating the WSS along the surface of a thrombus and the velocity magnitude at four cross-section planes. The leftmost cross-section plane corresponds to the outlet [100].

2.3.5. Computational Modelling of Venous Valves

Venous valves are one-way valves that allow flow towards the heart and restrict backflow. Malfunction of the valves can cause significant problems in blood circulation. With the introduction of CFD modelling into medical imaging, the operation and effects of different venous valves' configurations can be studied. Numerical methods were developed by Noda *et al*. and Ohashi *et al*. to study the flow behaviour around the valve's leaflets [101], [102]. A pair of vortices developed and the sinus' function around the valve was also seen to contribute to flow regulation. The result was validated with a flow experiment. The increase in velocity, pressure drop and deformation of the valve orifice during a heartbeat cycle was studied by Narracott *et al.*, and the method was then used by Buescher et al. to study the effects of varying the leaflet gap and the ratio of the sinus depth to the vein diameter experimentally[13], [103].

An experimental procedure was carried out by Lurie et al, to understand the mechanism of venous valves on the blood flow velocity. Volunteers with no history of venous disease underwent duplex ultrasound scans in the standing position. The probe was moved around until the valve was identified. The time relationship between the flow and venous valve movement was investigated frame by frame. Figure 2.11 shows how valve activity affects the velocity of the blood exiting the valves [104].

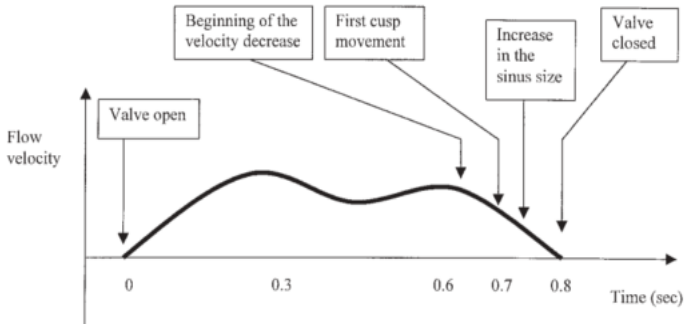

Figure 2.11: Time relationship between venous flow and valve cycle proposed by Lurie et al. [104].

A more recent model of the valve activities was developed by Hajati et al. [105]. The model applied knowledge from previous studies and was used to investigate the blood flow through the venous valve, considering the vein wall's flexibility and valve leaflets. Fluid-structure interaction was applied by solving the governing equations using the Galerkin finite element method. The model predicted the blood velocity increases from the inlet to the leaflets and the decreases passing behind the valve. The peak velocity profile confirms the profile measured by Lurie et al. [105], as shown in Figure 2.12. Also, a pair of vortices similar to those noticed by Ohashi et al. was noticed behind the valve leaflets[102].

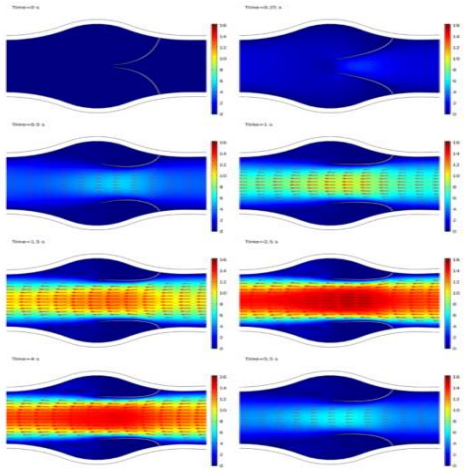

Figure 2.12: Leaflet opening and closing through one heartbeat cycle.

2.4. Experimental Models for Thrombosis

2.4.1. Overview

Venous thrombosis models have been classified into one of two categories: either a no-flow state or a low-flow state. This impacts slow thrombus development. An acute injury model is used to induce rapid clot formation. The study of DVT and other related factors has moved through various stages. Several experimental models have been developed to show and study the processes involved in blood clot formation in veins. The models are either in vivo or in vitro. Most of the in vivo models are performed on animals. The sections below discuss these models.

2.4.2. Animal Models

Animal models have played an essential role in the identification of pathways and factors that drive DVT. They have also helped with the development and optimization of antithrombotic drugs [106]. Several models have been developed using species larger than mice, such as rodents and non-human primates. One of the pioneer models was developed by Wessler and Connelly in 1952. A vein stasis model is developed by clamping vein segments in dogs for more than 20 minutes to induce clot formation [107]. This model's variables have been developed since then on other animals, including rabbits, rats, and mice. In the process, it was discovered that thrombosis could be initiated by placing a synthetic material such as a suture inside the blood vessel [106]. Another standard model is developed by creating an arteriovenous shunt that collects thrombus using a synthetic material. The "pros" of this model are that it can be performed on a wide range of animals and that it can be used for the treatment of acute or more chronic cases of DVT. A significant "con" of the model is its limitation when testing the efficacy of clinical antithrombotic drugs [106].

The IVC is the most accessible large vein in most animals; thus, most models have been created in the IVC [106]. Smaller veins such as the saphenous or femoral veins are mostly used for microscopic studies of thrombotic phenomena. IVC thrombotic models involve placing a ligature around the IVC, either tying it ultimately to stasis or tying it to allow 80-90% flow reduction. The clot is formed upstream of the ligation site, peaking at about 48 hours. The IVC models lack direct analogy to clinical DVT in a few crucial ways. One of the key differences is that the stasis site is downstream of the source, whereas it is upstream in clinical DVT. The model is performed experimentally on young, healthy animals. The IVC does not contain a valve and cannot be used to imitate events in other veins [106].

Runyon et al. developed an experimental DVT model that leads to pulmonary embolism (PE) in rats. Blood was drawn from the vein of the rat, treated with thrombin $Ca^{++,}$ and then reinjected. Clot formation increased, and PE occurred within five days [108].

2.4.3. In vitro Models

These models involve the use of methods that simulate various stages of the thrombotic process. A thrombin assay is a method used to evaluate the amount of thrombin in a volume of blood. Thrombin induced clotting time is determined by recording the increase in thrombin (usually added) and monitoring the rate of clot formation [109].

Narracott *et al.* developed an in-vitro model of blood clotting using hypercoagulable milk to represent blood. Clot formation was studied for different periods within an idealized cerebral aneurysm geometry with an idealized coil geometry within the aneurysm. Clot formation was studied using photography and mass calculation. The model results are consistent with general observations of thrombosis within cerebral aneurysms [110].

Ovanesov *et al.* developed an experiment used to investigate the effects of wall-bound cells on clot growth. In-vitro clot initiation was achieved in contact pathway-inhibited, non-flowing human plasma by human TF-expressing cells. Clotting was monitored by a real-time video microscopic system. The experiment proved that the role of TF-bearing cells is limited to the initiation stage of the clot. Clot propagation was regulated by the intrinsic Xase complex in the plasma. Although the model does not account for platelets, it is proposed that the results can be compared to *in-vivo* situations [111].

Onasoga-Jarvis *et al*. investigated the haemodynamic conditions under which fibrin formation from TF substrate under flow using a clot growth experiment. Silica beads were coated with TF and patterned into dimensioned spots. Human plasma was perfused over the beads with varying TF concentrations at shear rates between 50–1000 s^{-1}. The experiment was carried out in a hydrodynamic focusing microfluidic device. Thrombin generation and fibrin formation were studied using a fluorescent microscope. The experiment showed that fibrin formation on a surface requires a physical disturbance in the flow field. Also, a threshold spot size is necessary for fibrin formation to begin and the rate of fibrin formation decreases with an increase in shear rate [112].

Another in-vitro model was developed by Prasad et al. to study the lysis activity of thrombolytic drugs on the clot. The model involved using whole blood from a healthy human to grow a clot in a pre-weighed sterile microcentrifuge tube. The clot is then extracted and weighed before and after applying streptokinase fluid that causes lysis on the clot surface. The percentage of the clot lysis was calculated by comparing the weight difference. The experiment showed that there was a significant percentage of clot lysis when streptokinase was used. These methods could be used to rapidly observe the effects of newly developed antithrombotic drugs on the clot and can also be applied on a patient-specific level [113].

Neeves et al. developed a clot growth experiment to prove that the nature of fibrin mesh formed during thrombosis under flow is dependent on the local thrombin concentration. They introduced thrombin flux at concentrations 10^{-13}-10^{-11} nmol/μm^2-s into a flow of fibrinogen at wall shear rate 10–100 s^{-1} through a microfluidic membrane. They showed that clot formation under static condition will stop when all the soluble fibrinogen is converted to insoluble fibrin. Adding more fibrinogen made the clot denser and thicker with bundled fibres along the direction of flow. At low thrombin flux (10^{-13} nmol/μm^2 s), fibrin formation was not noticed. At the medium thrombin flux (10^{-12} nmol/μm^2 s), shear-rate-dependent fibrin morphology is formed. At the highest thrombin flux (10^{-11} nmol/μm^2 s), an occlusive fibrin gel was observed with the fibre diameters increasing as wall shear rate increased [114].

3. METHODOLOGY

To model the process of clot growth in the femoral vein, a combination of methods is used. The blood flow through the vein is accounted for by computational fluid dynamics methods. The biochemicals are transported in the blood, and the reactions are solved using a stiff equation solver. This chapter aims to explore all these methods and gives an overview of the theory behind these methods.

3.1. CFD Methods

Computational fluid dynamics (CFD) is widely used in many fields of engineering research and applications. Advances in computing technology have made it possible to model and study complex physiological flows using CFD. The application of CFD to cardiovascular medicine is relatively recent and has shown great potential, proving to be more cost-effective than traditional experimental methods.

For clinical applications, the CFD modelling process is divided into seven key stages. It begins with clinical imaging, where a range of medical imaging tools including, CT, MRI, and X-ray angiography is used. The imaging provides all the physiological details, such as patient-derived geometries and boundary conditions. Blood tests can also be done in this stage to derive the biochemical details required in the model. The details must be in the appropriate format to make data extraction possible. The next stage is segmentation and reconstruction. Segmentation converts the medical images into more simplified in-silico geometries that define the model region of interest. The geometry is then discretised or meshed, which involves dividing the geometry into several discrete volumetric cells or elements and time steps. There are many methods of discretising a volume or a geometry. However, the mesh must be refined enough to capture all the critical features and solve the equations bounding the flow. The refinement of the mesh must also not be excessive, as this will increase the computational expense on the solution time. A poor mesh will produce inaccurate results, and this should be avoided.

After the meshing is completed, the boundary conditions are defined. To have a CFD analysis, the physiological conditions at the inlet, outlet, and wall boundaries must be specified. The boundary conditions may change with time and can be patient-specific data, population data, physical models, or assumptions. Once this is done, the simulation stage begins. Depending on the code applied for the simulation, the user may be required to define some variables. The fluids' properties, the initial conditions, time discretization information, and the desired output are defined at this stage. The CFD solver uses this information to solve the Navier-Stokes and continuity equations over the defined time and the specified number of iterations. Different solver methods can be used to obtain the solution. The solution is considered to have converged when the difference between the values from two consecutive iterations is considered sufficiently small.

The CFD solver produces the velocity and pressure values at each element over each time-step. The post-processing stage involves extracting the required data and displaying it. The results from the model

are then validated against experimental results. After stating the importance and development of CFD modelling, the importance of experimental validation is noteworthy. Validation gives confidence in the accuracy and precision of the CFD model. The theory discussed in this section is derived predominantly from the ANSYS Fluent theory guide [115], and notes by Malan et al. Other works will be cited where necessary.

3.1.1. Governing Equations of Fluid Flow

The Navier-Stokes transport equations describe the blood flow dynamics. The fundamental principles governing these equations are the conservation of mass and momentum.

3.1.1.1. Conservation of Mass (Continuity)

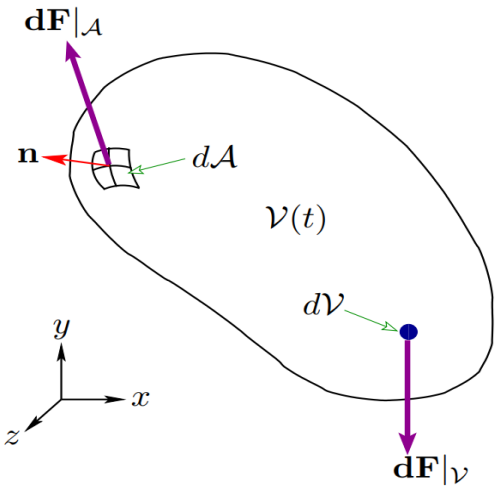

*Figure 3.1: Illustration of an arbitrary volume V(t) enclosed within a surface A(t). Normal vector **n** is pointing outwards. Volume subjected to forces F_A and F_v.*

Regarding Figure 3.1, the rate of mass increase in an element is equal to the net rate of mass flow entering the element. The conservation of the mass equation is described in Eq. 3.1.

$$\frac{\partial \rho}{\partial t} + \nabla(\rho \boldsymbol{u}) = 0 \qquad \textbf{Eq. 3.1}$$

Where ρ is the density, t is the time, and $\boldsymbol{u}$ is the velocity vector. For an incompressible fluid, the density is constant, and Eq. 3.2 can be written as:

$$\nabla \cdot \boldsymbol{u} = 0 \qquad \textbf{Eq. 3.2}$$

The continuity equation states that the conservation of mass requires the divergence of the velocity to be zero.

3.1.1.2. Conservation of Momentum

The Conservation of momentum equation is derived from Newton's second law of motion (Eq. 3.3).

$$\Sigma \boldsymbol{F} = m\frac{D\boldsymbol{u}}{Dt} = m\boldsymbol{a} \qquad \textbf{Eq. 3.3}$$

Where $\Sigma \boldsymbol{F}$ is the sum of force acting on an object, m is the object's mass, $\boldsymbol{u}$ is the velocity of the object, and $\boldsymbol{a}$ is the acceleration.

The second law of motion states that the rate of change of momentum of a fluid element is equal to the sum of forces acting on that element. Eq. 3.4, Eq. 3.5 and Eq. 3.6 describes the Navier- Stokes momentum conservation equation in the x, y, and z-direction, respectively.

$$\frac{\partial(\rho u_x)}{\partial t} + \nabla \cdot (\rho u_x \boldsymbol{u}) + \frac{\partial p}{\partial x} - \nabla \tau_x = \rho g_x \qquad \textbf{Eq. 3.4}$$

$$\frac{\partial(\rho u_y)}{\partial t} + \nabla \cdot (\rho u_y \boldsymbol{u}) + \frac{\partial p}{\partial y} - \nabla \tau_y = \rho g_y \qquad \textbf{Eq. 3.5}$$

$$\frac{\partial(\rho u_z)}{\partial t} + \nabla \cdot (\rho u_z \boldsymbol{u}) + \frac{\partial p}{\partial z} - \nabla \tau_z = \rho g_z \qquad \textbf{Eq. 3.6}$$

Where u_x, u_y, u_z are the velocities in the x, y, and z directions, respectively, g_x, g_y, g_z are the gravitational accelerations, τ_x, τ_y, τ_z are the stress tensors in the x, y, and z-direction, and p is the pressure. The equation then simplifies to:

$$\frac{\partial(\rho \boldsymbol{u})}{\partial t} = -\nabla \cdot (\rho \boldsymbol{u} \otimes \boldsymbol{u}) - \nabla p + \mu \nabla^2 \boldsymbol{u} + \rho \boldsymbol{g} \qquad \textbf{Eq. 3.7}$$

Where μ is the dynamic viscosity.

$\frac{\partial(\rho \boldsymbol{u})}{\partial t}$ is the rate of change of momentum per unit volume and is zero in a steady-state case.

$-\nabla \cdot (\rho \boldsymbol{u} \otimes \boldsymbol{u})$ is referred to as the convective term, which describes the momentum transported through the volume due to the fluid flow velocity.

$-\nabla p$ is the pressure gradient.

$\mu \nabla^2 \boldsymbol{u}$ is referred to as the diffusive term, which describes the momentum transported through the volume due to the flow of the surrounding elements' viscous effect.

$\rho \boldsymbol{g}$ is the momentum contribution on the fluid from the body force acting on the fluid.

It is important to note that the Navier-Stokes equations do not have a closed-form solution; hence the equations need to be discretized over the defined region.

3.1.2. Reference Frames

A fluid under shear will begin and continue to deform. Different reference frames are used when deriving the governing equations that define this deformation. The primary reference for the Navier-Stokes equations is the Lagrangian and Eulerian frames.

Lagrangian Reference Frame

In the Lagrangian approach, the fluid particle or control volume is moving through the flow in question. The fluid-particle carries its properties such as velocity, pressure, and density, which change with time

and are mathematically represented as $\vec{v}_p(t), p_p(t)$, and $\rho_p(t)$, respectively. A fluid property can be expressed as:

$$\phi = \phi(\boldsymbol{X_0}, t) \qquad \textbf{Eq. 3.8}$$

Where ϕ is the position vector of the control volume at some time t, and $\boldsymbol{X_0}$ is the position vector of the control volume at some reference time t. In other words, $\boldsymbol{X_0} = (X, Y, Z)$. Hence, the Lagrangian velocity for a fluid particle can then be defined as:

$$V = \left.\frac{d\boldsymbol{X_0}}{dt}\right|_{Single\ Particle} \qquad \textbf{Eq. 3.9}$$

Eulerian Reference Frame

In the Eulerian approach, the control volume is considered at a fixed point in space, and the properties of the fluid elements are recorded as they pass through that point. The properties depend on both the position and time and are mathematically represented as $\vec{v}_p(\boldsymbol{x}, t), p_p(\boldsymbol{x}, t)$, and $\rho_p(\boldsymbol{x}, t)$. Where $\boldsymbol{x}$**=** **(**x, y, z) is the spatial coordinate at any time t.

While the Lagrangian approach has multiple benefits, it is computationally expensive and can make it challenging to keep track of all the fluid particles' trajectory. For this reason, the Eulerian reference frames are mainly used in fluid mechanics.

3.1.3. General Transport Equation

The general transport equation has some similarities to the Navier Stokes equations. The equation generally describes the evolution of a quantity ϕ and can be applied to scalars quantities. The equation is described in Eq. 3.10.

$$\frac{\partial(\rho\phi)}{\partial t} + \vec{u} \cdot \nabla(\rho\phi) = \nabla \cdot (\Gamma_\phi \nabla\phi) + S_\phi \qquad \textbf{Eq. 3.10}$$

Where,

- $\frac{\partial\phi}{\partial t}$: Rate of increase of ϕ
- $\vec{u} \cdot \nabla(\rho\phi)$: Net rate of flow out due to convection of ϕ
- $\nabla \cdot (\Gamma_\phi \nabla_\phi)$: Rate of the increase due to the diffusion of ϕ.
- Γ_ϕ is the diffusion coefficient of ϕ.
- S_ϕ: Rate of the increase due to source of ϕ

3.1.4. Finite Volume Method

The finite volume method (FVM) is a discretization method used to approximate a single or partial differential equations system, describing the conservation of one or more quantities. Other techniques include the finite element method and the finite difference method. In FVM, the geometry is subdivided into a mesh, illustrated in Figure 3.2. Non-overlapping domains are then constructed from the mesh. The domain can either be cell-centred or vertex-centred, and the elements of the mesh are called control

volumes. The conservation equations are integrated over each control volume, resulting in a balanced equation. The set of balanced equations are then discretized concerning a set of discrete unknowns.

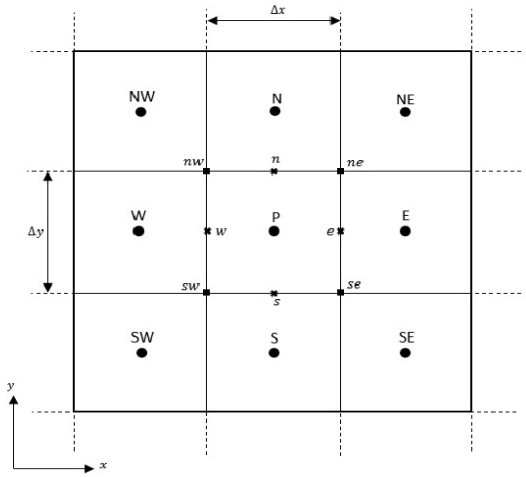

Figure 3.2: A uniform 2-D grid, showing the mesh breakdown. P is the cell centre. N, S, W, E represents north, south, west, and east, respectively, indicating the neighbouring cell centres. Furthermore, n, s, w, e are the cell faces [116].

As explained, the first step of the FVM is to integrate the general transport equation over each control volume. This is shown in Eq. 3.11.

$$\int_{cv} \frac{\partial(\rho\phi)}{\partial t} dV + \int_{cv} \vec{u} \cdot \nabla(\rho\phi) dV = \int_{cv} \nabla \cdot (\Gamma_{\emptyset} \nabla\phi) dV + \int_{cv} S_{\emptyset} dV \qquad \textbf{Eq. 3.11}$$

Applying Gauss's theorem to Eq. 3.11 yields Eq. 3.12.

$$\int_{cv} \frac{\partial(\rho\phi)}{\partial t} dV + \oint_{A} \boldsymbol{n}.(\rho\phi\vec{u}) d\boldsymbol{A} = \oint_{A} (\Gamma_{\emptyset} \nabla\phi)\, d\boldsymbol{A} + \int_{cv} S_{\emptyset} dV \qquad \textbf{Eq. 3.12}$$

Where A is the area of the face of the control volume, and n is the vector normal to that face. Discretization of Eq. 3.13 can therefore be rewritten as

$$\frac{\partial(\rho\phi)}{\partial t} V + \sum_{f}^{N\,faces} (\rho\phi\vec{u}) \cdot \boldsymbol{A} = \sum_{f}^{N\,faces} (\Gamma_{\emptyset} \nabla\phi) \cdot \boldsymbol{A} + S_{\emptyset} V \qquad \textbf{Eq. 3.13}$$

To solve the system of equations, pressure velocity coupling needs to be. The discretized transport equation is generally presented in a non-linear form concerning scalar variables ϕ. The linearized form can then be written as stated above.

$$a_p \phi = \sum_{nb} a_{nb} \phi_{n_b} + b \qquad \textbf{Eq. 3.14}$$

Where subscript nb refers to the neighbouring cell, and a_p and a_{nb} are the linearization coefficient for ϕ and ϕ_{nb}, respectively. A similar equation can be written for each cell in the mesh. ANSYS Fluent solves these linear equations using a point implicit linear equation solver (Gauss-Seidel) in conjunction with an algebraic multigrid (AMG) method.

3.1.5. Discretization

3.1.5.1. Spatial Discretization

ANSYS Fluent does discretization of scalar ϕ at the cell centres. The values at the face f, ϕ_f are needed to solve for the convection and diffusive term. ϕ_f was interpolated from the values at the cell centres. This is achieved using the upwind scheme, which involves deriving ϕ_f from quantities in cells upwind, relative to the direction of the average velocity v_n. Fluent has various schemes that can be used for spatial discretization, including first-order and second-order upwind, power law, and QUICK.

Since a high level of accuracy is desired, the second-order upwind was applied in this work. In this approach, the cell face values are derived by a Taylor series expansion of the cell centre values using equation Eq. 3.15.

$$\phi_f = \phi + \nabla\phi \cdot \vec{r} \qquad \textbf{Eq. 3.15}$$

Where ϕ is the cell centre value, $\nabla\phi$ is the cell centre value's gradient in the upstream cell, $\vec{r}$ is the displacement vector from the upstream cell centroid to the face centroid. The diffusion term is central differenced and is always second-order accurate.

3.1.5.2. Temporal Discretization

For transient simulations, the governing equations must be discretised in both time and space. The same spatial discretization is done for both steady and transient simulations. Temporal discretization involves integrating every term in the differential equation over the chosen time step Δt. Eq. 3.16 describes the time evolution of a given variable ϕ.

$$\frac{\partial\phi}{\partial t} = F(\phi) \qquad \textbf{Eq. 3.16}$$

Where F incorporates the spatial discretization, the time derivative is discretized using backward differences to give the first and second-order accurate temporal discretization described in Eq. 3.17 and Eq. 3.18.

$$\frac{\phi^{n+1} - \phi^n}{\Delta t} = F(\phi) \qquad \textbf{Eq. 3.17}$$

$$\frac{3\phi^{n+1} - 4\phi^n + \phi^{n-1}}{2\Delta t} = F(\phi) \qquad \textbf{Eq. 3.18}$$

Where $n+1$ is the value at the next time step, n is the current time step, and $n-1$ is the previous time step. The method used to evaluate $F(\phi)$ is the implicit time integration, which is done at $n+1$ (see Eq. 3.19) and can be iterated at each time step before moving to the next. The method is unconditionally stable with respect to time step size.

$$[J](\nabla\phi)_{c0} = \Delta\phi\frac{\phi^{n+1} - \phi^n}{\Delta t} = F(\phi^{n+1}) \qquad \textbf{Eq. 3.19}$$

3.1.5.3. Evaluation of Gradients and Derivations

Gradients are essential when determining a scalar's values at the cell faces (see Eq. 3.15). They are also used to compute the secondary diffusion terms and velocity derivatives. The gradient $\nabla\phi$ of a scalar ϕ is used to discretize the conservation equations' convection and diffusion terms. According to the following methods, fluent computes the gradients: Green-Gauss Cell-Based, least-squares cell-based, and Green-Gauss Node-based.

The Least-squares Cell-based method is applied in this work. In this method, the solution is assumed to change linearly. Considering two neighbouring cells c0 and ci, the change in cell values between the two cells is described as,

$$(\nabla\phi)_{c0}: \Delta r_i = (\phi_{ci} - \phi_{c0}) \qquad \textbf{Eq. 3.20}$$

Where Δr_i is the vector from the centroid of c0 to ci. Eq. 3.20 can be written for each neighbouring cell to c0 in compact form:

$$[J](\nabla\phi)_{c0} = \Delta\phi \qquad \textbf{Eq. 3.21}$$

Where $[J]$ is the coefficient matrix and is a function of the geometry. The minimization problem for the system of the non-square coefficient matrix is solved to determine the cell gradient. The coefficient matrix is decomposed using the Gram-Schmidt process, yielding a matrix of weights for each cell. Thus, for each face of c0, there are three components of weights (${W^x}_{i0}$, ${W^y}_{i0}$, ${W^z}_{i0}$) produced. Therefore, the gradient at the cell centre can be derived by multiplying the difference vector $\Delta\phi = (\phi_{ci} - \phi_{c0})$ by weight factors.

$$(\phi_x)_{c0} = \sum_{i=1}^{n} {W^x}_{i0} \cdot (\phi_{ci} - \phi_{c0}) \qquad \textbf{Eq. 3.22}$$

$$\left(\phi_y\right)_{c0} = \sum_{i=1}^{n} {W^y}_{i0} \cdot (\phi_{ci} - \phi_{c0}) \qquad \textbf{Eq. 3.23}$$

$$(\phi_z)_{c0} = \sum_{i=1}^{n} {W^z}_{i0} \cdot (\phi_{ci} - \phi_{c0}) \qquad \textbf{Eq. 3.24}$$

3.1.5.4. Gradient Limiters

Gradient limiters are applied when the second-order upwind scheme is used and prevents spurious oscillations in the flow field near areas with shock, discontinuities, or rapid local changes. The limiter attempts to prevent the linear field variable on the cell faces from going past the neighbouring cells' minimum and maximum values. The simulations in this work used the standard limiter. This limiter applies the minimum modulus function to limit the reconstructed solution's overshoots and undershoots on the cell faces.

3.1.6. Pressure-Based Solver

The simulations in this work are pressure-based. This section describes the unique methods used to approach the discretization of the momentum and continuity equations and their solutions using pressure-based solvers. The particular methods are described by taking the steady-state continuity (Eq. 3.25) and momentum (Eq. 3.26) equations in integral forms.

$$\oint \rho \vec{v} \cdot d\vec{A} = 0 \qquad \textbf{Eq. 3.25}$$

$$\oint \rho \vec{v}\vec{v} \cdot d\vec{A} = -\oint pI \cdot d\vec{A} + \oint \bar{\tau} \cdot d\vec{A} + \int_V \vec{F}\, dV \qquad \textbf{Eq. 3.26}$$

Where *p* is the pressure, *I* is the identity matrix, $\bar{\tau}$ is the stress tensor, and $\vec{F}$ is the force vector.

3.1.6.1. Discretization of Momentum Equation

The spatial discretization scheme is also used to discretize the momentum equations. The x-momentum is derived by substituting scalar ϕ with velocity u in Eq. 3.27.

$$a_p u = \sum_{nb} a_{nb} u_{n_b} + \sum p_f A \cdot \hat{\imath} + S \qquad \textbf{Eq. 3.27}$$

In the case where the pressure field p_f and face mass flux is known, the spatial discretization scheme can be performed directly. In most cases, these values are unknown; hence they must be obtained as a part of the solution. Fluent uses a co-located scheme where the velocity and pressure are stored at the cell centres. However, the values at the cell faces are required for the solution. These values are computed using the interpolation scheme. Fluent offers multiple interpolation schemes for different cases including linear, standard, second-order, body force weighted, and PRESTO! Scheme.

Some of the simulations in this work were performed using the default second-order scheme in which the face pressure was reconstructed using the central difference scheme describing the p_f in Eq. 3.27. As the modelling becomes more complex and porous media were introduced, the PREssure Staggering Option (PRESTO!) scheme was then used as recommended for flow involving porous media. The PRESTO! Scheme applies the discrete continuity balance for a "staggered" control volume about the face to compute the face pressure. The PRESTO! scheme can be applied for any mesh type.

3.1.6.2. Continuity Equation Discretisation

The integral form of the continuity equation described in Eq. 3.25 is solved over a control volume to yield the discrete equation Eq. 3.28.

$$\sum_f^N J_f A_f = 0 \qquad \textbf{Eq. 3.28}$$

Where J_f is the mass flux through face f, To complete the solution, the face values of velocity $\vec{v}_n$ are related to the stored values of velocity at the cell centres. This was done by linear interpolation of the cell-centred velocities to the face. Fluent does not average the face velocity linearly; instead, it uses the

momentum-weighted averaging, applying the weighting factors based on the linearization coefficient a_p. The face flux is hence described as,

$$J_f = \rho_f \frac{a_{P,c_0} v_{n,c_0} + a_{p,c_1} V_{n,c_1}}{a_{p,c_0} + a_{P,c_1}} + d_f \left(\left(p_{c_0} + (\nabla p)_{c_0} \cdot \vec{r}_0 \right) - \left(p_{c_1} + (\nabla p)_{c_1} \cdot \vec{r}_1 \right) \right) \quad \textbf{Eq. 3.29}$$

$$= \hat{J}_f + d_f \left(p_{C_0} - p_{C_1} \right) \quad \textbf{Eq. 3.30}$$

Where p_{C_0} and p_{C_1} are the pressures, v_{n,c_0} and v_{n,c_1} are the typical velocities within the two cells on both sides of the face. $\hat{J}_f$ accounts for the influence of velocities in these cells. d_f is a function of a_p for both cells.

3.1.6.3. Pressure-Velocity Coupling

The pressure-velocity was coupled to derive an additional condition for pressure by rearranging the continuity equation. The pressure-based solver made it possible to solve the flow problem in either a segregated or coupled manner. Fluent provides five options of pressure-velocity coupling algorithms to choose from; including, SIMPLE, SIMPLEC, PISO, Coupled, and fractional step (FSM). This work used SIMPLEC for cases that do not require porosity change and PISO for cases that include porous effects.

SIMPLEC

SIMPLEC (SIMPLE-Consistent) is a variation of SIMPLE algorithm. The SIMPLE algorithm applies the relationship between pressure and velocity corrections to ensure mass is conserved and obtain the pressure values. The momentum equation is firstly solved with a guessed pressure p^* value with resultant face flux J_f^* computed as

$$J_f^* = \hat{J}_f^* + d_f \left(p_{c_0}^* - p_{C_1}^* \right) \quad \textbf{Eq. 3.31}$$

If J_f^* does not satisfy the continuity equation, a correction J_f' described in Eq. 3.33 is added to J_f^*. The corrected face flux J_f is computed as,

$$J_f = J_f^* + J_f' \quad \textbf{Eq. 3.32}$$

$$J_f' = d_f \left(p_{c_0}' - p_{C_1}' \right) \quad \textbf{Eq. 3.33}$$

Where p' is the cell pressure correction. SIMPLE algorithm then substitutes Eq. 3.32 and Eq. 3.33 into the discrete continuity equation to derive the discrete equation for pressure correction, described in Eq. 3.34.

$$a_p p' = \sum_{nb} a_{nb} p_{nb}' + b \quad \textbf{Eq. 3.34}$$

Where b is the source term indicating the flow rate into the cell, described in Eq. 3.35.

$$b = \sum_{f}^{N} J_f^* A_f \quad \textbf{Eq. 3.35}$$

The pressure-correction equation was then solved using the AMG method. The cell pressure and face flux are then corrected using Eq. 3.36 and Eq. 3.37, respectively.

$$p = p^* + \alpha_p p' \quad \textbf{Eq. 3.36}$$

$$J_f = J_f^* + d_f\left(p'_{c_0} - p'_{C_1}\right) \quad \textbf{Eq. 3.37}$$

Where α_p is the under-relaxation factor for pressure.

The SIMPLEC algorithm follows a similar procedure as the SIMPLE algorithm. The only difference is the expression used to define the face flux correction J'_f in which the d_f is redefined as a function of $\left(\overline{a_p - \Sigma_{n_b} a_{nb}}\right)$. Using this modified equation accelerates the convergence of solutions involving pressure-velocity coupling.

There are cases whereby the mesh has a degree of skewness. Skewness describes the roughness of the approximate relationship between the difference of pressure correction and the mass flux correction at the cell face. The skewness is corrected by SIMPLEC by recalculating the pressure-correction gradient after the initial solution. The gradient is then used to update the mass flux correction. The SIMPLEC skewness correction allows Fluent to determine the solution on a highly skewed mesh, taking approximately the same number of iterations as a more orthogonal mesh.

PISO

The pressure-implicit with the splitting of operators (PISO) coupling scheme is also a variation of the SIMPLE scheme. It has a higher degree of approximation of the relationship between the correction of pressure and velocity. SIMPLEC is limited because those additional calculations are needed to make the new velocities, and their corresponding fluxes satisfy the momentum balance after pressure-correction. PISO accounts for this by performing two additional corrections: neighbour and skewness correction.

The PISO algorithm moves the repeated calculations required by SIMPLEC into the solution stage of the pressure-correction equation. For cases where the mesh a high degree of skewness, the PISO algorithm recalculates the pressure-correction gradient and uses it to update the mass flux correction. PISO and SIMPLEC algorithm perform similar processes for skewness correction. The skewness and neighbour corrections' simultaneous coupling at the same pressure correction equation may lead to divergence or a lack of robustness. The PISO algorithm may take longer to solve for each iteration, but it will reduce the number of iterations required for convergence.

The simultaneous coupling of the skewness and neighbour corrections at the same pressure correction equation may lead to divergence or a lack of robustness. PISO algorithm enables iterating the skewness correction one or more times for each separate neighbour correction iteration. Although more

computationally expensive, this method allows for a more accurate adjustment of the face mass flux correction according to the normal pressure correction gradient.

3.1.7. Steady-State Iterative Algorithm

To perform a steady-state calculation, the time-dependent terms of the general governing equations are ignored.

3.1.7.1. Under-Relaxation of Variables

The explicit under-relaxation of variables is applied in the pressure-based coupled algorithm for some material properties, momentum, and pressure. Since the equation set being solved by Fluent is non-linear, it is vital to control the change of ϕ. This is achieved by under-relaxation of variables, which limit the change of ϕ produced during each iteration. The new value of ϕ is defined as,

$$\phi = \phi_{old} + \alpha \Delta\phi \qquad \textbf{Eq. 3.38}$$

Where ϕ_{old} is the old value, α is the under-relaxation factor, and $\Delta\phi$ is the change in ϕ.

3.1.7.2. Under-Relaxation of Equation

The pressure-based coupled solver uses the equation's implicit under-relaxation to stabilize the convergence behaviour of the non-linear iterations. The stabilization is done by adding selective amounts of ϕ into the system of discretized equations. The Courant-Frederichs-Levy (CFL) number is a solution parameter in the pressure-based coupled algorithm.

$$\frac{a_p \phi}{\alpha} = \sum_{nb} a_{nb}\phi_{nb} + \frac{a_p \phi_{old}}{CFL} \qquad \textbf{Eq. 3.39}$$

$$\frac{1}{CFL} = \frac{1-\alpha}{\alpha} \qquad \textbf{Eq. 3.40}$$

3.1.8. Time-Advancement Algorithm

Time-dependent flow simulations require the discretized generic transport equation described in Eq. 3.41. The pressure solver in Fluent uses an implicit discretization of the general transport equation. By default, all diffusive, convective, and source terms are solved for the future time step n+1.

$$\int_{cv} \frac{\partial(\rho\phi)}{\partial t} dV + \oint_A (\rho\phi\vec{u})^{n+1} d\boldsymbol{A} = \oint_A (\Gamma_\emptyset \nabla\phi)^{n+1} \, d\boldsymbol{A} + \int_{cv} {S_\emptyset}^{n+1} dV \qquad \textbf{Eq. 3.41}$$

Generally, the time-discretization error of a pressure-based solver is determined by the choice of temporal discretization scheme and the time advancement scheme. Fluent provides two time-advancement schemes, the iterative and non-iterative time-advancement schemes. The scheme selection is made based on the manner in which the splitting error is controlled.

The iterative time advancement scheme was applied for simulations in this work, which involved solving all the equations iteratively for the given time step until the convergence criteria are met. This scheme accounted for the non-linearity of the equations and eliminated the splitting error.

3.1.9. Multigrid Methods

Fluent uses the multigrid scheme to accelerate the convergence by computing corrections on a series of coarse grid levels. Using multigrid significantly reduced the number of iterations taken. Thus reducing the CPU time required to obtain convergence. A set of discrete linear equations is given by:

$$A\phi_e + b = 0 \qquad \textbf{Eq. 3.42}$$

Where ϕ_e is the exact solution, and A is the acceptable level operator. Before convergence, the approximate solution, ϕ is associated with a defect *d*,

$$A\phi + b = d \qquad \textbf{Eq. 3.43}$$

The approximate ϕ was corrected by ψ. The exact solution was then described as

$$\phi_e = \phi + \psi \qquad \textbf{Eq. 3.44}$$

Substituting Eq. 3.42 and Eq. 3.43 into Eq. 3.44 gives

$$A\psi + (A\phi + b) = 0 \qquad \textbf{Eq. 3.45}$$

Substituting Eq. 3.43 into Eq. 3.45 gives

$$A\psi + d = 0 \qquad \textbf{Eq. 3.46}$$

Assuming the relaxation scheme has damped the high-frequency errors, the correction ψ will be solved more effectively on the succeeding coarser level. Solving for the correction on a coarser level needs the defect to be transferred from an adequate level. The correction was then solved on a coarse level and transferred back to the satisfactory level. The equations for correction on a coarse level are written as:

$$A^H\psi^H + Rb = 0 \qquad \textbf{Eq. 3.47}$$

Where, $\psi^H$and A^H is the correction and the operator on a coarse level, respectively. R is the restriction operator used to transfer from the acceptable level. Eq. 3.47 can then be rewritten as:

$$\phi^{new} = \phi + P\psi^H \qquad \textbf{Eq. 3.48}$$

Where P is the restriction operator used to transfer from the coarse level.

The multigrid cycles are recursive processes applied at each grid level as it moves through the grid hierarchy. The V and W are cycles offered by Fluent. The default V cycle was used in the simulations for algebraic multigrid. The cycle revolves around five processes,

- Iteration performed on the current grid level one iteration consists of one forward and one backward Gauss-Seidel sweep.
- The solution is restricted to the next coarser grid level
- The reduction of an error on the course grid
- The computed correction on the course grid interpolated back to the fine grid

- Iterations are known as post-relaxation sweeps performed on the fine grid to eliminate the high-frequency error.

Fluent offers two forms of multigrid, AMG and full approximation storage (FAS). The AMG was applied in this work. The Algebraic multigrid does not require the geometry or re-discretization on the coarse level. AMG is preferable for use in cases with unstructured meshes. The scalar AMG solver is used to solve linear systems of individually discretized transport equations. The coupled AMG solver solves the linearized transport equations using implicit discretization from coupled systems.

$$[A]_{ij}\vec{X}_j = \vec{B}_i \qquad \textbf{Eq. 3.49}$$

Where i influence j. The influence has the form,

$$A_{ij} = \begin{bmatrix} a_{ij}^{11} & a_{ij}^{12} & \dots & a_{ij}^{1N} \\ a_{ij}^{21} & \cdot & & \\ \vdots & & \cdot & \\ a_{ij}^{N1} & & & a_{ij}^{NN} \end{bmatrix} \qquad \textbf{Eq. 3.50}$$

The unknowns and source are defined in form,

$$\vec{X}_j = \begin{bmatrix} x_j^1 \\ \vdots \\ x_j^n \end{bmatrix}, \vec{B}_j = \begin{bmatrix} b_j^1 \\ \vdots \\ b_j^n \end{bmatrix}$$

Eq. 3.49 above was solved using the Gauss-Seidel smoother. The Gauss-Seidel method solves the linear system of equations one at a time in sequence. It uses the previous solutions as soon as they become available for the next one.

3.2. Chemistry Modelling

The modelling of clot initiation and growth is a crucial part of this work. This section describes the method of approach used to simulate these processes. The values of constants and thresholds used will be discussed in the upcoming sections.

3.2.1. User-Defined Scalar (UDS)

Scalars were introduced into the simulation to account for the biochemistry concentration and reactions. The concentration of thrombin, fibrinogen, and fibrin in blood was simulated as scalars flowing in the solution zone, which is the entire vein geometry implemented by Bodnar and Sequeira [94]. Additional variations need to be made in some cases, but, in most cases, Fluent solves the transport equation of a UDS the same way it solves the transport equation of any other scalar. For an arbitrary scalar under convective flux, Fluent solves the transport equation:

$$\frac{\partial(C_i)}{\partial t} + \vec{u} \cdot \nabla(C_i) = \nabla \cdot (\Gamma_i \nabla C_i) + S_i \qquad \textbf{Eq. 3.51}$$

Where C_i represents the concentration of the ith biochemical or "scalar", S_i is its corresponding source or depletion, and Γ_i is its diffusion coefficient.

3.2.2. Biochemical Reactions

This work focuses on the reactions between the biochemical species required for the clotting of blood. A convection-diffusion-reaction approach is taken where the proteins are delivered at the specified boundaries, diffuse around, and then react with one another leading to clot formation. The changes in concentrations of these species are modelled using the Michaelis-Menten equation. The equation describes the reaction between an enzyme E and a substrate S producing product P. In this work, fibrin is produced by the reaction between thrombin and fibrinogen.

$$E + S \Leftrightarrow ES \Rightarrow E + P \quad \textbf{Eq. 3.52}$$

$$\frac{d[P]}{dt} = \frac{k_{cat}[E][S]}{K_m + [S]} \quad \textbf{Eq. 3.53}$$

Where k_{cat} is the catalytic rate constant, and K_m is the Michaelis constant

3.2.3. Porous Media Conditions

Clot growth inflow is simulated in various ways. Bodnar and Sequeira, including other researchers in the field, approached clot formation by changing the clot region's porosity to a different value from the rest of the flow [94]. Other works also approached clot formation by assigning the clot region with a different permeability and viscous resistance [117]. This work took both ideas and used them to model the clot growth. Fluent simulates a porous media by adding a momentum sink to the governing momentum equations, as shown in Eq. 3.54.

By default, Fluent solves the porous media for a single-phase flow using the superficial velocity porous formulation. Where the superficial phase velocities are calculated based on the volumetric flow rate in the porous zone. The porous media are modelled by adding a momentum source term S_i. The source term comprises two parts, the viscous loss term, and the inertia loss term.

$$\frac{\partial(\rho \boldsymbol{u})}{\partial t} = -\nabla \cdot (\rho \boldsymbol{u} \otimes \boldsymbol{u}) - \nabla p + \mu \nabla^2 \boldsymbol{u} + \rho \boldsymbol{g} + S_i \quad \textbf{Eq. 3.54}$$

$$S_i = -\left(\sum_{j=1}^{3} D_{ij} \mu v_j + \sum_{j=1}^{3} C_{ij} \frac{1}{2} \rho |v| v_j \right) \quad \textbf{Eq. 3.55}$$

Where $|v|$ is the magnitude of velocity and D and C are prescribed matrices. The momentum sink influences the pressure gradient in the cell, creating a pressure drop is proportional to the fluid velocity. Eq. 3.55 is then simplified to Eq. 3.56 for a homogenous porous media.

$$S_i = -(\frac{\mu}{\alpha} v_i + C_2 \frac{1}{2} \rho |v| v_i) \quad \textbf{Eq. 3.56}$$

Where α is the permeability and C_2 is the inertial viscous resistance.

3.2.3.1. Darcy's Law

When a fluid flows through a porous zone in a laminar fashion, the pressure drop is proportional to the velocity, and C_2 can be considered equal to zero. The convective acceleration and diffusion can be ignored reducing the porous media to Eq. 3. and describing Darcy's Law.

$$\nabla p = -\frac{\mu}{\alpha}\vec{v} \quad \textbf{Eq. 3.57}$$

The pressure drop can be written in the x, y, z directions as:

$$\Delta p_x \approx \sum_{j=1}^{3} C_{2_{xj}} \Delta n_x \frac{1}{2}\rho|v|v_j \quad \textbf{Eq. 3.58}$$

$$\Delta p_y \approx \sum_{j=1}^{3} C_{2_{yj}} \Delta n_y \frac{1}{2}\rho|v|v_j \quad \textbf{Eq. 3.59}$$

$$\Delta p_z \approx \sum_{j=1}^{3} C_{2_{zj}} \Delta n_z \frac{1}{2}\rho|v|v_j \quad \textbf{Eq. 3.60}$$

Where Δn_x, Δn_x, Δn_x are the thickness of the medium in the x, y, z-direction.

For transient simulations, the effect of porosity is accounted for in the scalar transport equations and continuity equation. The temporal term simply becomes $\frac{\partial}{\partial t}(\gamma\rho\phi)$, where ϕ is the scalar quantity and γ is the porosity.

3.3. Clot Growth Modelling

Under normal blood flow conditions, no clot is formed or exists in the vessel. Clot formation begins when an activation threshold in the flux boundary condition is exceeded, and the clotting cascade is initiated [94]. The clot formation and growth in this model are linked to the concentration of thrombin, which is released as flux from the injury zone on the vein wall. As more thrombin is introduced into the flow, it is consumed by the fibrinogen already present in the blood, and fibrin is produced as explained in the previous section. The concentration of fibrin continues to increase, and when it reaches a threshold value, clot formation initiates in that cell. The porosity and the viscous resistance of the "clotted" cells were changed to simulate the resistance to flow caused by the presence of clot in those cells.

The clot formation in a cell is restricted to two criteria, the concentration of fibrin in the cell must exceed the set threshold value, and the cell must either be by the injury zone where clot formation is assumed to initiate, or it must have at least one clotted neighbouring cell. The coagulation pathways were reduced to initiate clotting only based on the concentration of thrombin present. The thrombin generation begins some seconds after the simulation starts. This allows the flow to stabilize before the biochemical is introduced. The concentration used in this work was derived from literature. Tests assessing the amount of thrombin generated during coagulation have associated limitations. Whole blood tests are being developed to clinically determine the amount of thrombin in blood. The use of a thrombogram is one

of the most accessible research-based tests to reliably measure the thrombin concentration during different stages of coagulation [118]. A calibrated automated thrombogram (CAT) was developed by Hemker et al., showing the concentration of thrombin in a patient's blood over time. The CAT was used to determine if the patient was in a hypercoagulable or hypo coagulable state [119]. A thrombin generation curve shown in was later defined by an Eq. 0.**Error! Reference source not found.** developed by Kremer et al. [120].

$$|TH| = 1 \times 10^{-9} \times \left(h \times P \times e^{\left(-h \times \left(\frac{t}{60} - TTP\right)\right)} \times \frac{P}{ETP} \times e^{\left(-e^{\left(-h \times \left(\frac{t}{60} - TTP\right) \times \frac{P}{ETP}\right)}\right)} \right) \quad \textbf{Eq. 3.61}$$

Where: P is the peak thrombin concentration

ETP is the endogenous thrombin potential

TTP is the time to peak

h is a constant = 2.7272

t is the time in seconds

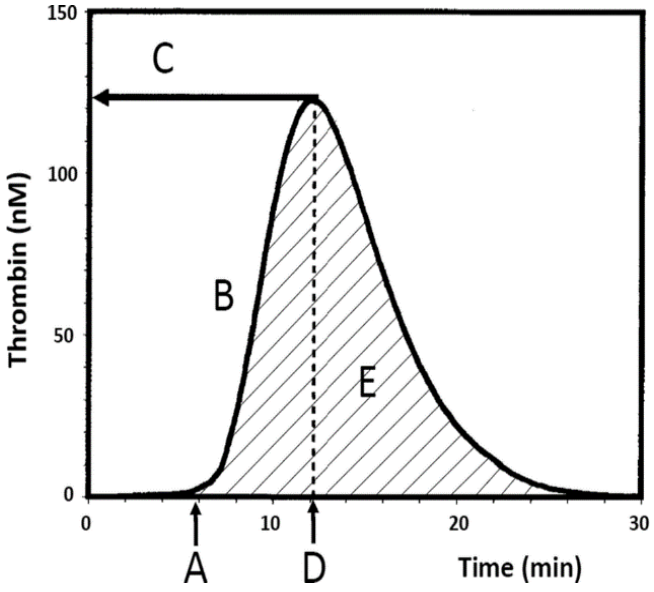

Figure 3.3: Thrombin Generation Curve shown on thrombogram as a function of time. A = Lag time (min), B = Maximal rate (nM/min), C = Thrombin Concentration peak, D = Time to peak, and E = endogenous thrombin potential (ETP) [118].

3.3.1. Experimental Validation Methods and Materials

Materials and Devices

Fibrinogen from human plasma 50-70% protein with ≥80% of clottable protein (Sigma Aldrich, Saint Louis MO USA) was received in powder form with solubility 10 mg/mL. It was then diluted in Dulbecco's Phosphate Buffered Saline (Sigma Aldrich, Saint Louis MO USA) to a concentration of 100mg/L. The calcium and magnesium in the saline facilitate cell binding and clumping a characteristic

needed for clot formation. Thrombin from human plasma (Sigma Aldrich, Saint Louis MO USA) was diluted in the saline to concentration 100mg/L.

The experimental setup shown in Figure 3.4 includes the following parts and devices:

- Flow phantom (a 10mm ID clear PVC pipe, Length 80 mm) with a 1mm hole 40mm from the inlet to serve as the thrombin inlet.
- A Masterflex® L/S variable speed analogue console peristaltic pump.
- An NE-300 Just Infusion™ Syringe Pump.
- A Leica V-Lux 5 digital camera.

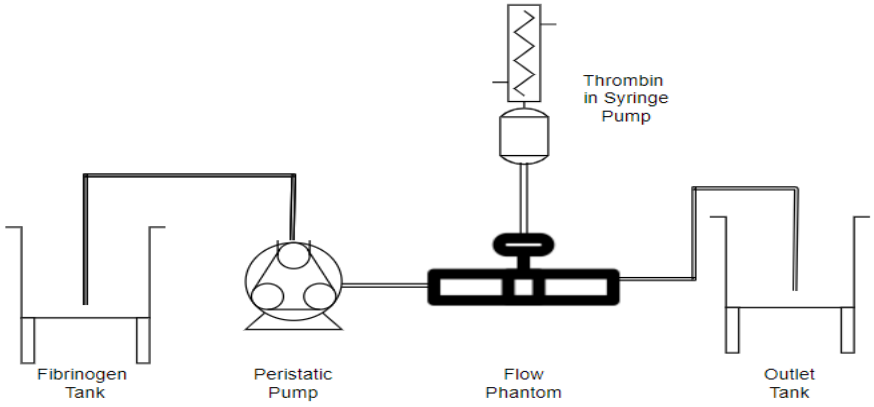

Figure 3.4: Illustration of Experimental Setup

4. PARAMETRIC STUDY OF TWO-DIMENSIONAL DVT MODEL

Modelling cardiovascular vessels using CFD is beneficial in the development and effectiveness of the treatment for cardiovascular disease. The optimization of the parameters involved in clot formation in DVT is an important step in model development. This chapter describes the parametric study of vein diameter, blood velocity, and thrombin concentration in a two-dimensional geometry. Blood flow transports protein to the injury site where clot formation initiates, obstructing flow. The model is simplified and will serve as a basis for developing more complex models to be discussed in the following chapters. Simplification allows for the effects of the changing parameters to be identified.

4.1. Overview

CFD modelling of cardiovascular diseases has been a promising development in medical imaging applications. There are speculations that CFD modelling and simulations could be used in conjunction with imaging techniques to produce systematic predictions of different cases of surgery and treatment outcomes for clinical environment. The modelling process begins with an idealized or simplified model with which the parameters and constraints are optimized. The models require reliable parameter inputs that are derived experimentally. The optimization is then used with a patient-specific model to enable a customized treatment regime for patients [121]. This optimization process was used mainly by traditional disciplines such as automotive and aeronautics design and was recently introduced into cardiovascular medicine.

Medical devices such as stents, ventricular assist devices, and coil placement involve a form of geometry or shape optimization. Parameter identification enables the obtainment of a patient-specific model using control theory methods. The information extracted from the medical images is maximised in the context of material property identification. For models involving fluid-structure interaction, viscoelasticity is used to accurately simulate the effects of surrounding tissue, vessels, and organs on fluid flow.

The process of blood clot formation is complex and is dependent on interactions between multiple biochemical species. The clot formation initiation results from platelets getting trapped in a fibrin mesh, forming a large solid mass known as thrombus. The work described in this chapter modelled the formation and growth of the fibrin mesh based on the transport of the biochemical species as done by Mann [75] and Bodnar and Sequeira [94]. The coagulation cascade's complexity was reduced to one reaction, simplifying the model and making it easier to use. The effect of the platelets is included by varying the porosity of areas that have clotted due to fibrin formation. Although values for parameters used in previous models are derived experimentally, few sources describe the actual effect of different parameters on the initiation and propagation of clots. This work answers some of those questions by

investigating the impact of three parameters (blood velocity, vein diameter, and thrombin concentration) on the size and shape of the clot formed at the injury site. An idealized two-dimensional model of the femoral vein was employed.

4.2. Modelling Process

The modelling processes of a typical haemodynamic CFD case were described previously. Figure 4.1 below describes these processes.

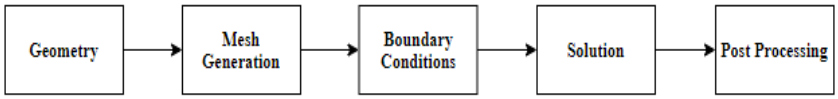

Figure 4.1: Processes of modelling a Haemodynamic CFD case.

The acquisition of data was an important stage of the modelling process. The simplicity involved makes it possible to derive all the data used for the model discussed in this section from literature. The essential data acquired are the velocity of blood, the blood pressure, and the vein's geometry.

4.2.1. Vein Geometry

The geometry of the vein is derived from literature. Clinically, multiple methods could be used to determine the shape of the vein. Hayakawa *et al*. applied a B-mode ultrasound diagnostic device to determine the diameter of the femoral vein of a person breathing normally in a sitting position [56]. The diameter was measured as the distance between the vein lumen at its rest position.

Lattimer *et al*. used duplex evaluations of a linear transducer attached to an ultrasound machine to determine the diameter of the femoral vein of patients with no evidence of venous disease [54]. The patients were examined in the standing position with their hips supported by a couch while the other leg carried the body weight. This position was chosen to allow the gravitational force to act and ensure the leg veins are fully expanded. To determine the hemodynamic changes that occur when the femoral vein is under increased outflow resistance, they attached a high thigh cuff that inflates and deflates to the patient's legs to work in conjunction with the intermittent pneumatic compression (IPC) device attached on the calf. Fronek et al., also determined the common femoral vein's diameter using a duplex ultrasonography evaluation [51]. The evaluations done by Lattimer *et al*. [54] and Fronek *et al*. [51] differ in that the patients in Fronek *et al*. evaluation were on a tilted table, resting comfortably in a flat position, and were performing the Valsalva manoeuvre.

The measurements from the above works are considered in this section. These evaluations account for prominent leg positions: standing, sitting, and supine. The simplicity of the model allows for the idealization of geometry. The complex shape of the vein was simplified to be a rectangle representing a cylinder with properties shown in Table 4. The length of the simulated vein was the distance between

two venous valves. Figure 4.2 indicate that the 2D geometry is asymmetric and the injury site was 50% of the vein length.

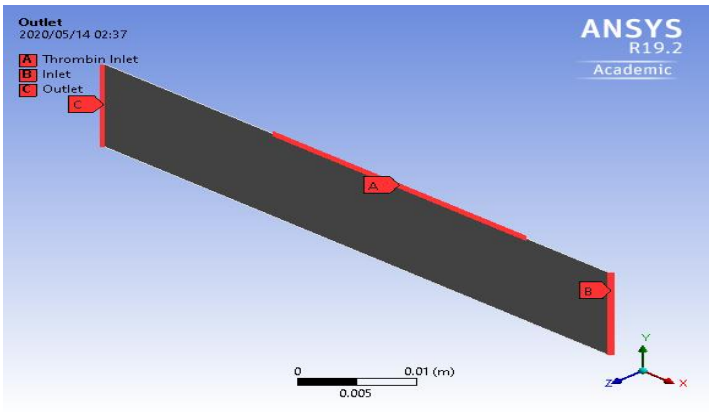

Figure 4.2: Idealized 2-D geometry of vein. A is the thrombin inlet; B is the inlet, and C the outlet.

4.2.2. Blood Velocity and pressure

The velocity data used for this model is acquired from literature. Lattimer *et al*. and Fronek *et al.* determined the velocity of blood in the femoral vein using duplex ultrasonography in positions mentioned in Section 4.2.1 [51], [54]. In both cases, the velocity profiles were analysed, the time-averaged maximum flow velocity (TAMV), and the mean peak velocities are determined. The mean peak velocity values are used in this section. An invasive approach to measuring the venous flow velocity developed by Coffman and Lempert is also considered in this model [54]. This prevents the restriction of the data sample to ultrasonography. Coffman and Lempert determined the velocity by measuring albumin's transit time from the calf to the inguinal region. A catheter was used to inject the dosage of albumin required at the ankle. A scintillation probe was placed over the femoral vein to record the radioactive count. The velocity was determined from the time of injection to the initial rise in radioactivity. The inlet velocity and Reynolds number are shown in Table 3.

Table 4: Geometric and flow properties for idealized geometry.

Properties	**Values**
Vein Diameter (mm)	11.84 [51]
	11.2 [54]
	9.76 [56]
Vein Length (mm)	60
Thrombin Inlet Length (mm)	30
Thrombin Inlet distance from Inlet (mm)	10
Inlet Blood Velocity (m/s)	0.122
Reynolds Number	380

Not many researchers have attempted to measure blood pressure in the femoral vein, instead, the body mean pressure is used [53], [57]. Kurstjens *et al.* used an ultrasonic machine and a pressure monitoring set to study the changes in blood pressure in the common femoral veins of patients with post-thrombotic deep venous obstruction [58]. The study measured the pressure for both the affected and non-affected limb. The data for the non-affected limb was used in this model.

Hagen Poiseuille profile was used to describe the velocity at the inlet of the vein. The equation Eq.4.1 represents the velocity.

$$v = V_m\left(1 - \frac{r^2}{R^2}\right) \qquad \textbf{Eq.4.1}$$

Where,

$$r = \sqrt{x^2 + y^2} \qquad \textbf{Eq.4.2}$$

V_m is the maximum velocity, r is the distance from the centre, and R is the vessel's radius.

4.2.3. Grid Independence Test

A grid independence test (GIT) was performed to improve the quality of results by running calculations using successively smaller cell sizes. The test determines the most suitable meshing method and meshes size for the model. Velocity and pressure were monitored, and these values are more accurate using finer mesh. However, running calculations using finer meshes is computationally expensive. The grid independence test is performed to find the balance between the results' accuracy and the computational expense.

The test for this model was done in two sections. The steady-state GIT was done to choose the meshing method and size required to attain stable blood flow. The transient state GIT was then performed to determine the mesh size, giving the most accurate bio-chemical release accounting for CPU time.

4.2.3.1. Steady State GIT

Steady-state GIT was performed using four mesh sizes with 750, 2500, 5000, and 7500 elements, respectively. Two mesh methods are applied: tetrahedral and multizone. Outlet flow velocity and pressure were monitored to evaluate the adequate mesh size and method. The vein was initially a cylindrical pipe of length 60 mm, considering the distance between the valves. Inlet velocity was considered a parabolic flow as it would not be formed due to short vein length. In each mesh size case, the test was performed on geometries with three vein diameters, shown in Table 4. The average percentage error in the outlet velocity over a line drawn across the geometries' centre was measured.

Table 5: Steady-state grid independence test result summary for the geometries.

Steady State Mesh Independence Test						
Geometry 1						
	No of Elements	No of Nodes	Element Size (mm)	Average Outlet Velocity (m/s)	Maximum Velocity (m/s)	% Error Compared to Next Finer Mesh
Mesh 1	780	837	2.000	0.0810	0.121	1.3130
Mesh 2	2660	2772	0.800	0.0812	0.121	1.0345
Mesh 3	5280	5445	0.500	0.0813	0.122	0.4748
Mesh 4	7500	7701	0.400	0.0813	0.122	
Geometry 2						
	No of Elements	No of Nodes	Element Size (mm)	Average Outlet Velocity (m/s)	Maximum Velocity (m/s)	% Error Compared to Next Finer Mesh
Mesh 1	754	810	2.200	0.0811	0.1215	1.0049
Mesh 2	2448	2555	0.850	0.0812	0.1216	1.0136
Mesh 3	4998	5160	0.490	0.0813	0.1217	0.6760
Mesh 4	7595	7800	0.390	0.0813	0.1217	
Geometry 3						
	No of Elements	No of Nodes	Element Size (mm)	Average Outlet Velocity (m/s)	Maximum Velocity (m/s)	% Error Compared to Next Finer Mesh
Mesh 1	750	806	2.000	0.0810	0.1205	0.9203
Mesh 2	2574	2686	0.770	0.0811	0.1211	1.0735
Mesh 3	5125	5292	0.485	0.0813	0.1215	0.5740
Mesh 4	7567	7776	0.375	0.0813	0.1216	

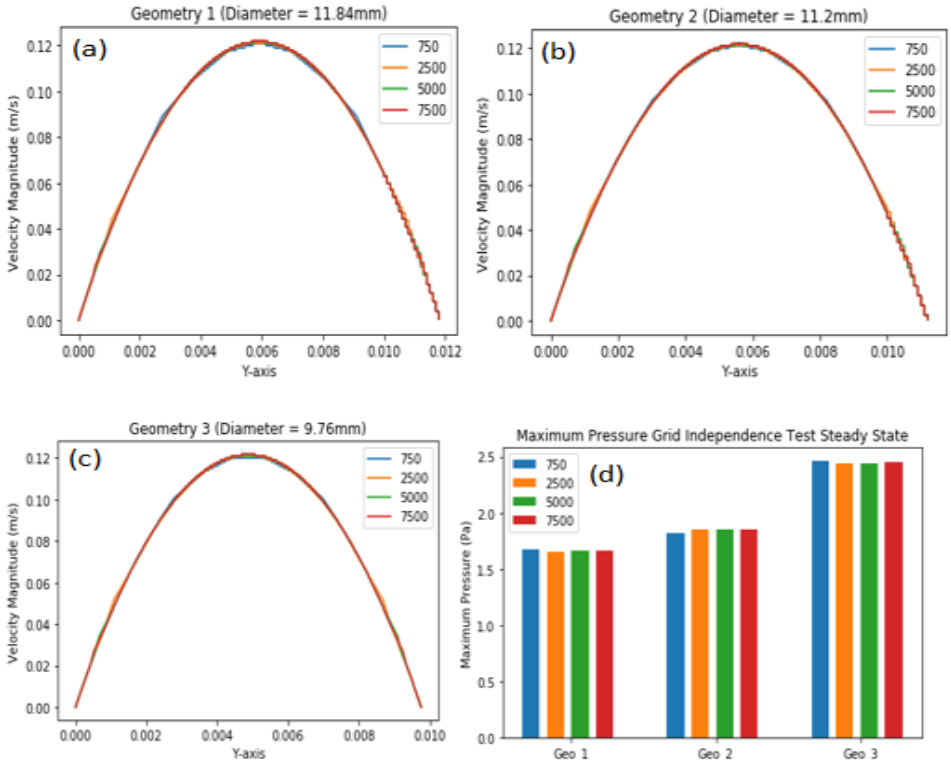

Figure 4.3: Steady-state grid independence test results. (a-c) show the parabolic velocities for the three geometries at four different mesh sizes. (d) Inlet pressure for the three geometries at different mesh sizes

A solution is assumed to be grid independent when the percentage error between the mesh and the next finer mesh is less than 1%. The geometries tabulated results show that the parabolic flow solutions become grid independent at 5000 elements for Geometries 1 and 2 and 750 elements for Geometry 3.

4.2.3.2. Transient State

The transient bio-chemistry grid independence test was performed by measuring the thrombin concentration over time using a point probe placed 5×10^{-5} m away from the centre of the injury zone. The vein geometries from steady-state analysis are maintained in transient GIT. Fifteen inflation layers were made at the walls to increase the solution's accuracy at cells closer to the walls. The mesh element size was varied over range 7500 – 30000 elements. And *dt* values 0.1, 0.5, and 1s were applied. The thrombin generation profile described in Eq. 3.61. was applied. Thrombin concentration was simulated as a scalar with diffusivity of $6.47 \times 10^{-11}\ m^2\ /\ s$. The thrombin generation peak used was 118 nm, ETP was 1648, and the TTP was 4 min. For each grid size, three timesteps were implemented.

As indicated in Figure 4.4 and Table 6 The Geometry 1 solution was observed to be grid independent at 7500 elements and *dt* = 0.1 s. To acquire precise results, the same grid size used for the geometries should be the same. The three geometries were grid independent at 30000 elements and *dt* = 0.5 s.

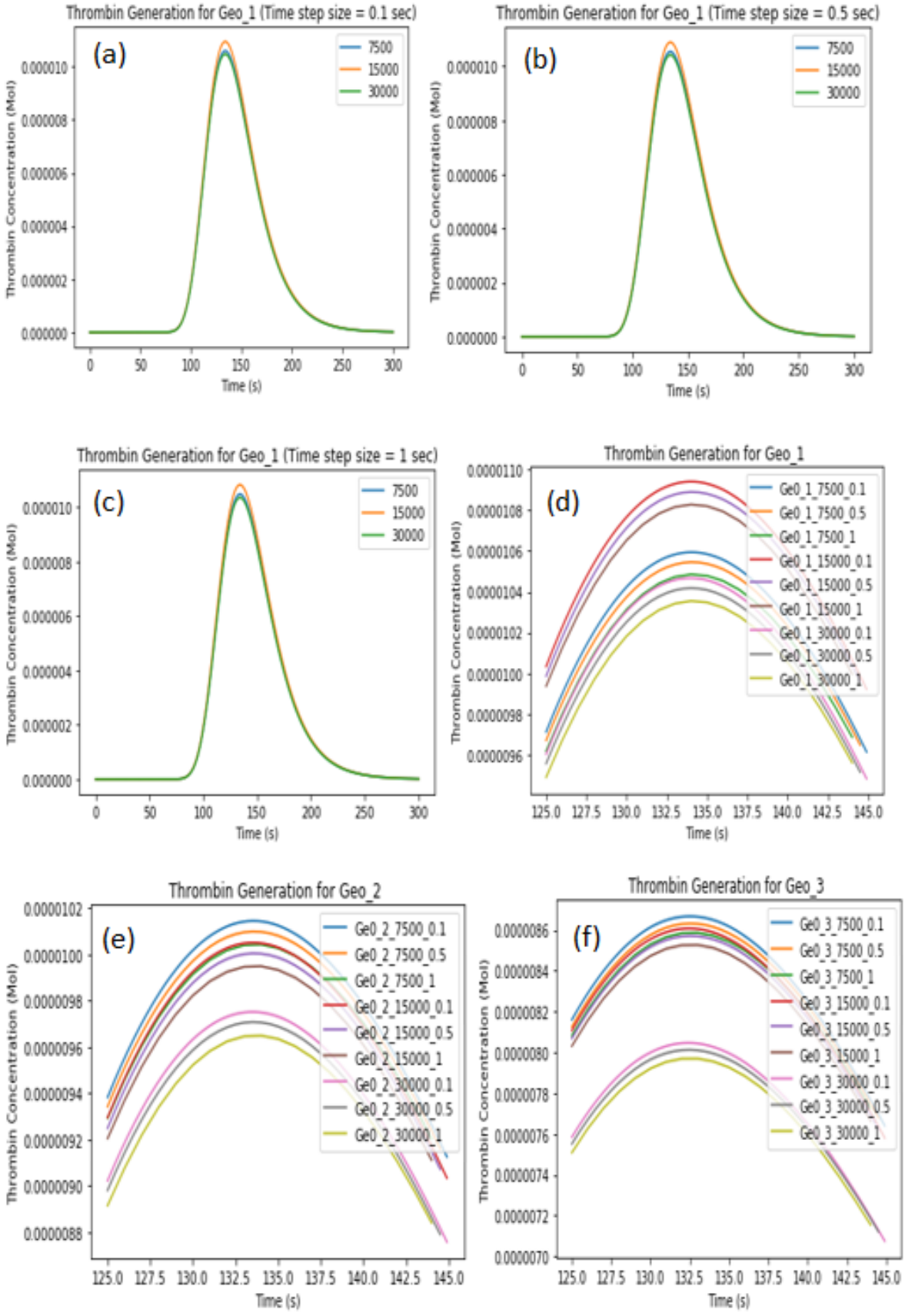

Figure 4.4: Transient state grid independence test results. a-c showing the thrombin concentration at point probe for geometry 1 at time steps 0.1 s, 0.5 s, and 1s. d-f is showing the magnified peaks of the curves for geometry 1, 2, and 3.

Table 6: Transient state grid independence test result summary for the geometries.

Mesh	Courant Number	Peak Thrombin Concentration [Mol]	Average Thrombin Concentration [Mol]	% Error
Ge0_1_7500_1	0.4379	1.05E-05	2.186E-06	0.18
Ge0_1_7500_0.5	0.2190	1.05E-05	2.189E-06	0.75
Ge0_1_7500_0.1	0.0438	1.06E-05	2.192E-06	1.22
Ge0_1_15000_1	0.4487	1.08E-05	2.255E-06	3.46
Ge0_1_15000_0.5	0.2243	1.09E-05	2.258E-06	4.04
Ge0_1_15000_0.1	0.0449	1.09E-05	2.261E-06	4.53
Ge0_1_30000_1	0.4454	1.04E-05	2.153E-06	1.07
Ge0_1_30000_0.5	0.2227	1.04E-05	2.155E-06	0.47
Ge0_1_30000_0.1	0.0445	1.05E-05	2.159E-06	0.00
Ge0_2_7500_1	0.4808	1.00E-05	2.088E-06	2.98
Ge0_2_7500_0.5	0.2404	1.01E-05	2.092E-06	3.56
Ge0_2_7500_0.1	0.0481	1.01E-05	2.095E-06	4.02
Ge0_2_15000_1	0.4686	9.95E-06	2.064E-06	2.02
Ge0_2_15000_0.5	0.2343	1.00E-05	2.068E-06	2.59
Ge0_2_15000_0.1	0.0469	1.00E-05	2.071E-06	3.06
Ge0_2_30000_1	0.4703	9.65E-06	2.000E-06	1.05
Ge0_2_30000_0.5	0.2352	9.71E-06	2.002E-06	0.45
Ge0_2_30000_0.1	0.0470	9.75E-06	2.005E-06	0.00
Ge0_3_7500_1	0.5502	8.59E-06	1.773E-06	6.72
Ge0_3_7500_0.5	0.2751	8.63E-06	1.775E-06	7.28
Ge0_3_7500_0.1	0.0550	8.67E-06	1.777E-06	7.72
Ge0_3_15000_1	0.5442	8.53E-06	1.758E-06	5.97
Ge0_3_15000_0.5	0.2721	8.57E-06	1.761E-06	6.53
Ge0_3_15000_0.1	0.0544	8.61E-06	1.763E-06	6.98
Ge0_3_30000_1	0.5393	7.97E-06	1.639E-06	0.96
Ge0_3_30000_0.5	0.2696	8.01E-06	1.642E-06	0.41
Ge0_3_30000_0.1	0.0539	8.05E-06	1.644E-06	0.00

4.2.4. Flux vs. Value Investigation

The thrombin generation equation (Eq. 3.62) incorporated into Fluent as a User-defined function (UDF). The profile is simulated as either a value or a flux. This section describes an investigation into the difference between two options and which option is selected for the model. Neeves *et al*. proposed that thrombin should be generated at the injury zone as a flux [114]. However, the equation describing the profile only supplies Fluent with the thrombin concentration value $|TH|$ at any given time.

Geometry 1 was applied for this investigation with a parabolic velocity profile at the inlet and zero-gauge pressure at the outlet. Thrombin was generated at the injury zone, and the simulation was run for 300 seconds. Point probes were placed at points 0.05, 0.06, 0.07, 0.08, 0.09, and 0.1 mm from the injury wall to measure the concentration at those points. This is done to study how far into the vein the thrombin diffuses and how much thrombin diffuse. The maximum thrombin concentration throughout the geometry was monitored.

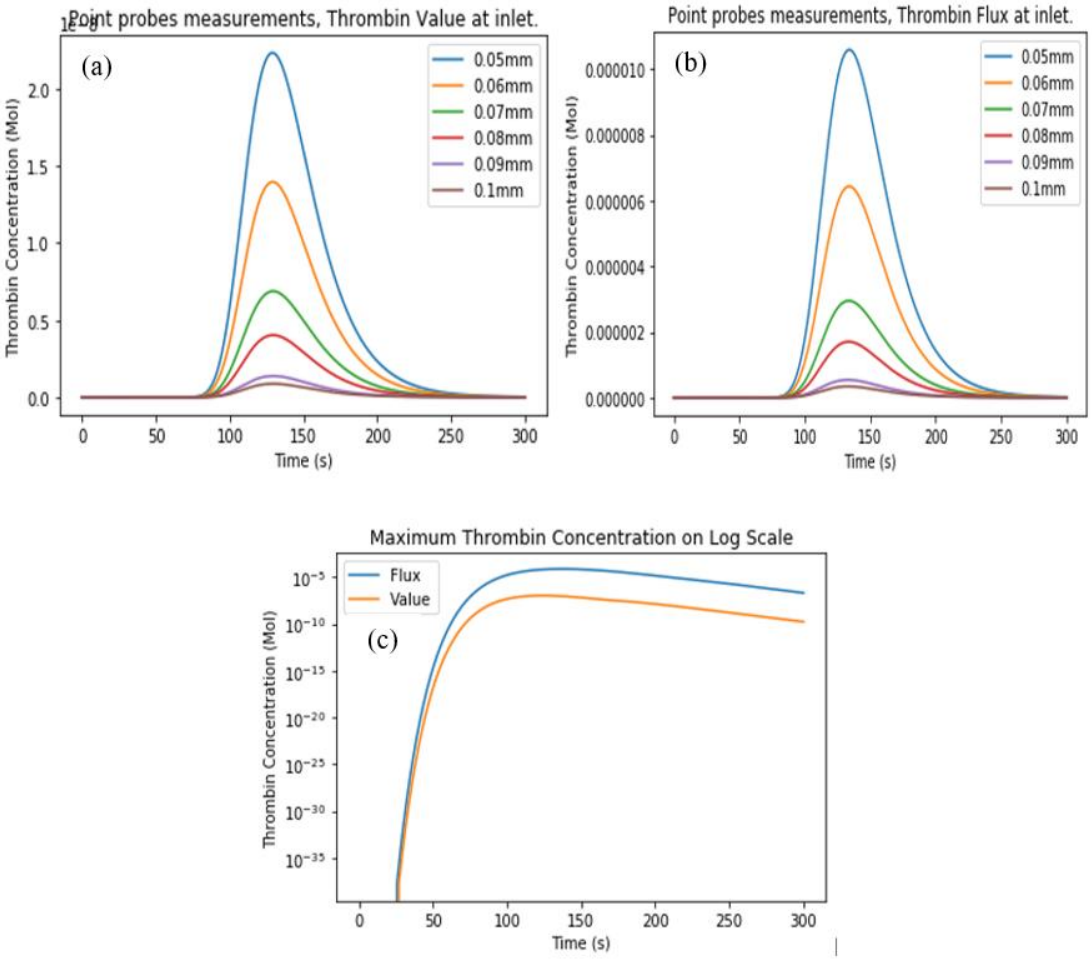

Figure 4.5: Point probes thrombin concentration measurements different distances from the injury site for (a) value (b) flux boundary conditions at thrombin inlet. (c) comparing maximum thrombin concentration in the vein between both boundary conditions on a logarithmic scale

The thrombin concentration reduces as the distance from the wall increases, as shown in Figure 4.5. Figure 4.5 also shows that the isotropic diffusion of thrombin is not related to generating a flow method. For both cases, thrombin diffused downwards by a similar trend. The significant difference between the two cases was the concentration at which thrombin was generated. In the case of value, thrombin was generated at the exact amount dictated by equation Eq. 3.63. However, Fluent generates the defined amount of thrombin into the flow at every timestep when using flux. This difference was explained by understanding that Fluent sets the concentration of thrombin on that surface as the defined value when using the value method. It uses diffusivity to solve for how much and how far thrombin travels. However when using flux, Fluent generates the defined amount of thrombin into the flow at every timestep. Therefore, the concentration of thrombin varies for different timestep sizes.

Figure 4.5 shows the maximum concentration of thrombin in both cases on a logarithmic scale. The maximum concentration when using flux boundary condition was about 700 times higher when applying value boundary conditions. As recommended by Neeves *et al*. thrombin in this model was introduced into the flow as a flux [114]. However, alterations were made to the generation profile equation to reduce the amount of thrombin generated accordingly. Eq. 3.64 was adjusted to account for the area and the change in time involved in convective flux. Eq.4.3 describes the updated equation:

$$|TH| = \frac{1 \times 10^{-9} \times \left(h \times P \times e^{\left(-h \times \left(\frac{t}{60} - TTP\right)\right)} \times \frac{P}{ETP} \times e^{\left(-e^{\left(-h \times \left(\frac{t}{60} - TTP\right) \times \frac{P}{ETP}\right)}\right)} \right)}{AREA \times dt} \qquad \textbf{Eq.4.3}$$

Where *AREA* is the injury zone area which stays constant throughtout the simulation.

4.2.5. Deep Vein Thrombosis Model Boundary Conditions

The model has four defined boundaries: inlet, outlet, thrombin inlet, and the vein wall. The boundary conditions specify the flow and thermal variables on the boundary.

4.2.5.1. Wall Boundary Conditions

There were two wall boundaries in this model, namely the vein wall and the thrombin inlet (injury zone). The walls are rigid, stationary, and no-slip shear conditions were enforced. A specified flux condition is set at the thrombin inlet to represent the thrombin generation at the wall as a user-defined scalar.

4.2.5.2. Velocity Inlet Boundary Conditions

The velocity inlet condition is used to define the flow velocity and the scalar flow properties at the vein inlet. The total pressure (stagnation) is not fixed and rises to the value necessary to achieve the prescribed velocity distribution. The parabolic velocity profile is specified to give the velocity magnitude normal to the boundary. An absolute reference frame is used, and the initial gauge pressure was constant at zero pascal. A specified zero thrombin flux condition is set at the inlet to ensure that thrombin is only generated from the vein's injury zone.

4.2.5.3. Pressure Outlet Boundary Conditions

The pressure outlet boundary conditions are used to define the gauge (static) pressure at the vein's outlet. Gauge pressure was used because the flow was subsonic. The "backflow" condition is specified for flow in the reverse direction at the pressure outlet during the simulation.

4.2.6. Numerical Solving Parameters

The two-dimensional model described in this chapter accounts for thrombin transport from the injury site and relates this to the cells' permeability and porosity. The simulations conducted in this chapter are derived from varying the velocity, vein diameter, and peak thrombin concentration. The effects of these parameters on the size and shape of the clot formed are studied.

Blood is assigned a density of 1050 kg/m^3 and a viscosity of 0.004 kg/ms. The flow is considered laminar and incompressible. Thrombin is introduced into a flow as a scalar with a diffusivity of $6.79 \times 10^{-8}\ kg/ms$. The clot formation in the model is achieved by decreasing the porosity after the set threshold had been exceeded. The porosity is 1 when the threshold had not been exceeded and changed to 0.75 when the clot is formed. Viscous resistance (inverse absolute permeability) also follows a similar relationship. Its value changes from $1 \times 10^{-12}\ m^{-1}$ when the clot is not formed to $1 \times 10^{12}\ m^{-1}$ when the clot forms. The PISO scheme is used to solve the pressure-velocity coupling with skewness and neighbour correction factors of 1. Table 7 below indicates all the simulations are done and the input parameters. With the notation G(1, 2, 3)_T(L, M, H)_V(L, M, H) indicating the geometry(G) being 1, 2, or 3, thrombin concentration (T) and velocity (V) being low, middle, or high.

Table 7: Simulation names and the parameters used for each simulation carried out in this study. With the notation G(1, 2, 3)_T(L, M, H)_V(L, M, H) indicating the geometry(G) being 1, 2, or 3, thrombin concentration (T) and velocity (V) being low, middle, or high

Name	Diameter (mm)	Peak Thrombin Concentration (nMol)	Peak Velocity (m/s)	Time Step Size (s)
G1_TL_VH	11.84	50	13.87	0.1
G1_TL_VM	11.84	50	12	0.1
G1_TL_VL	11.84	50	9.8	0.1
G1_TM_VH	11.84	118	13.87	0.1
G1_TM_VM	11.84	118	12	0.1
G1_TM_VL	11.84	118	9.8	0.1
G1_TH_VH	11.84	200	13.87	0.1
G1_TH_VM	11.84	200	12	0.1
G1_TH_VL	11.84	200	9.8	0.1
G2_TL_VH	11.2	50	13.87	0.5
G2_TL_VM	11.2	50	12	0.5
G2_TL_VL	11.2	50	9.8	0.5
G2_TM_VH	11.2	118	13.87	0.5
G2_TM_VM	11.2	118	12	0.5
G2_TM_VL	11.2	118	9.8	0.5
G2_TH_VH	11.2	200	13.87	0.5
G2_TH_VM	11.2	200	12	0.5
G2_TH_VL	11.2	200	9.8	0.5
G3_TL_VH	9.76	50	13.87	0.5
G3_TL_VM	9.76	50	12	0.5
G3_TL_VL	9.76	50	9.8	0.5
G3_TM_VH	9.76	118	13.87	0.5
G3_TM_VM	9.76	118	12	0.5
G3_TM_VL	9.76	118	9.8	0.5
G3_TH_VH	9.76	200	13.87	0.5
G3_TH_VM	9.76	200	12	0.5
G3_TH_VL	9.76	200	9.8	0.5

4.2.7. Velocity Contour

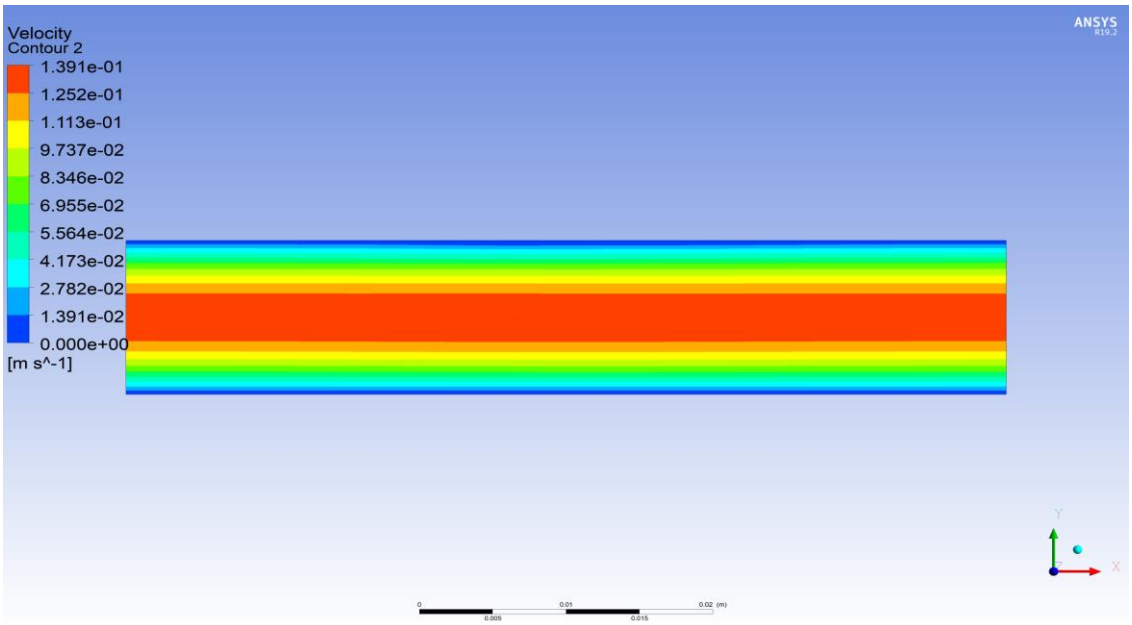

Figure 4.6: Velocity contour at 250s

As illustrated in Figure 4.6, the fully formed parabolic velocity profile set at the inlet applies throughout the vein's length. A vertical line probe drawn at the centre of the injury site is used to measure the velocity and track the clot's thickness. Figure 4.7 shows the velocity against the Y-axis plot at times 50, 100, and 250s. up to 50s, the clot has not been initiated; at 100s, the clot is growing, and at 250s, the clot is fully grown. As illustrated, the clot obstructs blood flow close to the wall. The growth of the clot was not significantly high to cause a significant change to the parabolic profile. Instead, it slightly shifts the position of the peak velocity off-centre. Similar velocity contours were noticed in all the simulations made, with the significant difference being the clot's size.

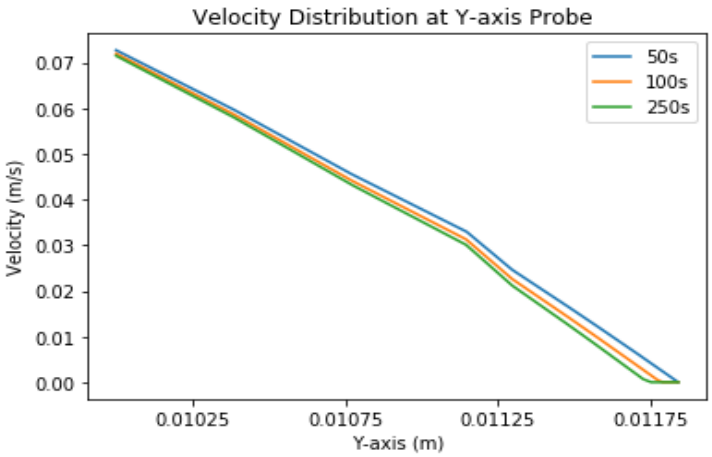

Figure 4.7:Velocity Distribution at the vertical probe in the centre of the injury site.

4.2.8. Pressure Contour

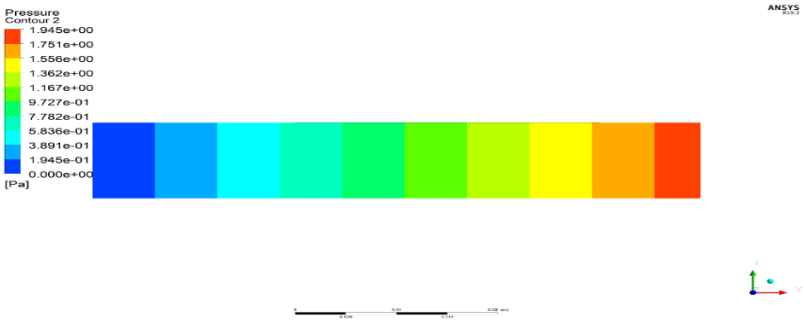

Figure 4.8: Pressure Contour at 50s.

As illustrated in Figure 4.8, the pressure decreases linearly from 1.945 Pa at the inlet to zero at the outlet. The formation of the clot barely affected the pressure distribution.

4.2.9. Thrombin Concentration Contour

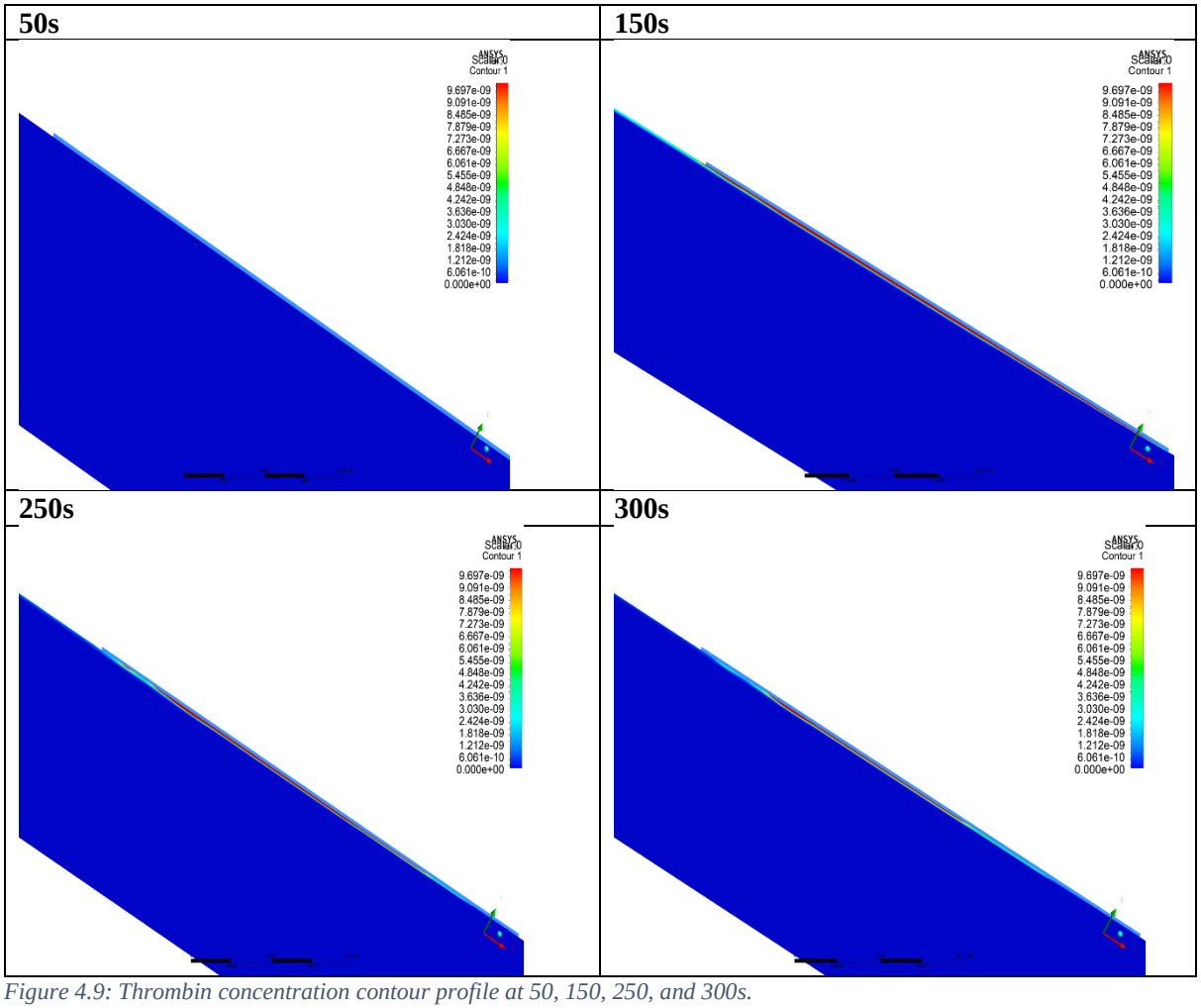

Figure 4.9: Thrombin concentration contour profile at 50, 150, 250, and 300s.

Figure 4.9 shows the thrombin concentration contour at different times in the simulation. Thrombin close to the wall was transported away from the injury site slowly as the velocity in this area approached zero.

4.2.10. Maximum Thrombin Concentration

The maximum thrombin concentration over the vein was also monitored. Figure 4.10 illustrates the different peak thrombin concentrations for Geometry 1. A similar pattern is seen in Geometry 2 and 3. Velocity change has little effect on the peak thrombin concentration; however, the rate at which the thrombin concentration drops increased as the velocity increased. The peak thrombin concentration was higher than the defined value due to clot growth during the thrombin generation. The clot obstructs flow, trapping some thrombin and increasing thrombin concentration close to the wall. The effect of geometry change on maximum thrombin concentration is illustrated in Figure 4.11. The change in vein's diameter does not affect the maximum thrombin concentration.

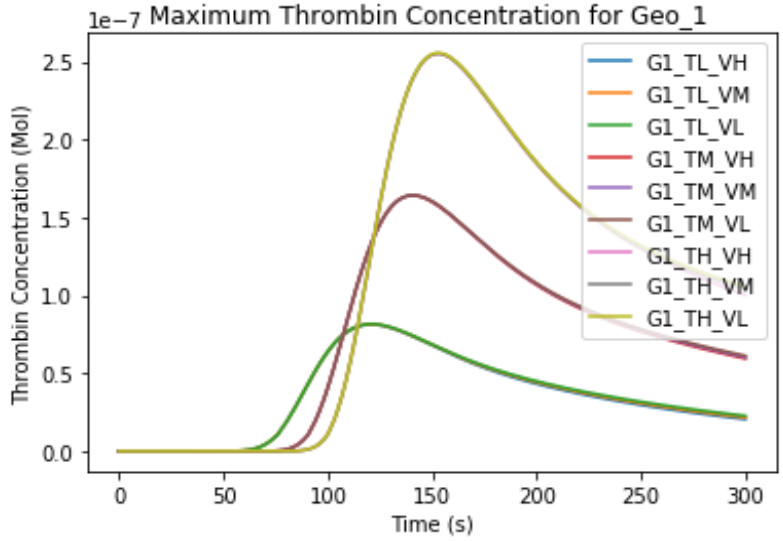

Figure 4.10: Maximum thrombin concentration for cases with geometry 1. Note the overlay of graphs with the same thrombin concentration.

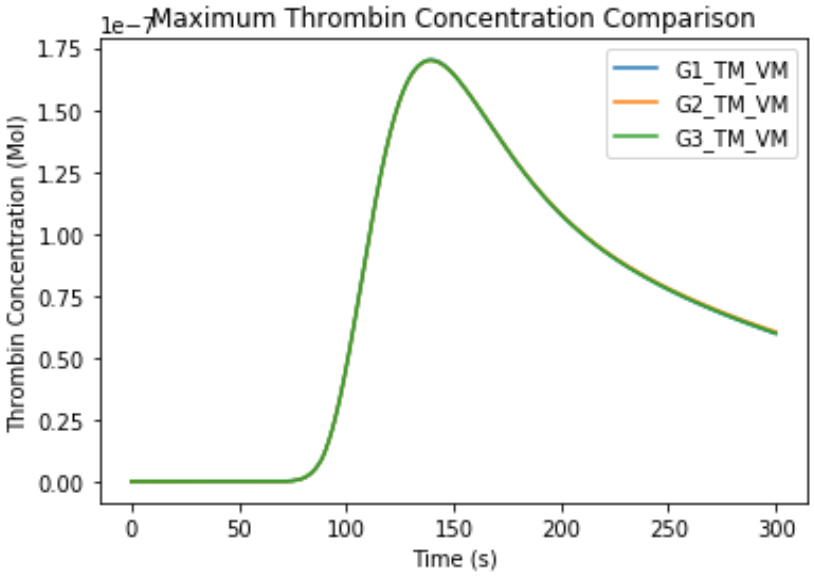

Figure 4.11: Comparison of maximum thrombin concentration between geo 1,2, and 3 at middle thrombin peak and velocity.

4.2.11. Clotting Process

The parametric study was done by measuring the clot's size formed in the different cases after 300 seconds when the clot is fully formed. The clotted area was described by a UDS that switches from zero to 1 when the cell has clotted. Since the elements are not the same size due to the inflation layers bounded by the vein walls, the clotted area was measured by finding the weighted average of the clot over the total vein area.

4.2.11.1. Effects of Velocity Change on Clot Size

Figure 4.12 and

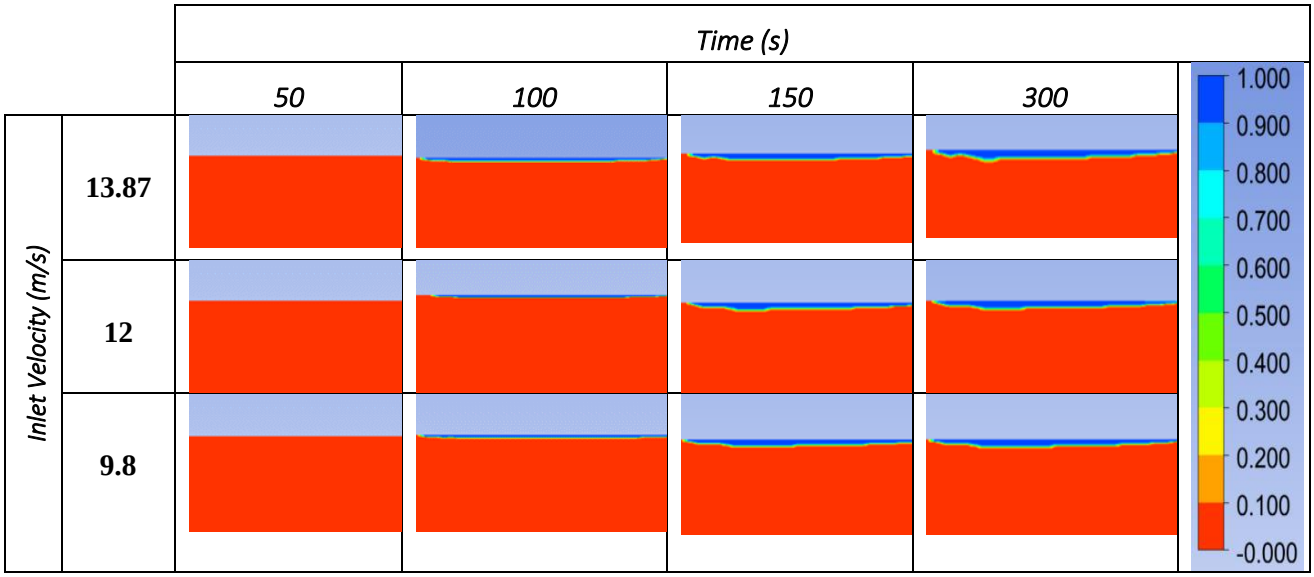

Figure 4.13 illustrates the clot sizes with changing velocities. The clot size decreases as the velocity increases. A 13.5% reduction in velocity led to a 2% increase in clot size, and a 30% decrease in velocity gave a 4% increase in clot size. Clot formation initiated at 75.5s for all three cases, proving that the velocity does not affect the clot initiation. The clots were fully formed at 155.3s for G1_TL_VH, 155.1s for G1_TL_VM, and 156s for G1_TL_VL.

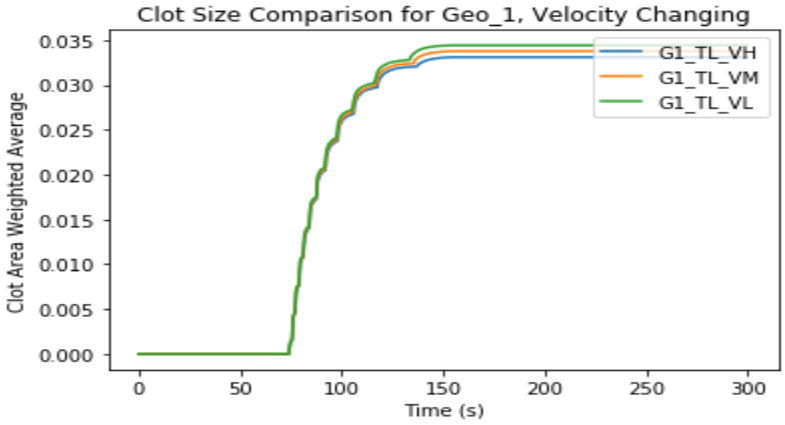

Figure 4.12: Graph comparing clot sizes in Geometry 1 at different velocities over 300s.

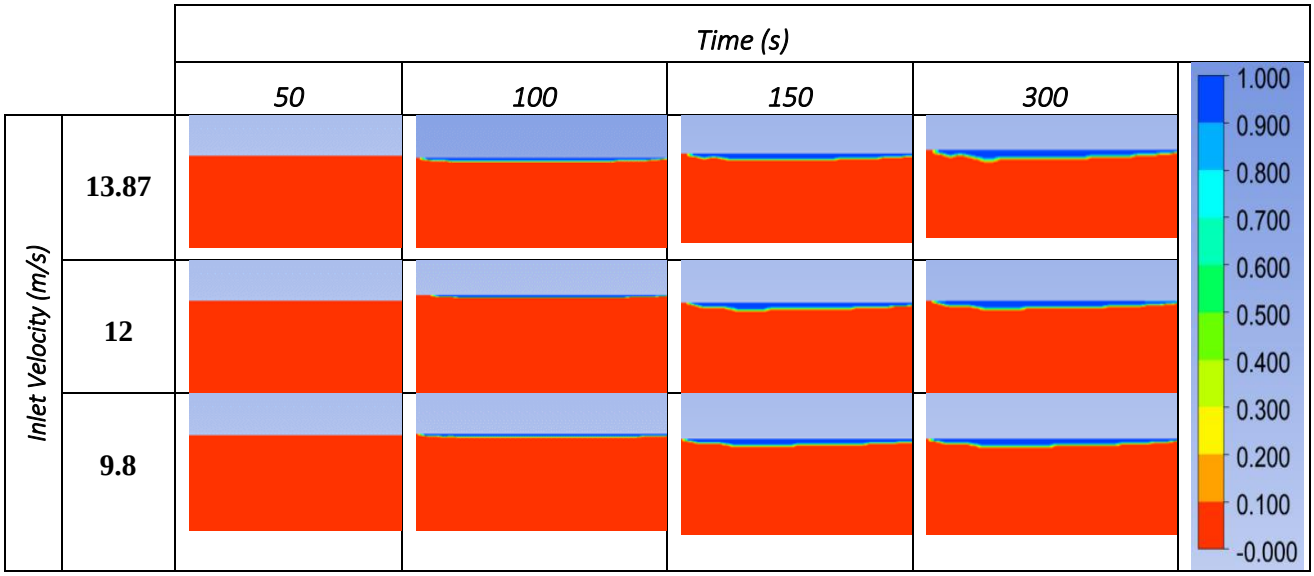

Figure 4.13: Clot contour plot comparing cases with different velocities. A scalar is tracking the clotted area changes from zero to one when the area has clotted.

4.2.11.2. Effects of Geometry Change on Clot Size

Figure 4.14 illustrates the changes to the clot size as the vein diameter changes. The larger the vein, the

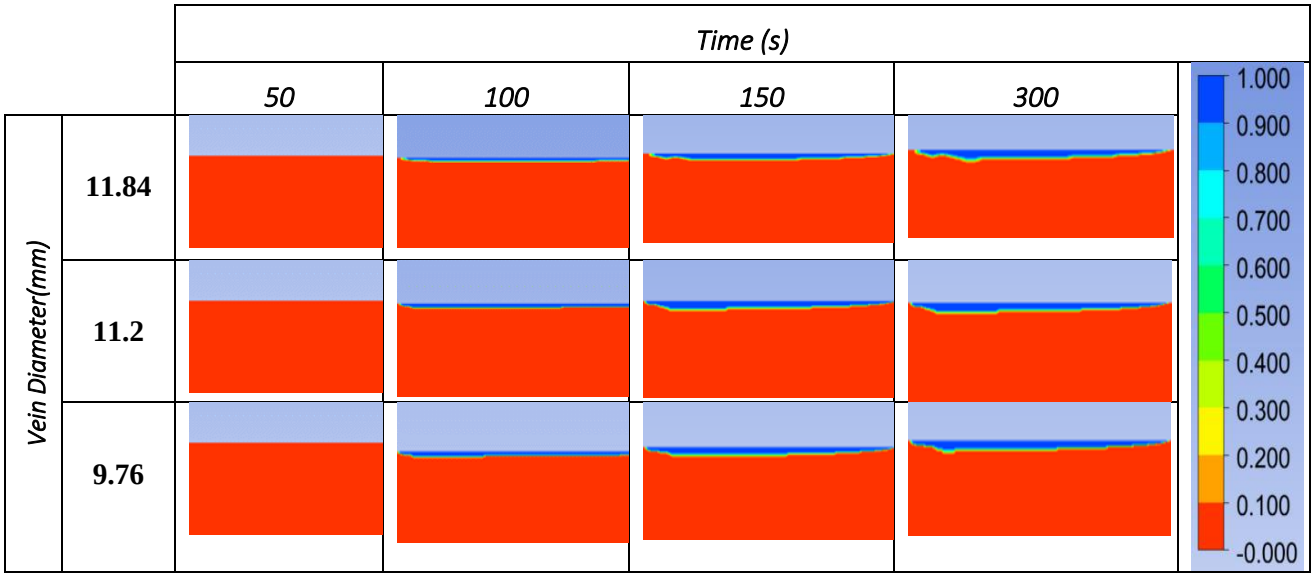

smaller the size of the clot. A 5.4% reduction in vein diameter led to a 3.3% increase in clot size, and an 18% decrease in vein diameter gave a 4.7% increase in clot size. The vein diameter does not affect the clot initiation time, with all three cases initiating clots at 75.5s. However, the clot becomes fully formed earliest in the largest vein. Figure 4.15 shows the clot formed for the different geometries.

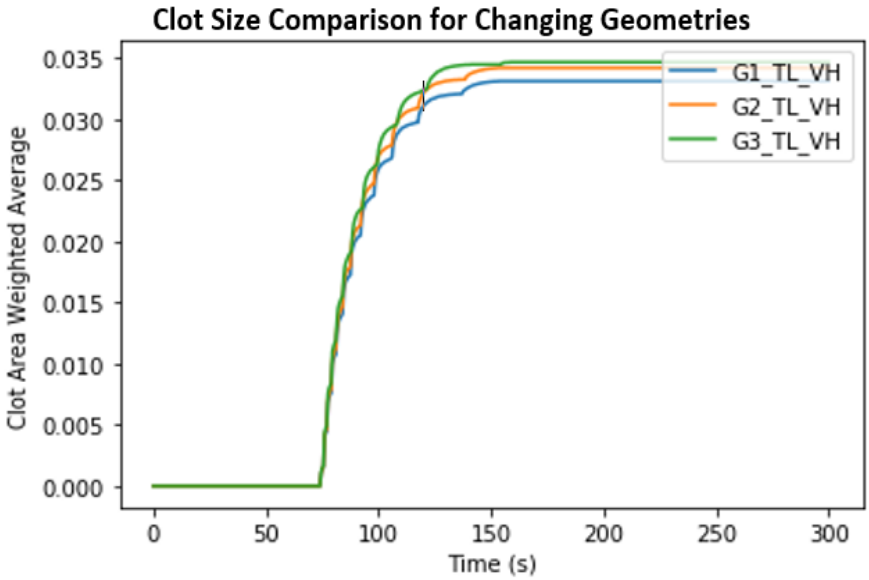

Figure 4.14: Graph comparing the size of the clot formed as geometry changes over 300s.

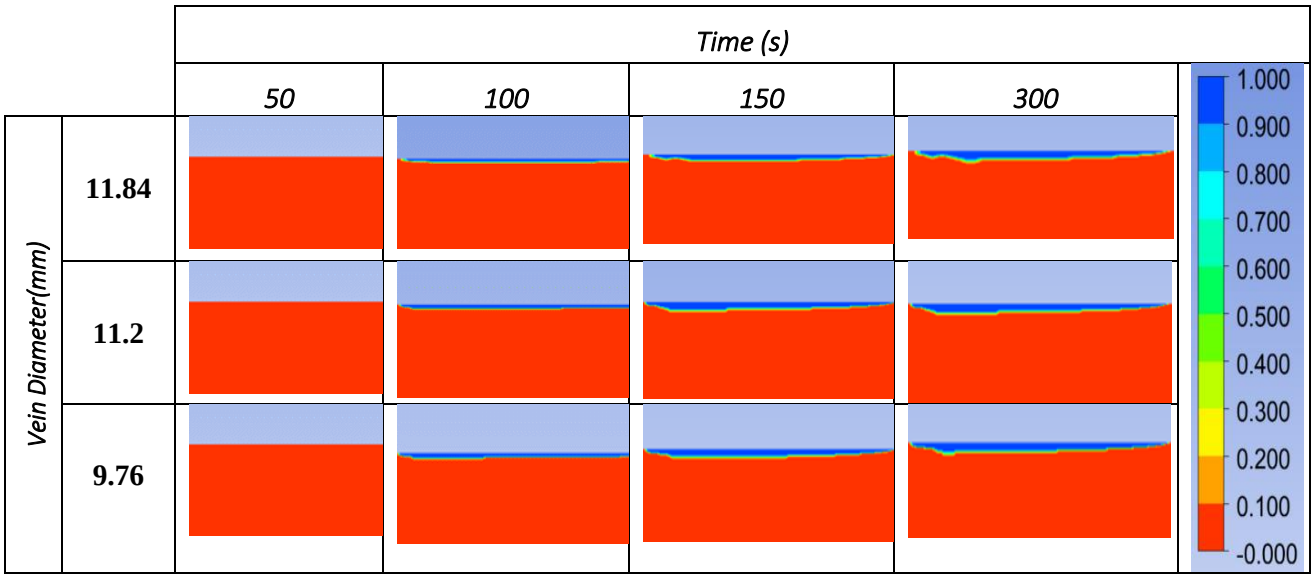

Figure 4.15: Clot contour plot comparing cases with different vein diameter. A scalar tracking the clotted area changes from zero to one when the area has clotted.

4.2.11.3. Effects of Peak Thrombin Concentration on Clot Size

Figure 4.16 illustrates the comparison between the clot sizes of three thrombin concentration levels. The case with the lower thrombin peak (G1_TL_VM) had an earlier clot initiation and reached its peak earlier. The lower the thrombin concentration peak, the earlier the clot initiates. The thrombin concentration peak seemed to have little effect on the propagation rate of the clot. Figure 4.17 shows the clot contour at different times of the cases. A 68nM increase in thrombin peak concentration led to an 11.5% increase in clot size, and a 150nM increase in thrombin peak concentration led to a 20% increase in clot size.

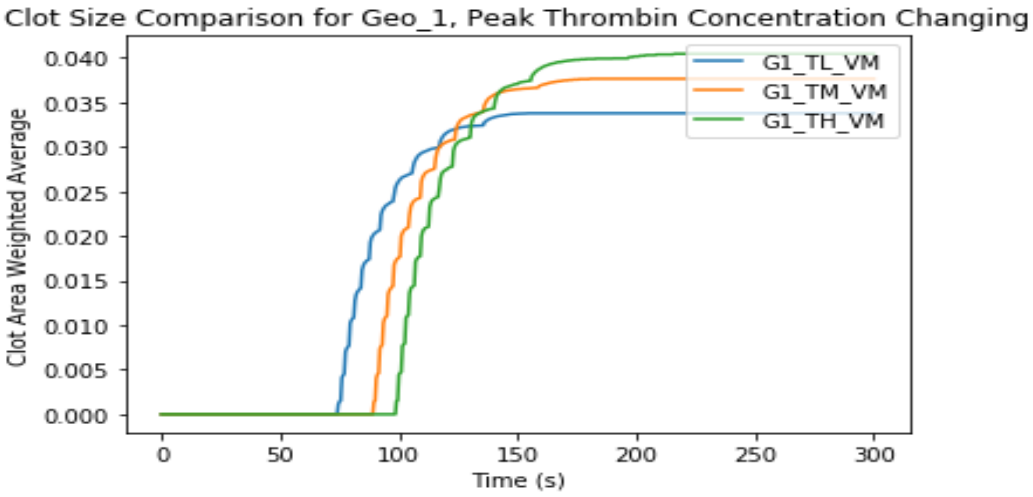

Figure 4.16: Graph comparing the size of clot formed as peak thrombin concentration changes over 300s.

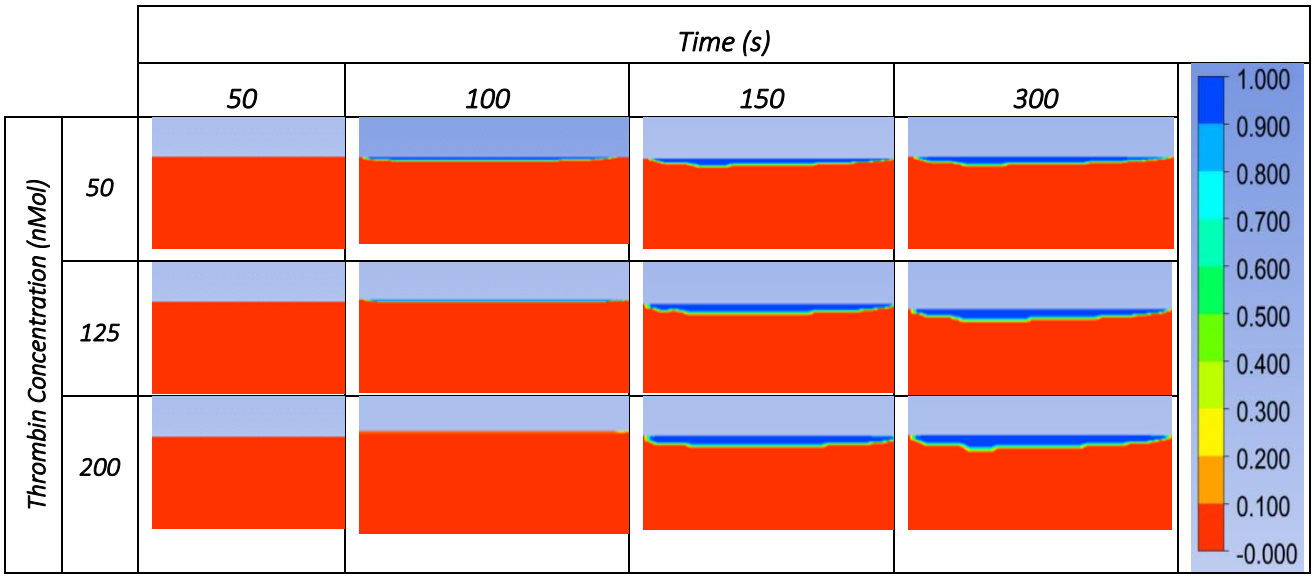

Figure 4.17: Clot contour plot comparing cases with different thrombin concentrations. A scalar tracking the clotted area changes from zero to one when the area has fully clotted.

4.2.12. Discussion

This study presents a model of clot growth in a two-dimensional geometry incorporating blood flow with biochemical reactions. The model was used to study the difference between using the flux and value boundary conditions to define thrombin's introduction into the flow. The model was also used to study the effect of changing parameters like velocity, vein diameter, and peak thrombin concentration on the clot's size. The resultant clot sizes and shapes were compared to other clots developed in the literature. There are not many fully thrombin-based reduced deep vein thrombosis models in the literature. However, some coagulation models were found, and their methodology was applied in developing this model. All the values used in this model were derived from literature. The thrombin generation profile was used, and a thrombin concentration threshold of 1nM was used to determine when the clot initiates [122].

Before commencing the study, steady and transient state grid independence tests were performed on the three geometries used. The geometries were grid independent at 30000 elements and a time step of 0.5s.

The parabolic velocity profile applied at the inlet continued throughout the length of the vein. The velocity gets obstructed by the clot as it grows and slightly shifts the position of the parabola's peak. The pressure in the vein decreases linearly from the inlet to the outlet. As the clot propagates, the pressure gradient contour's noticeable effect on the pressure can be seen. The thrombin diffusion was isotropic and was influenced by the flow.

The thrombin boundary condition investigation focused on setting up point probes that measure the concentration of thrombin at different distances away from the wall. The concentration of thrombin at point 0.05mm away from the wall when using the flux boundary condition was about 700 times the value when using the value. This is physiologically unrealistic. The thrombin generation function was then altered to reduce the concentration to a more realistic value to be able to apply the flux boundary condition as recommended by Neeves et al. [114]. As illustrated in Figure 4.5, thrombin in both value and flux cases diffuses up to 0.11mm away from the wall. This indicates that the diffusivity is not sensitive to the biochemical method of introduction into a flow.

An increase in the diameter resulted in a smaller sized clot, as illustrated in Figure 4.14. All three clots are initiated simultaneously as the geometry does not affect the concentration at the clot's core. The manner in which clots propagate was similar for all three cases. As seen in Figure 4.15, the diameter does affect the shape or length of the clot formed. In an idealised straight geometry, the effects of changes in the geometry size on the clot's initiation time are barely noticeable when compared to geometries with complex flow patterns, which are known to favour thrombosis [123]. However, as clot formation propagates, the clot forms a stenotic flow that causes a form of laminar jet action. This result in the regions close to the clot surface experiencing low shear which leads to an increase in clot size, as shown by Young et al. [124]. At constant velocity, the diameter determines how severe the jet action is; this explains the decrease in clot size with an increase in vein diameter seen in the result.

The size of the clot decreases as the velocity increases, as shown in Figure 4.12. The effect of the velocity on clot propagation depends on the rate at which thrombin is being transported away from the injury site off. The blood velocity might also be a key factor in how far from the inlet the clot will grow, as illustrated in Figure 4.13. Keeping the vein diameter constant and increasing the velocity also similarly affect the propagation of the clot as changing the diameter. The jet action is formed, and the clot increase in size. Although, in this case, there is an increase in shear on the surface of the clot to reduce the amount of thrombin that diffuses further, hence reducing the size of the clot [125].

The initiation of clot growth occurred earlier in the case with the lower thrombin concentration peak. This was expected as the thrombin generation curves show that keeping ETP constant and decrease the peak value, increases the thrombin generation time. The clot size increases as the peak thrombin

concentration increases, as illustrated in Figure 4.16. This concurs with work done by Wolberg et al. The group proved that high thrombin concentration produces larger, dense networks of branched fibrin fibres. However, the clot produced is susceptible to lysis [125], [126]. Although the model developed in this work does not give any information on the fibrin network, it successfully predicts the clot sizes based on the thrombin concentration. In all the cases, the clot fully covers the injury site within the first 300s.

The limitation of the model developed is the simplification of the processes involved with clot formation. The complex biochemical reactions involved in clot formation were reduced to the thrombin concentration, the pulsatile blood flow was reduced to a steady parabolic flow, and the clot was reduced to a lower porosity zone. These simplifications will slightly vary the clot produced by the model. The amount of variation caused by the simplification can be studied using more complicated models in the future. This will help understand the quantitative effects of these simplifications.

Further development on the parametric studies performed will be to study the effect of these parameters on the clot formed using a wider range of values. A pulsatile velocity at the inlet could also be implemented, and this would allow studying the clot formed under the varying velocity.

5. DEVELOPMENT OF DEEP VEIN THROMBOSIS IN A THREE-DIMENSIONAL PATIENT-SPECIFIC GEOMETRY.

Creating patient-specific models has proven to be an important development for CFD, based on medical imaging. Dedicated diagnosis and treatments for an individual patient are enabled. The chapter improves on the model developed in the previous chapter and presents the developmental processes for a three-dimensional patient-specific deep vein thrombosis model. The model is then used to study the clot initiation and propagation under physical and biochemical factors.

5.1. Overview

The coagulation cascade is complex, containing about 30 different species interacting with one another. Attempts have been made to model the complete mechanism with all the known reactions leading to clot formation in order to study the initiation and propagation of a clot [127]. It was discovered that thrombin plays a crucial role in the process [128], [129]. Virchow's triad described in the literature review proposed that for clot formation to occur, there must be at least one or a combination of stasis in the vessel, hypercoagulability, and injury to the vessel wall. The formation of thrombus is mainly reliant on two mutually linked processes; platelet interaction and the activation of the coagulation pathways[127].

After damage to the vessel wall, the platelet adheres to the vascular lesion, forming a cellular layer. Morphological changes occur in the platelets and stick together and form cell aggregates. Models were developed to describe the intrinsic, extrinsic and common pathways of the coagulation cascade [67], [75], [110]. These models were then simplified into three major stages by Wu et al, [130]. Prothrombin is created in response to the damage of the vessel wall, prothrombin is then activated and converted to thrombin, finally, thrombin reacts with fibrinogen to form fibrin. The polymerised fibrin traps the platelets and form a clot over the wound site.

The valves in the deep veins play an important role in the clot formation process. A dislodged embolus can get trapped between the values and obstruct blood flow in the vessel. The opening and closing of the values make the area around the valve sinus susceptible to clot formation as there is bound to be stasis it the area. Ibrahim et al. developed a model of DVT caused by valve malfunctions in the popliteal vein. The valve opening was varied, and the size of the static zone and vorticity was investigated [97]. Bends and curves present in complex geometries can also cause stasis in some area, supporting clot initiation[93]. Brass et al, claimed that the main factors affecting the clot initiation are the flow parameters such as velocity, wall shear rate and wall shear stress, in addition to the blood biochemistry.

A different thrombosis model was developed by Xu et al to study thromboembolism. A two-dimensional model similar to that developed in the previous chapter was applied. The clot stability was investigated under different flow conditions. The clot was modelled to be in two sections, the more

dense core and the less dense shell [99]. Most DVT models in literature focus solely on the flow and stasis in the vein. Fortuny et al developed DVT model in a patient-specific vein geometry, with a fully developed clot. The model was used to study the effect of the clot on the wall shear stress and how the wall shear stress responds to anticoagulants [100]. Few patient-specific models take the blood biochemistry as well as the flow and valve action into account.

Considering all the flow and biochemical factors involved in clot formation is complicated when developing a DVT model. The conditions that are likely to lead to realistic platelet response such as the chemical reactions in the coagulation cascade are focused on. The model described in this chapter describes the development of a three-dimensional DVT model. The model will be an improvement to the model developed in the previous chapter. The model account for steady and pulsatile blood flow in the vein, biochemical reactions between thrombin and fibrinogen involved in the formation of fibrin, porosity effect of a clot, and the valve activities. The formation is fibrin mesh is modelled based on the coagulation cascade simplification done by Wu et al, [130]. The clot core and shell are also modelled to simulate the possibility of embolism.

The final aim of the project is to develop a realistic model which is applied in a patient-specific geometry. The model is applied on a patient-specific geometry and the clot formed is compared to the clot formed in a physiological condition. All the data used in this study were derived from literature.

5.2. Idealized 3-Dimensional Geometry Model Development

The modelling process used in this study is the same as that used in the previous chapter. The image and data acquisition was the same for velocity, pressure, vein geometry and thrombin concentration.

5.2.1. Vein Geometry

The complex geometry of the vein derived from literature was simplified into a cylinder shown in Figure 5.1(a). The length of the idealised vein was determined by taking the average distance between two venous valves. The geometry provides a model that can be used to predict clot initiation and propagation. The parameters used in the idealised geometry are then translated into a patient-specific geometry which is presented later in this study. Flow enters at the inlet; thrombin is generated at the injury zone and blood exits at the outlet. Two geometries are initially used with the injury zone covering 30% of the circumference in the first and 100% in the second. The injury zone is 50% of the length of the vein in both cases. The diameter and length of the vein, 9.76mm and 60mm respectively were derived from the previous chapter.

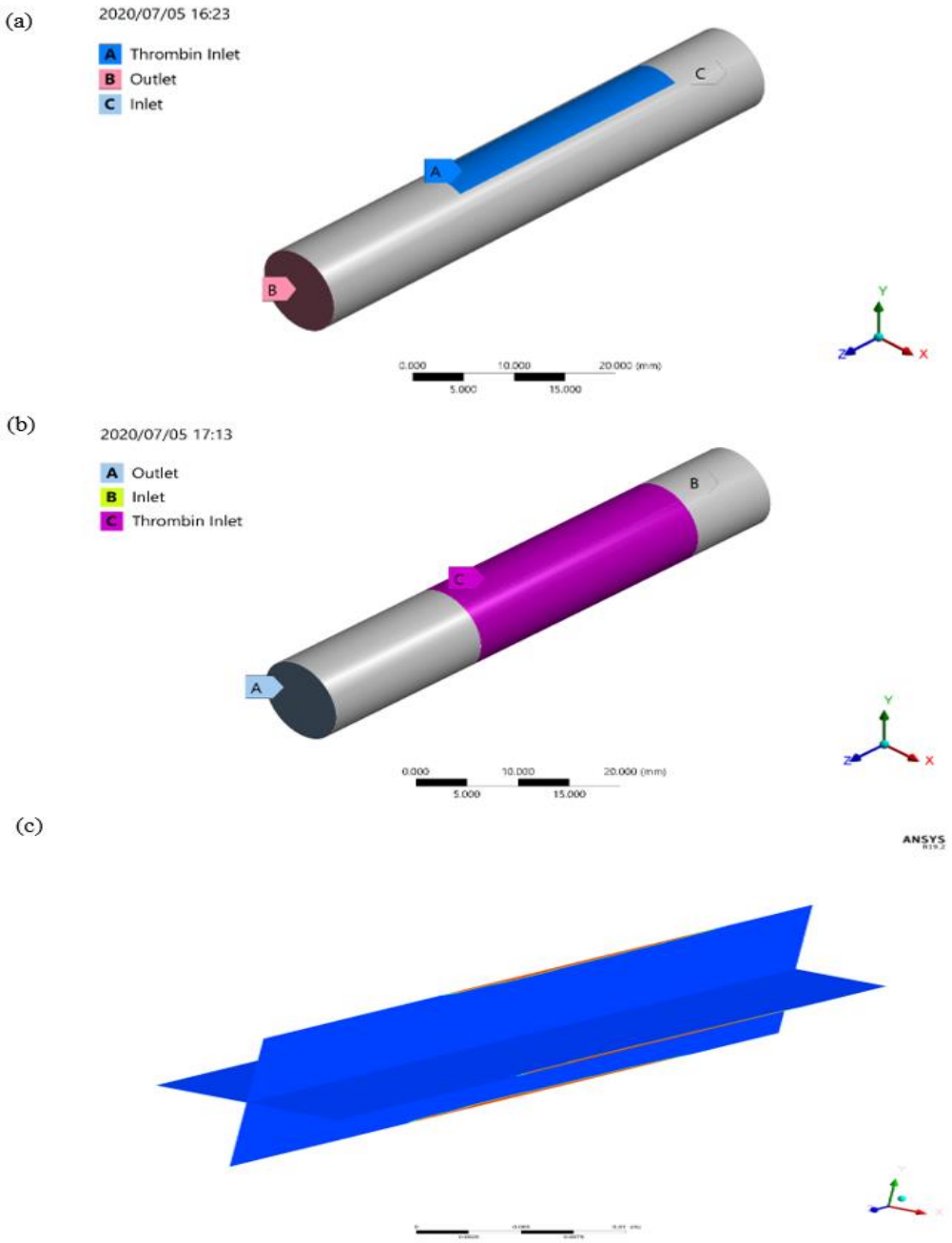

Figure 5.1: Three-dimensional geometry with injury zone covering (a)30% (b) 100% of the circumference. (c) Contour showing clot formed on the x-z and y-z plane.

A basic investigation of the injury zone was carried out to verify the initial assumption made in the previous chapter that what happens on the midplane is the same across the circumference. The model developed in the previous chapter was applied to the two three-dimensional geometries developed shown in Figure 5.1 (a) and (b). Figure 5.1 (c) shows that the clot formed on any midplane of the vein is the same. To reduce the computational expense and complexity of the model, the 30% injury zone geometry (Figure 5.1 (a)) is used for this study.

5.2.2. Mesh Independence Test

A mesh independence study was conducted on the geometry. The blood flow and thrombin concentration were monitored. The velocity at the outlet was studied as in the previous chapter to ensure that the flow was grid independent. The thrombin concentration at point probes away from the injury site was determined and compared to ensure mesh independence of the biochemical species. Three mesh refinements were used, with 250000, 5000000 and 1000000 elements. Twenty inflation layers were applied to make the cell size around the wall less than those close to the vein centre for increases accuracy of biochemical transport in that area.

Table 8: Grid independence test result for steady and transient state.

Steady State Mesh Independence Result					
	No of Elements	Element Size (mm)	Average Outlet Velocity (m/s)	Maximum Velocity (m/s)	% Error Compared to Next Finer Mesh
Mesh 1	250,000	0.7	0.0907	0.1340	1.68
Mesh 2	500,000	0.52	0.0914	0.1363	0.23
Mesh 3	1,000,000	0.404	0.0916	0.1366	0
Mesh 4	1,500,000	0.3	-	-	-

Transient State Mesh Independence Result					
	Courant Number	Corresponding Time step size (s)	Peak Thrombin Concentration (nMol)	Average Thrombin Concentration (nMol)	% Error
Mesh 1	> 1	0.0005	51.4	10.9	12.1
Mesh 2	> 1	0.0003	65.4	12.4	40.0
Mesh 3	> 1	0.00025	108.5	20.7	1
Mesh 4	> 1	0.00025	109.0	20.9	-

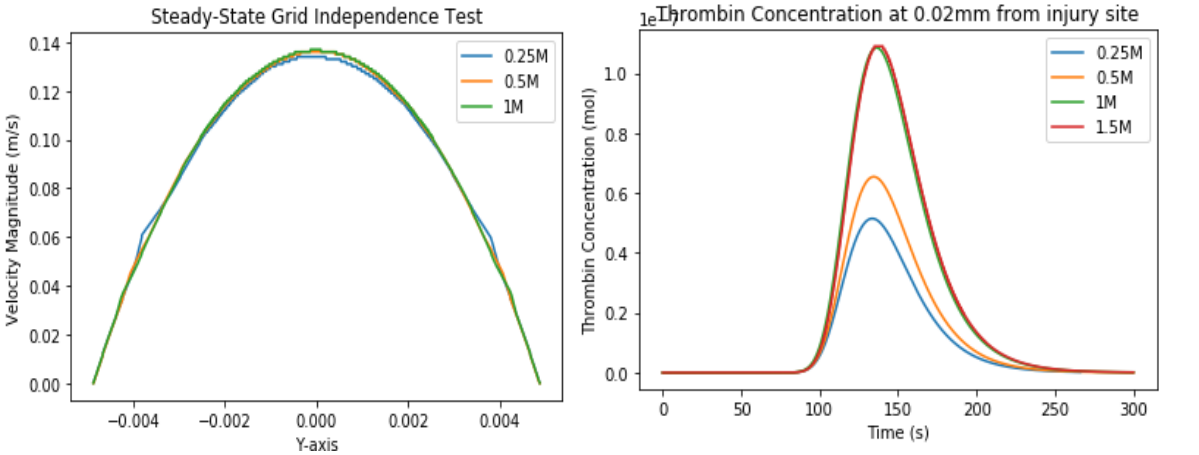

Figure 5.2: (a) Parabolic velocities at the outlet for different mesh sizes. (b)Thrombin concentration at point probe 0.02mm away from the injury site for the different mesh sizes.

Applying a 1% error limit, Table 8 and Figure 5.2 shows that the flow becomes grid independent at 500000 elements, and the biochemical transport is grid independent at 1,000,000 elements. These values are used for the rest of the simulations in this chapter.

5.2.3. Biochemistry Setup

Chapter 4 discussed that it is computationally expensive to account for all the reactions pathways involved in coagulation. When necessary, simplicity is key when developing a patient-specific model as it is easier to match biochemical profiles for fewer number of parameters on a per patient basis. The model considers the reaction between thrombin and fibrinogen, forming fibrin. Thrombin is generated at the injury site as a flux and fibrinogen is present in the blood flowing in from the geometry's inlet. The concentration of fibrin increases to a threshold value of 1000 nMol where the clot begins to form [94]. The density of the clot formed is based on the concentration of fibrin. This allows the distinction between the clot core and shell. The reaction was described using the Michaelis-Menten equation.

$$Thrombin(IIa) + Fibrinogen\ (I) \Rightarrow Fibrin\ (Ia) \qquad \textbf{Eq. 5.1}$$

$$\frac{d[Ia]}{dt} = \frac{k_{cat}[IIa][I]}{K_m + [I]} \qquad \textbf{Eq. 5.2}$$

Where k_{cat} is the catalytic rate constant and, K_m is the Michaelis constant.

Table 9 below describes the values of the properties of the biochemical species and reaction parameters involved in clot formation in this model. A positive source term describes the formation of fibrin, and a negative source term describes the sink or consumption of fibrinogen. To ensure that fibrin formation does not exceed physiological values, the fibrin concentration is limited to a maximum value of 10000nMol and the fibrinogen concentration to a minimum value of 0.1 nMol. Refer to the Appendix for UDFs used to describe the biochemical reactions.

Table 9: Biochemical properties and values used for the reaction kinetics [94].

Biochemical properties		
Biochemicals	**Initial Value (nMol)**	**Diffusion Coefficient 10^{-7} (cm^2/s)**
Thrombin (IIa)	0	6.47
Fibrinogen (I)	7000	3.10
Fibrin (Ia)	0	2.47
Reaction Kinetics parameters		
Parameter	**Values**	**Unit**
k_{cat}	3540	min^{-1}
K_m	3160	nMol

5.2.4. Pulsatile Velocity

To orient the model towards patient-specificity, physiological pulsatile flow is implemented at the inlet. To enable accurate prediction of clot formation, the blood velocity in the target vessel of the patient is obtained. For the development of the model, cases, where measurements of the venous velocity are measure, were examined. To account for pulsatile flow in this model, a venous doppler sonography of the lower extremities was performed on a healthy 27-year-old woman by Selis and Kadakia [131]. It is understood that there is high variability in the appearance of the normal venous waveform between patients. This is due to differences in rate and depth of respiration, right heart function, intravascular volume and valve activities [131]. There are cases wherein the waveform lacked pulsatility and further evaluation was done by performing additional imaging for compression or obstruction.

The sonography, shown in Figure 5.3 depicts the pulsatile blood flow in the right central femoral vein (CFV). The plateau of the profile during each cycle indicates the activity of the venous valves.

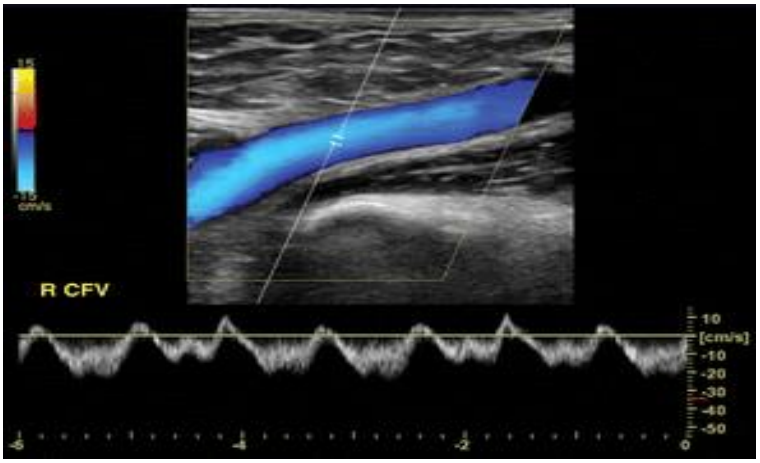

Figure 5.3: Venous waveform obtained from a healthy 27-year-old woman showing cardiac pulsatility and valve activity in the right CFV.

The velocity profile required digitizing to allow a generated plot to be applied at the inlet. The digitized profile provides the velocity at any time *t*. The velocity profile in Figure 5.3 was exported as a .jpeg file to an open-source plot digitizer package [132]. To digitize the data, the axis was set and the maximum values for time and velocity were determined. Points were placed on the velocity line as shown in Figure 5.3. The plot digitizer gives the coordinates of these points (time, velocity) in a .csv format based on their position relative to the set axis.

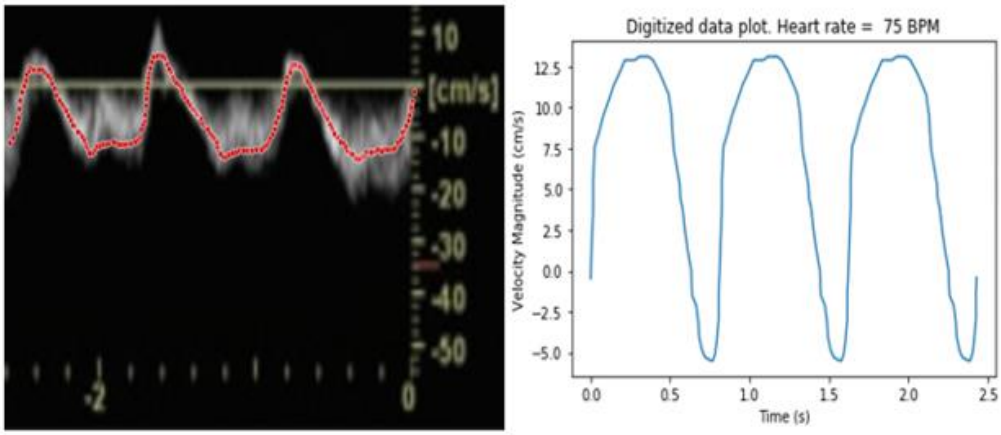

Figure 5.4: Digitization of velocity data from sonography. Red dots manually placed and generated .csv file used to create plot on right.

An equation representing the plot in Figure 5.4 was then generated in Microsoft Excel using the curve fitting method. A Fourier transform fit was chosen and the least-squares method was applied. The sum of the least-squares of a Fourier transform was reduced to the minimum by varying the amplitude, phase and frequency. The generate Fourier transform is represented by Eq. and illustrated in Figure 5.5. There was a 1.1% average error between the digitized and Fourier transform velocity.

$$v_P(t) = 0.083\sin(7.8t + 5.3) + 0.022\sin(15.6t + 5.8) + 0.01\sin(7.8t + 5.33) + 0.2 \qquad \textbf{Eq. 5.3.}$$

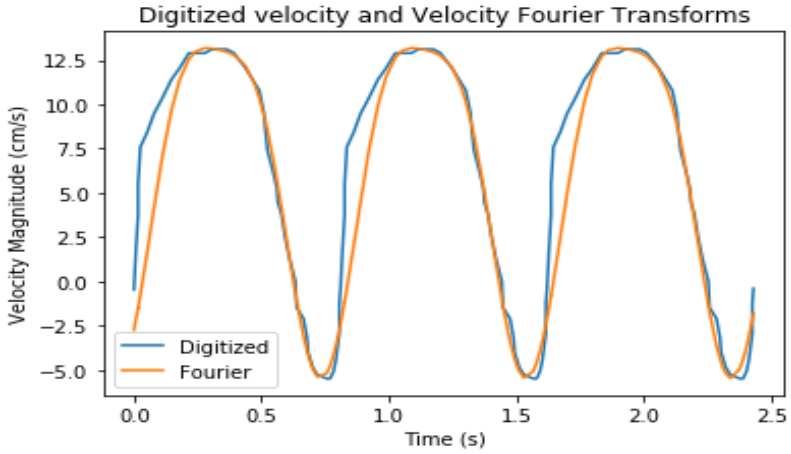

Figure 5.5: Comparing the generated Fourier Transform to the digitized velocity plot.

To achieve fully developed parabolic flow, Eq. 5.3. produced the value used for the peak velocity values at any time *t*. Figure 5.6 shows the plot of the velocity profile at the vein inlet for one heartbeat cycle and Figure 5.7 shows the velocity contour as time changes during the cycle. Note the reversed flow at times 0.0s, 0.7s, and 0.8s as a result of the venous valve activity and gravity.

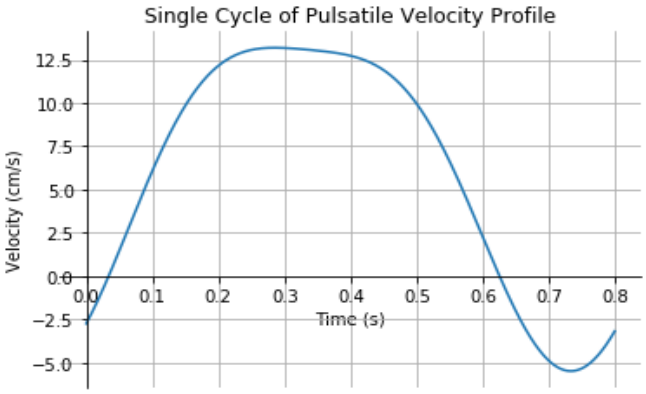

Figure 5.6: Pulsatile velocity profile for a single heartbeat.

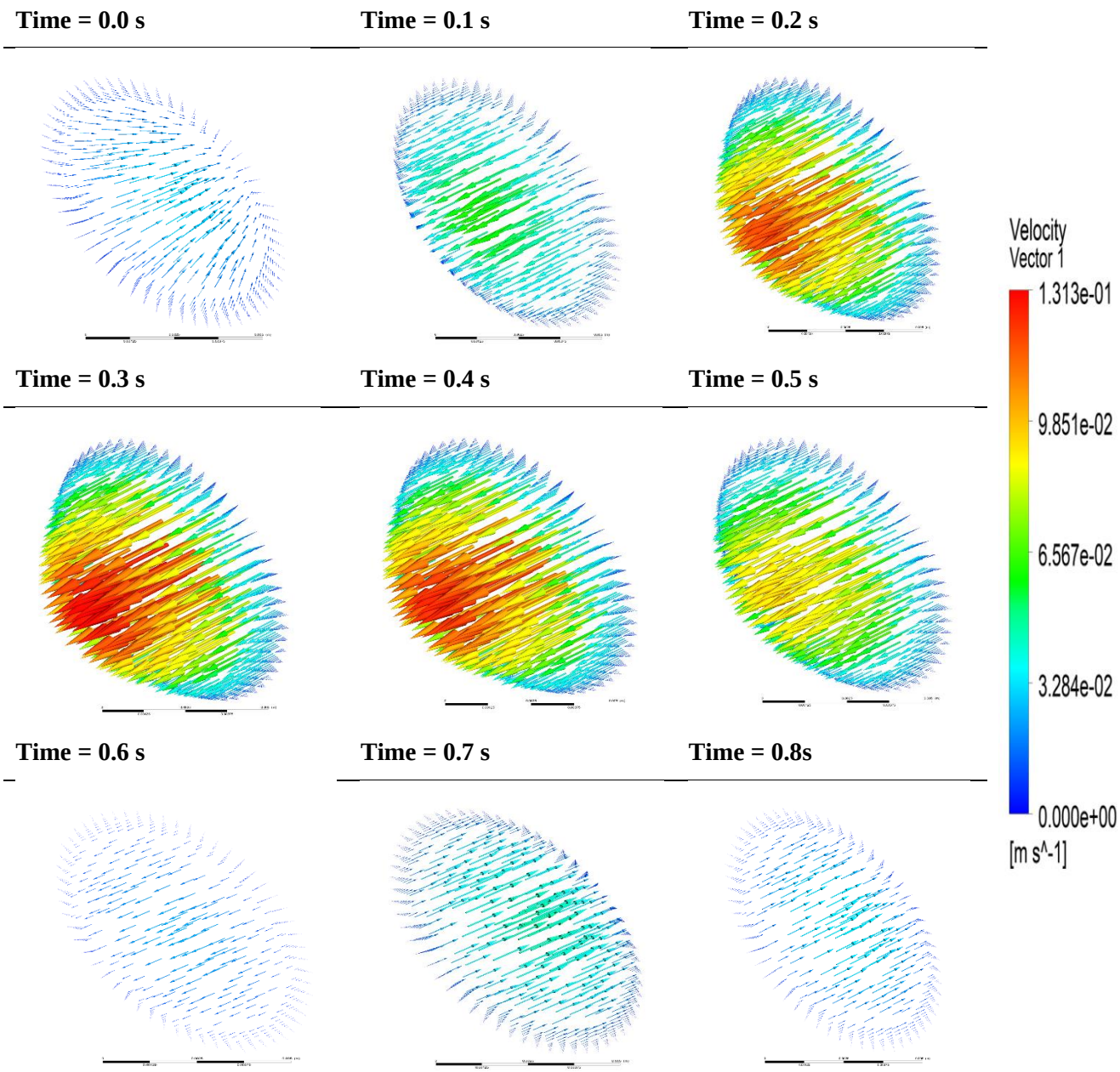

Figure 5.7:Velocity vector at the inlet at different times for one heartbeat cycle.

5.2.5. Valve Activity

The valve activity in the veins plays a crucial part in clot formation. The movement of valves creates distortions and stagnation zones in flow. For accurate prediction of clot formation, the effects of venous valves need to be included in the model. There are different approaches to modelling valves found in literature, as discussed in the literature review chapter. This model applies a variation of the model presented by Hajati et al, [105] which was based on a Doppler Ultrasound image of a 35-year-old person in a supine position. The model was developed to validate the flow velocity between the valve leaflets of the femoral vein. The vein walls are considered as a linear elastic material and the leaflet as a hyperelastic material. The inlet velocity was set as a sine function as a result of the opening and closing of the series of valves in the vein.

The model presented in this work does not consider the fluid-structure-interaction (FSI) between the valve wall and blood. The pulsatile velocity derived above is broken down into different stages of the valve activity as shown in Figure 5.8. For the model, the valve activity was achieved by varying the inlet diameter and hence the flow area. The flow area was directly proportional to the velocity magnitude. Where the maximum area is equivalent to the peak velocity. Figure 5.9 shows the comparison between the inlet radius and velocity magnitude at the vein inlet for a single heartbeat cycle. An interesting occurrence to notice in this proposed valve representation is that the valve leaflet open and closes two time in one heartbeat. This is as to the patient's valve malfunction, allowing blood flow in the reverse direction once every cycle.

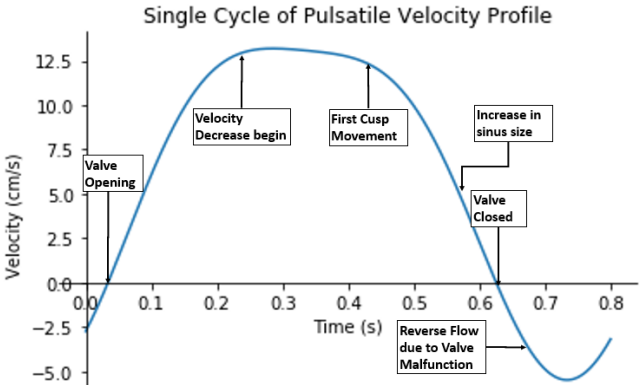

Figure 5.8: Time relation between pulsatile blood flow and valve cycle.

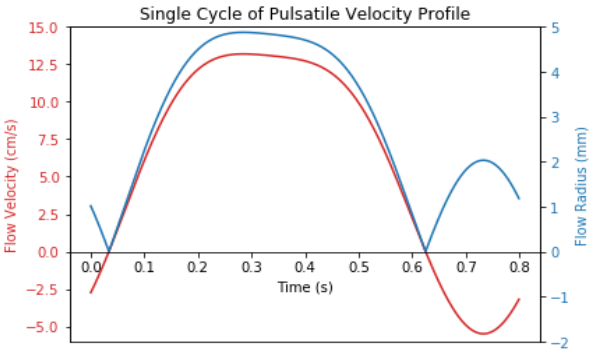

Figure 5.9: Flow velocity compared with flow radius during a single heartbeat cycle.

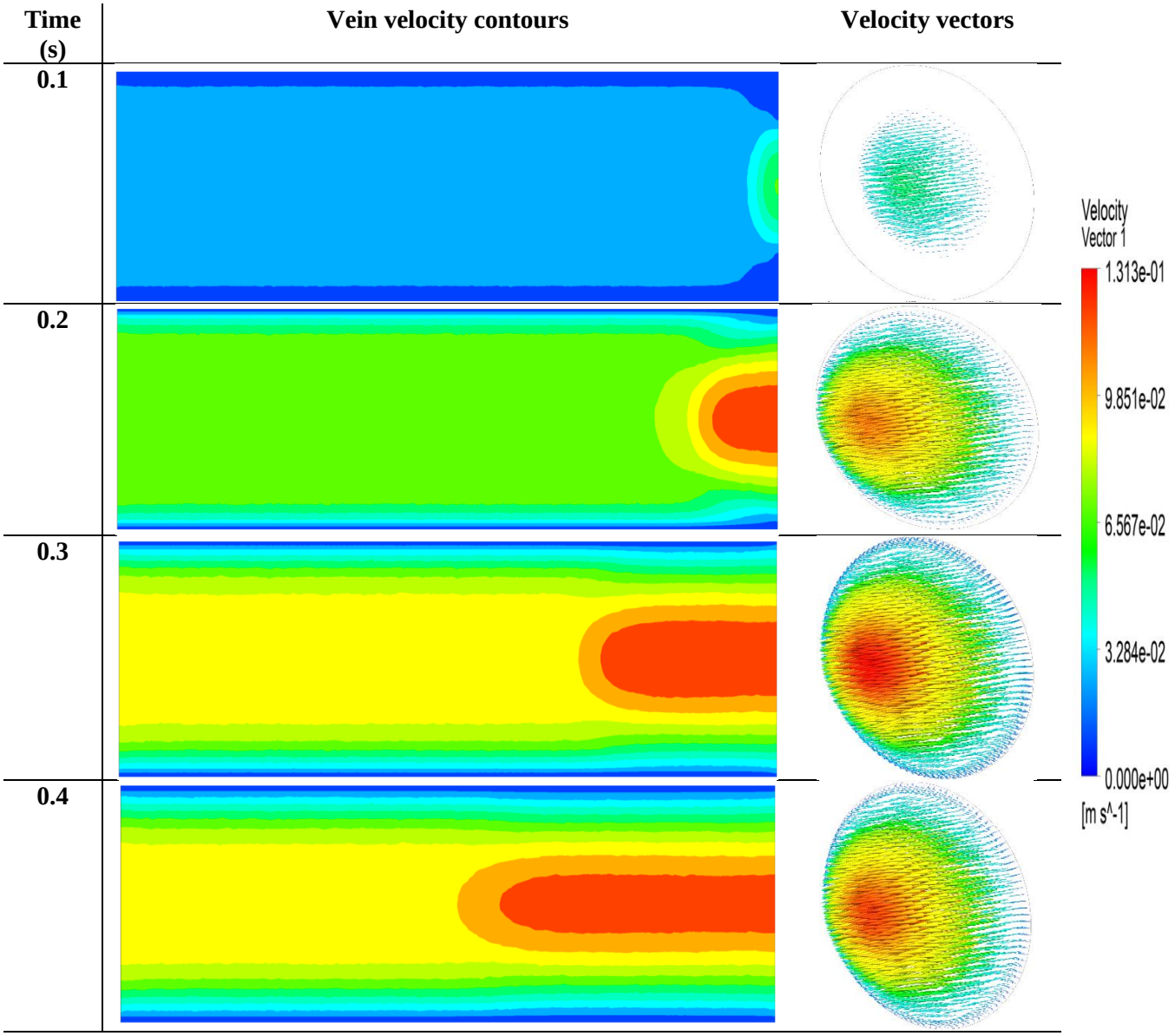

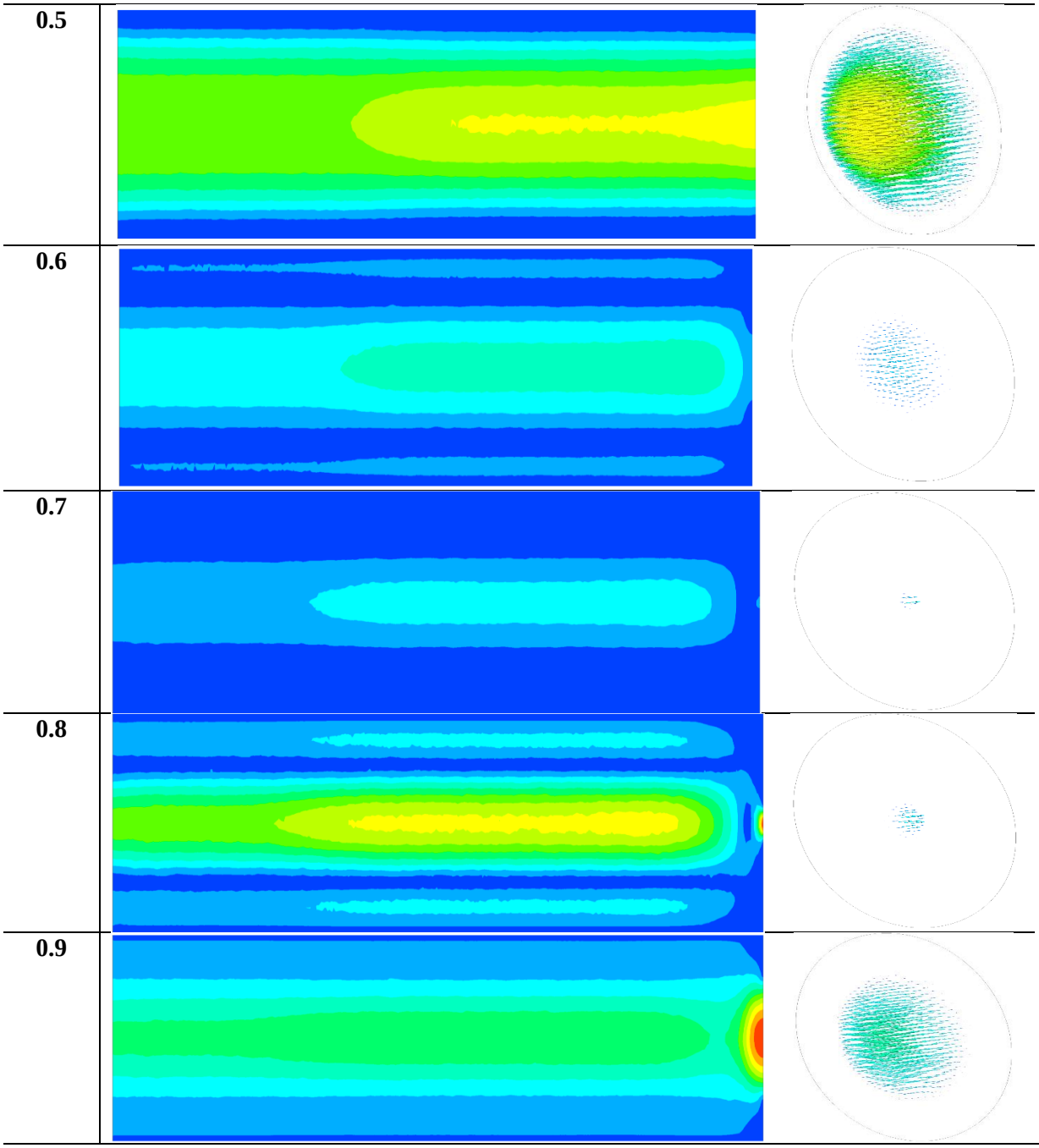

Figure 5.10: Vein velocity contours and vectors through one heartbeat cycle.

Figure 5.10 shows the velocity contour and vector at inlet through one heartbeat cycle. The flow area at the inlet changes and note reversed flow at times 0.7 and 0.8s.

5.2.6. Numerical Solving Parameters

To examine the initiation and propagation of the clot using the model, various stages of model development were studied. Table 10 below indicates these stages and the simulations carried out in this work.

Table 11: Simulations carried out to study the clot initiation and propagation as the complexity of the model increases.

Name	Flow Properties	Biochemical properties

Model_1	Parabolic blood flow	Clot Formation (Using Thrombin Concentration only)
Model_2	Pulsatile Parabolic blood flow	Clot Formation (Using Thrombin Concentration only)
Model_3	Parabolic Pulsatile blood flow Valve activities	Clot Formation (Using Thrombin Concentration only)
Model_4	Parabolic blood flow	Clot Formation (Fibrin formation from thrombin and fibrinogen)
Model_5	Parabolic Pulsatile blood flow	Clot Formation (Fibrin formation from thrombin and fibrinogen)
Model_6	Parabolic Pulsatile blood flow Valve activities	Clot Formation (Fibrin formation from thrombin and fibrinogen)
Model_7	Parabolic Pulsatile blood flow Valve activities Patient-Specific Geometry	Clot Formation (Fibrin formation from thrombin and fibrinogen)

5.3. Idealized 3-Dimensional Geometry Models Results

The results presented in this chapter illustrate clot formation in an idealized 3-D femoral vein model considering the flow and biochemical factors. The chapter explores clot formation with the increasing complexity of the model. Using Model_1, the properties that are similar in the initialization and propagation of clot in all the models are initially discussed. The differences in initialization and propagation are then discussed. The simulations were are designed to operate until the clots are fully developed. The results are discussed quantitatively in the terms of the size of the clots formed and qualitatively in terms of the shape and nature of the clot formed.

5.3.1. Pre-Clot Formation

For all models, the velocity and pressure in the vein pre-clot formation remained as set. Parabolic steady or pulsatile velocity was maintained in the vein and the pressure reduced from inlet to 0Pa at the outlet as shown in Figure 5.11(a) and (b). For the models with pulsatile velocity, a more complicated pressure pattern is noticed where the pressure rises and falls to correspond with the inlet velocity. Thrombin concentration is a major factor in clot formation. In conjunction with flow washing thrombin off, the low diffusivity value of thrombin prevents it from flowing downstream. Figure 5.11(c) indicates how far away from the wall thrombin diffused and Figure 5.11(d) shows the area of the vein with thrombin present at t = 70s. Little thrombin gets carried towards the outlet. This did not change in cases with pulsatile velocity. The strain rate was maximum at the walls and minimum at the centre of the vein. At this stage, the strain rate value follows a similar pattern as the velocity, the value remains constant for steady flow and varying accordingly with the corresponding velocity for pulsatile flow.

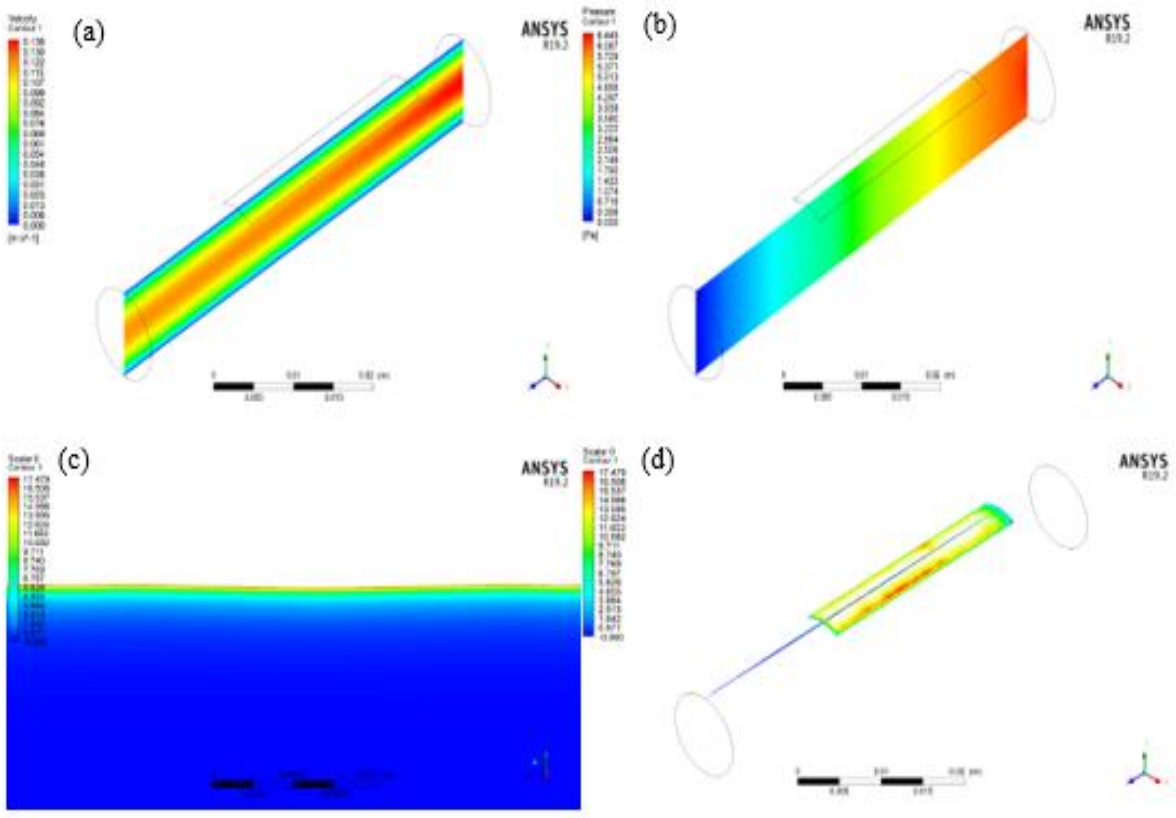

Figure 5.11: Contours of (a) Velocity (b) Pressure (c) Thrombin showing effects of low diffusivity (d) Thrombin showing the effect of flow on thrombin concentration at 75 secs.

Models_1,2,3 and Models_4,5,6 are compared with each other. Figure 5.12 illustrates the maximum strain rate value in the vein before the clot forms. Model_1 has a spike in strain rate at the start of the simulation, due to fluid entering the geometry. This spike immediately levels out in the next three timesteps to become stable at 132 s^{-1}. As explained previously, the maximum strain rate value in Model_2 and Model_3 is pulsatile, however, the value was much higher in Model_3. This is due to the value activity changing the velocity magnitude and the radius of flow simultaneously.

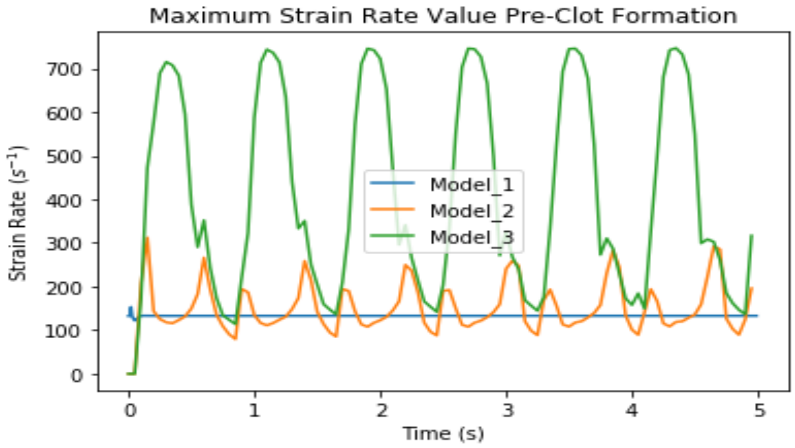

Figure 5.12: Maximum strain rate value for the first 5s.

5.3.2. Clot Initiation and Propagation

For clot to initiate, a threshold thrombin concentration and strain rate magnitude is applied. Clot formation initiates when thrombin concentration exceeds 10 nMol and the strain rate is below 132 s^{-1} [122], [133]. For all cases, the clot initiation disrupts the velocity field by reducing the velocity in the clotted area, causing reduction in strain rate in the clotted area and an increase on the surface of the clot. The clot begins to form around the end of the injury zone towards the outlet where the concentration is highest and propagates towards to inlet over time. The initiation times and manner of propagation varies between models.

Figure 5.13 illustrates the effects of improving the complexity of the model on the initiation and propagation of clot. It is important to note that all models were simulated in the same geometry and the same meshing method and element size were applied as per the grid independence study. Model_1 is the first and simplest model developed. The model considers clot formation under a steady parabolic flow. Clot initiation occurs at a threshold thrombin concentration and strain rate. Model_1 first produced clot at t = 89.1s. The clot then propagates at a steady rate until t = 143.16s, where the rate of propagation begins to slow down. This also coincides with the thrombin peak time or time to peak (TTP). The propagation continues until the clot reaches its peak at t = 180.32s.

Model_2 advanced on the flow properties of the previous model by applying pulsatile parabolic flow at the inlet. Clot initiated at t = 88.76s. An erratic clot propagation was noticed in these models where the propagation rate goes through a rise and fall cycle such that a fall takes the same amount of time as the preceding rise. This pattern continues until t = 147.65s when the rate continues to fall until the clot reaches its peak size at t = 231s. Model_3 also has a pulsatile velocity inlet; however, the flow is made to simulate the valve activity. Clot initiated at t = 88.8s and the erratic clot propagation noticed in Model_2 was also noticed. This pattern continues until t = 154.04s where the rate continues to fall until the clot reaches its peak size at t = 235s.

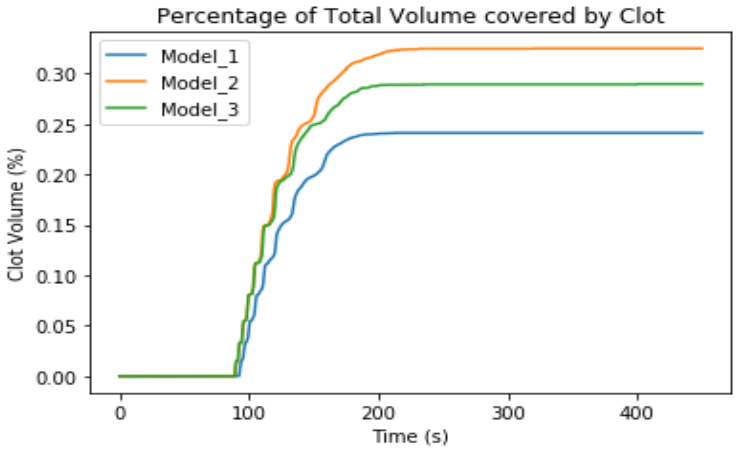

Figure 5.13: Comparison of the percentage of total volume covered by the clots in Model_1,2 and 3.

Thrombin concentration being the clot formation major factor in these models needs to be studied. The set peak thrombin concentration was 200nMol. Figure 5.14 illustrates the maximum thrombin concentration in the veins as time changes. Model_2 had a peak value of 220.76nMol at t = 145.1s and Model_3 followed the same trend with a peak value of 222.84nMol at t = 144.7s. Model_1 had peak value (220.3nMol) at t = 143.16s.

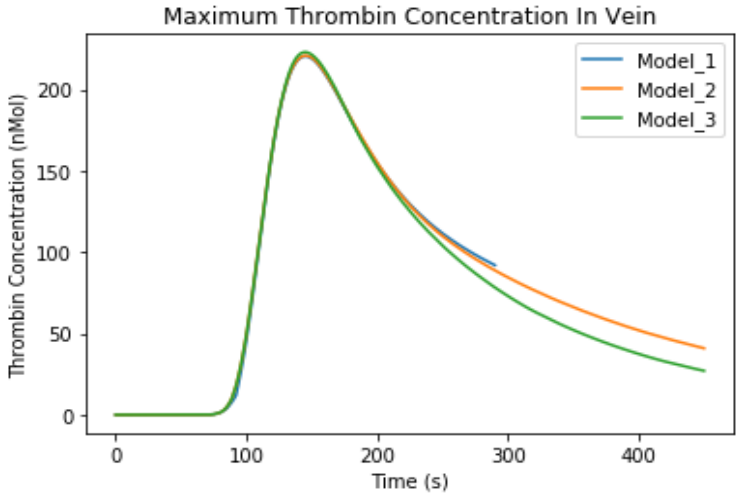

Figure 5.14: Comparison of maximum thrombin concentration in the vein. Model_1 ends at t = 300s to reduce computational cost as the clot is fully formed at this point.

Figure 5.15 illustrates the maximum strain rate in the vein during clot initiation. Strain rate in Model_1 gradually increases as the clot head grows towards the inlet. The value reaches a peak value of 142.7 s^{-1} and remains constant for the rest of the simulation. Model_2 also experienced an increase in maximum strain rate after clot initiated, however, no significant increase was noticed in Model_3.

The sizes of the clots formed are illustrated in Figure 5.13. Model_1 had the largest clot, with the clot volume covering 0.364% of the total vein volume. Figure 5.16 and Figure 5.17 shows the changes in clot size in Model_1, from clot initiation to when the clot is fully developed. Clots in Model_2 and Model_3 covered 0.325% and 0.290% of the total volume respectively. Model_1 forms a smooth-surfaced clot with a higher clot depth closer to the outlet. Clots formed in Model_2 and Model_3 have rough surfaces and the clot depth is almost even throughout the injury zone. Also, the clot in Model_1 did not propagate past the injury zone towards the inlet; However, such occurrence was noticed in Model_2 and Model_3.

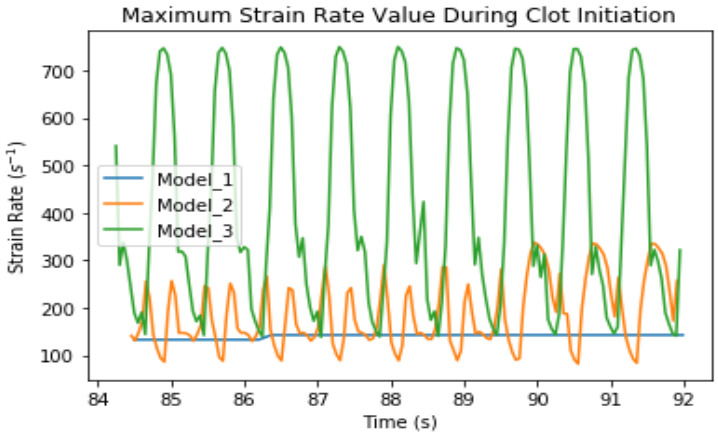

Figure 5.15: Maximum strain rate value before and after clot initiation.

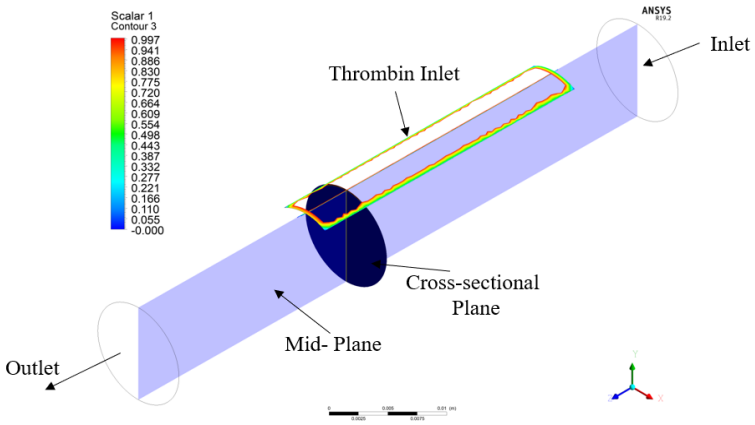

Figure 5.16:Outline of Vein showing planes and lines used for results analysis.

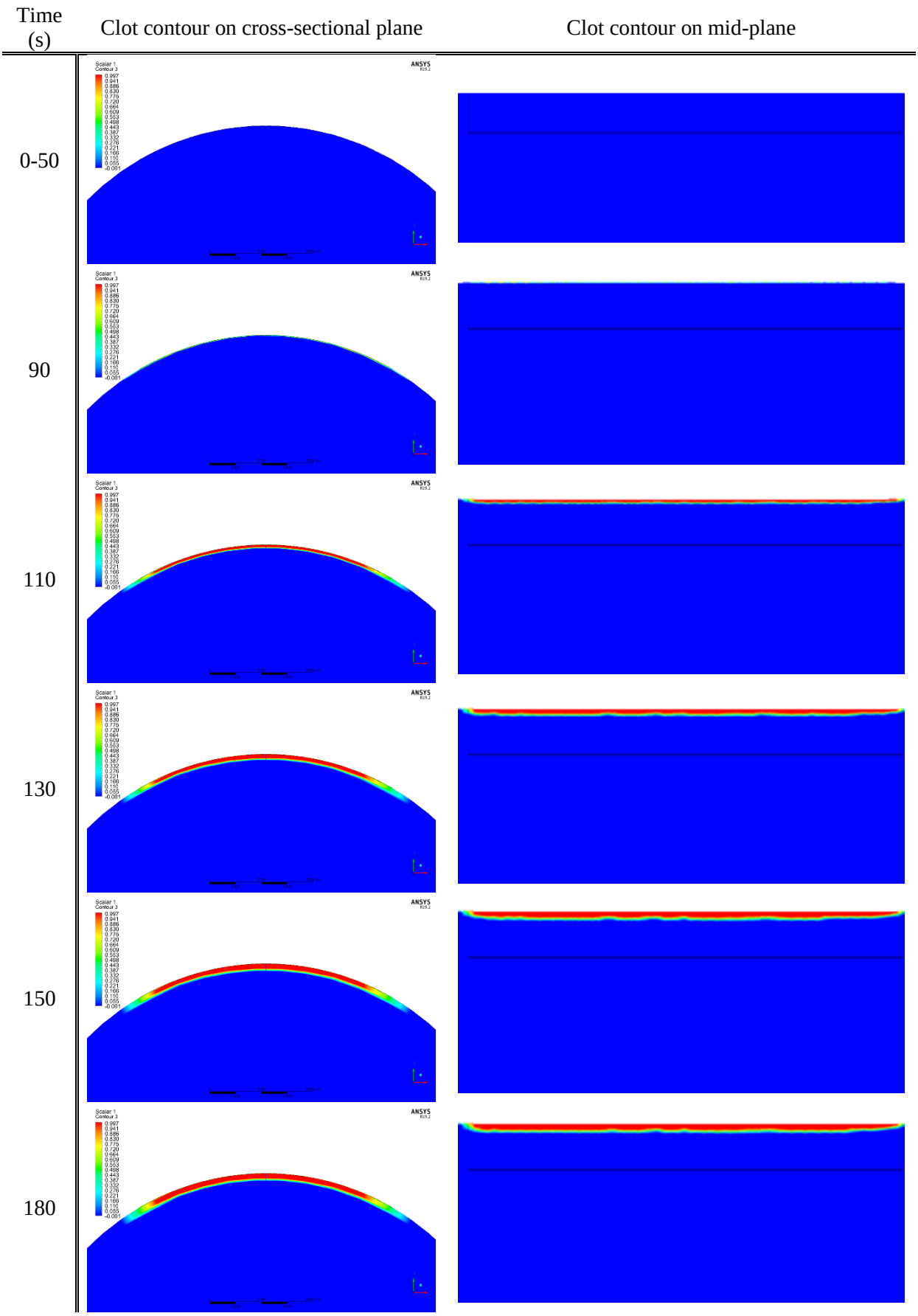

Figure 5.17: Illustration of how clot propagated in Model_1, showing clot on Midplane and cross-sectional plane.

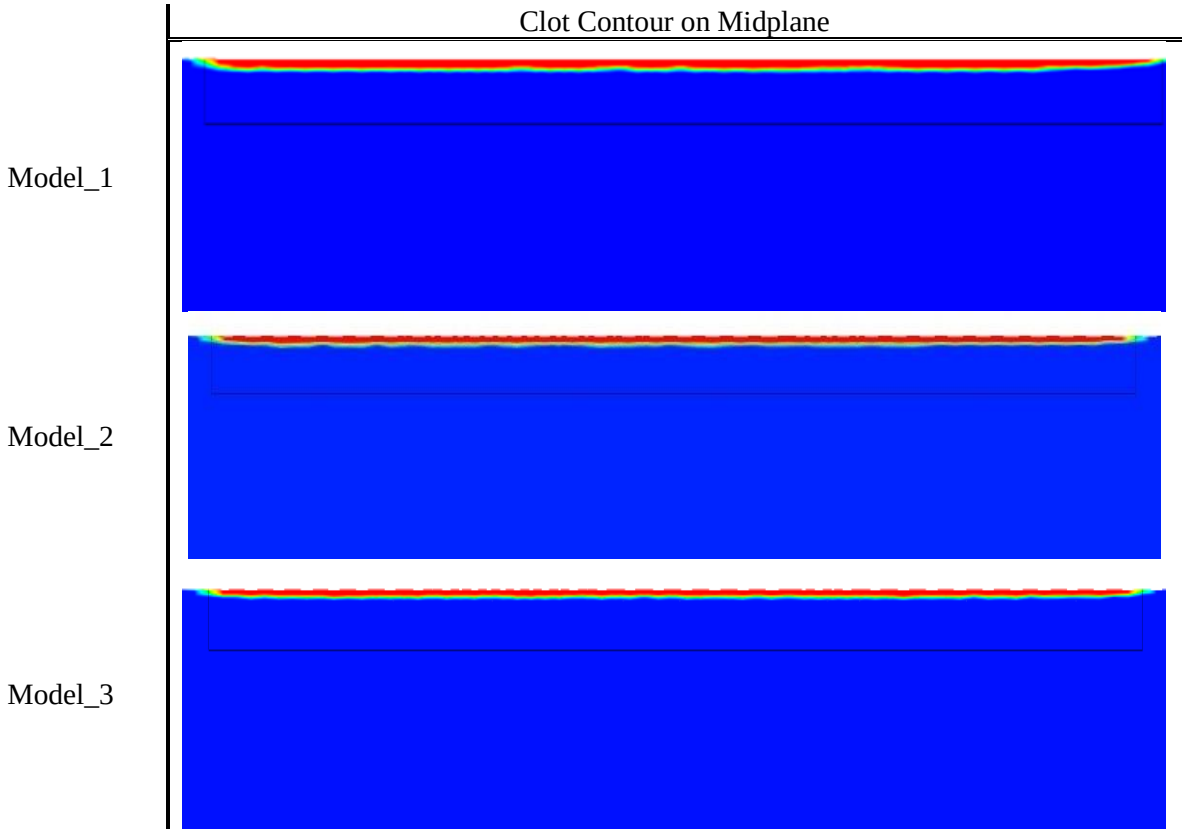

Figure 5.18: Comparing final clots formed in Models.

Clot formation in Models_4,5,6 was initiated when fibrin concentration reaches a threshold value. Model_4 was applied to show the changes in the biochemical species under steady flow. Figure 5.19 illustrates the changes in thrombin, fibrinogen and fibrin in Model_4 over time. A similar pattern can be identified in Model_5 and Model_6. However, due to the pulsatile nature of flow in these models, the concentrations were also pulsatile.

Thrombin concentration indicates that thrombin generation followed the defined profile and peaked at 198.8 nMol. However, thrombin consumption is slower than the defined rate. Fibrinogen concentration stayed constant until thrombin generation began. It then began to drop steadily by the same amount as fibrin increase. Figure 5.19(d) shows the maximum fibrin concentration in the vein over time. The value initially increases rapidly and later slows down until it reaches a peak value where it stays constant. Figure 5.20 below compares the clot volumes over time between Model_3 and 4. The clots formed in Models_4,5, and 6 are significantly larger than those in Models_1,2, and 3. Figure illustrates the clot volume comparison between Models_4,5, and 6.

Clot initiation in Model_5 occurred at t = 86.2 s and the peak volume of 2.41% was reached at t = 705.7s. Clot in Model_6 initiated at t = 87.1s and the peak volume of 1.74% was reached at t = 603.9s. In Model_4, Clot initiation occur at t = 86.02s. As shown in Figure 5.20: Comparison of the percentage of total volume covered by the clots in Model_4,5 and 6. Figure 5.20, the clot in Model_1 continues to

propagate at time t = 1000s. At this stage, the simulation was terminated and deemed to be too computationally expensive to predict the time that the clot reaches its peak size, since as the clot propagation rate was not reducing. At t = 1000s the clot has covered 1.42% of the vein in Model_1.

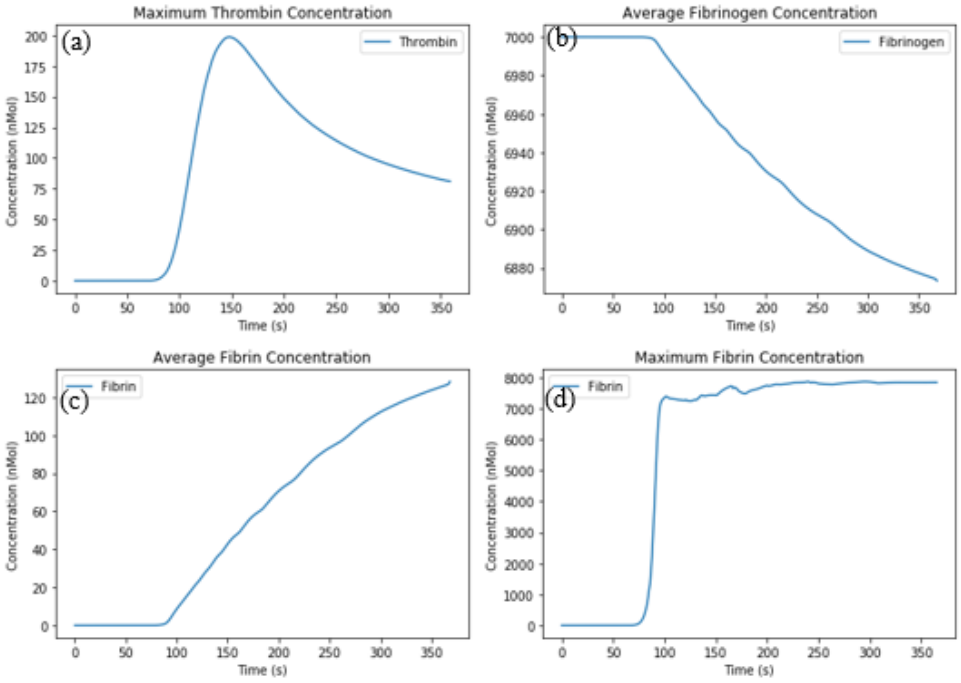

Figure 5.19:(a) Maximum thrombin concentration (b) Average fibrinogen concentration (c) Average Fibrin concentration (d) Maximum fibrin Concentration

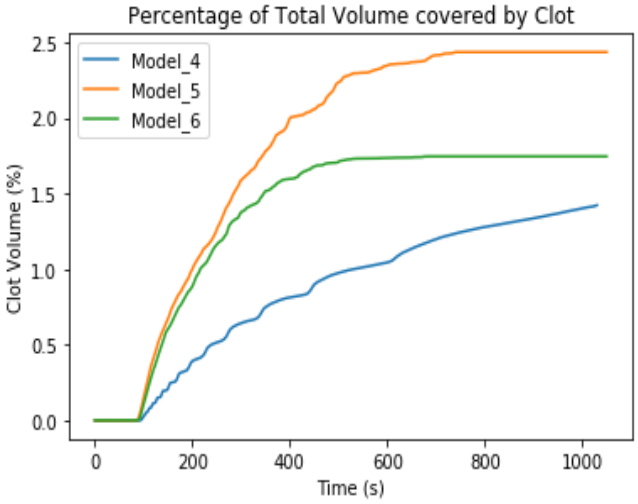

Figure 5.20: Comparison of the percentage of total volume covered by the clots in Model_4,5 and 6.

5.4. Experiment Clot Growth Validation

After developing the model, the results are validated by an experimental clot growth study. The study is aimed towards growing a clot in an experimental environment replicating the parameters from the computational model. This study follows the approach used by Ngoepe *et al* in their attempt to determine conditions under which fibrin formation occur under flow [134]. The membrane-based microfluidic technique used in their model was upscaled and manipulated to allow for easy visualization.

5.4.1. Specific Parameters for This Study

The aim is to grow a clot under similar conditions used in the computational model and compare the clots formed in both cases. To begin the experiment, physical parameters are determined. The Reynolds number from the computational model is matched with that of the experiment, as shown in Table 12. Steady blood flow is applied at the inlet and atmospheric pressure is applied at the pressure outlet. Thrombin was introduced into the flow as a liquid as opposed to the thrombin flux used in the computational model. A different computational simulation is performed in order to account for this. This simulation will have the same physical and biochemical properties as the experiment. However, the clot formation process from the model is implemented.

Table 12: Parameter values used in the computational model and experimental study.

Parameters	**Computational Model Values**	**Experimental Values**
Vein Diameter (mm)	10	10
Density (kg/m^3)	1050	1000
Viscosity (Pa.s)	0.004	0.001
Reynolds Number	364	364
Inlet Velocity (m/s)	0.1388	0.036
Flow rate (mL/min)	-	171

After diluting the fibrinogen and thrombin, the concentration used in the experiment is known, however this need to be translated to the computational model. Thrombin at concentration 100 mg/L is introduced into flow at 0.1mL/min and fibrinogen at concentration 100mg/L flows through the inlet at 171mL/min. The clot growth in the experiment occurs over 25s. At this flow rate, thrombin of constant concentration 120nMol is injected into flow and the concentration of fibrinogen is approximately 200nMol.

Geometry

A cylindrical PVC pipe was used as the geometry of interest, replicating the idealised computational model. A hole was drilled in the centre of the pipe for thrombin to be injected into flow. This geometry was developed computationally illustrated in Figure 5.21.

Mesh

A grid independence study was not performed on this geometry, however, to ensure the results are accurate, the mesh was made as fine as possible consisting of 500000 elements. the element size was 0.5mm and 10 inflation layers were employed at the vein walls.

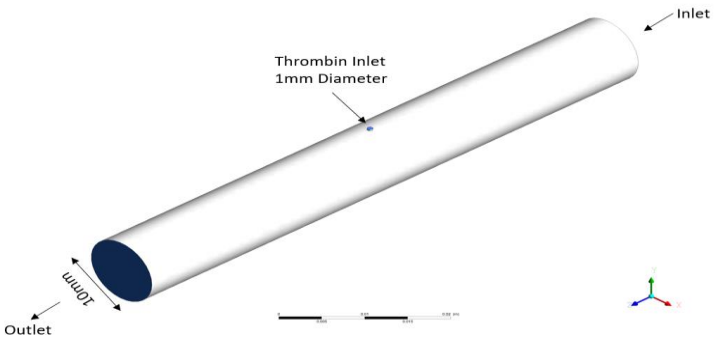

Figure 5.21: Experimental clot growth study simulation geometry

Setup

The overall setup of the simulation used is identical to that of the model developed in the idealised geometry. A few changes were made to account for the variations in physical properties. One of which is using a constant thrombin inflow instead of the generation profile used in the previous chapters. The porosity and permeability values used to represent the clotted region stayed the same. Fibrinogen enters through the inlet at velocity 0.036 m/s and zero-gauge pressure was applied at the outlet. PISO solver scheme was used to properly account for the porous media. The simulation is 30s long. The first 5 seconds allow for the flow to become stable and then thrombin is introduced into flow for the remaining 25s. A time step size of 0.01s is used. The results after 30s are viewed mainly using a plane in the centre of the vein along the length.

5.4.2. Experimental Validation Results

The experimental clot growth study does not give any quantitative result. The only result that can be derived from the study is the size and shape of the clot formed. Studying the clot propagation experimentally was not possible as the reacting components are transparent, and the fibrin fibres were therefore not visible. Hence the clot formed after 30s shown in Figure 5.22 was studied. Figure 5.23 shows the clot formed in the simulation and demonstrates are similarities in the shape and size of the clots formed between the experiment and the simulation results. The only deviation between the results is that the clot head in the simulation propagates towards the outlet more.

Figure 5.22: Clot formed in experimental study after 30s.

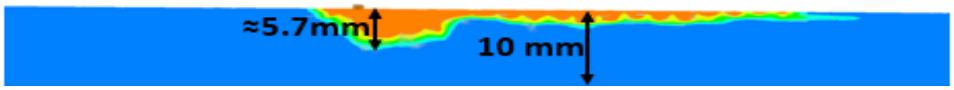

Figure 5.23: Clot formed by simulation after 30s.

5.5. Patient-Specific Geometry Design

In developing a patient-specific model, geometry segmentation and reconstruction are important. For this model, the geometry was derived from the CT scan of a 40 years-old male patient. The CT scan images were downloaded from Radiopedia.org, an open-source library for radiological related articles and cases. The patient involved recently underwent arthroscopic surgery and the CT scan was done to rule out pulmonary embolism. the CT images showed a large DVT present in the patient's left lower limb.

To develop a 3D geometry from CT images, the images must undergo segmentation. SYNOPSYS Simpleware Software was used for the segmentation of the region of interest. The software accurately process images, allows measurements to be taken and high-quality models can be generated. To prepare the images for segmentation, the images are resized. As the slices are not of the same pixel size. In these cases, Grzegorz's Simple Image Resizer 2012 package was used. The images are set to the default 630 × 627 pixels which is common in most of the images. To make segmentation easier and less complex for Simpleware, the images were converted from the 3D image with pixel value (R, B, G) into a grayscale image.

The greyscale .jpeg images were then imported into Simpleware. The spacing between each slice was manually defined as 5mm. Since this information was not provided with the CT scan, the chest to knee measurement of an average 40 years-old man is used. Simpleware processed the images and produced a 3-D body shown in Figure 5.24. Images of slices in planes x-z and y-z were also generated. On the images, the common femoral vein (CFV) is identified shown in Figure 5.25. Simpleware's "Threshold" method is used to differentiate and define the location of the CFV on each slice. As a result of image noise in some slices, the applied threshold value of 200 did not accurately account for the CFV. Manual segmentation, although highly subjective is hence applied in these slices. Knowing the clot is only present in the left limb, the CFV of the right limb was developed using the same methods to serve as the control.

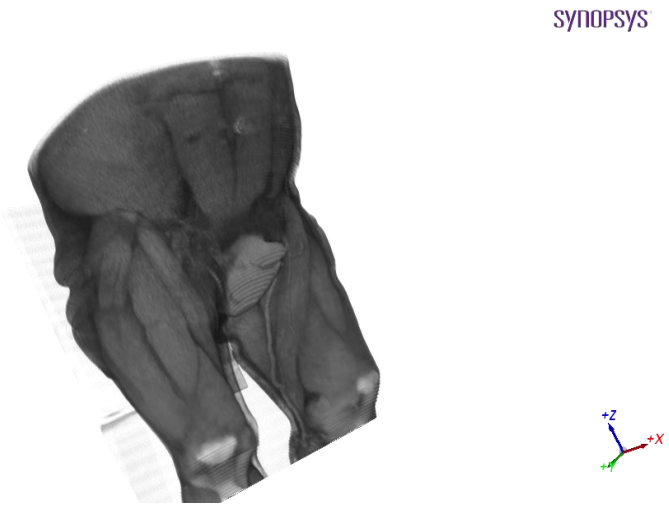

Figure 5.24: 3-D body generated by Simpleware from the 136 CT scan slices. Showing muscles and inner vessels.

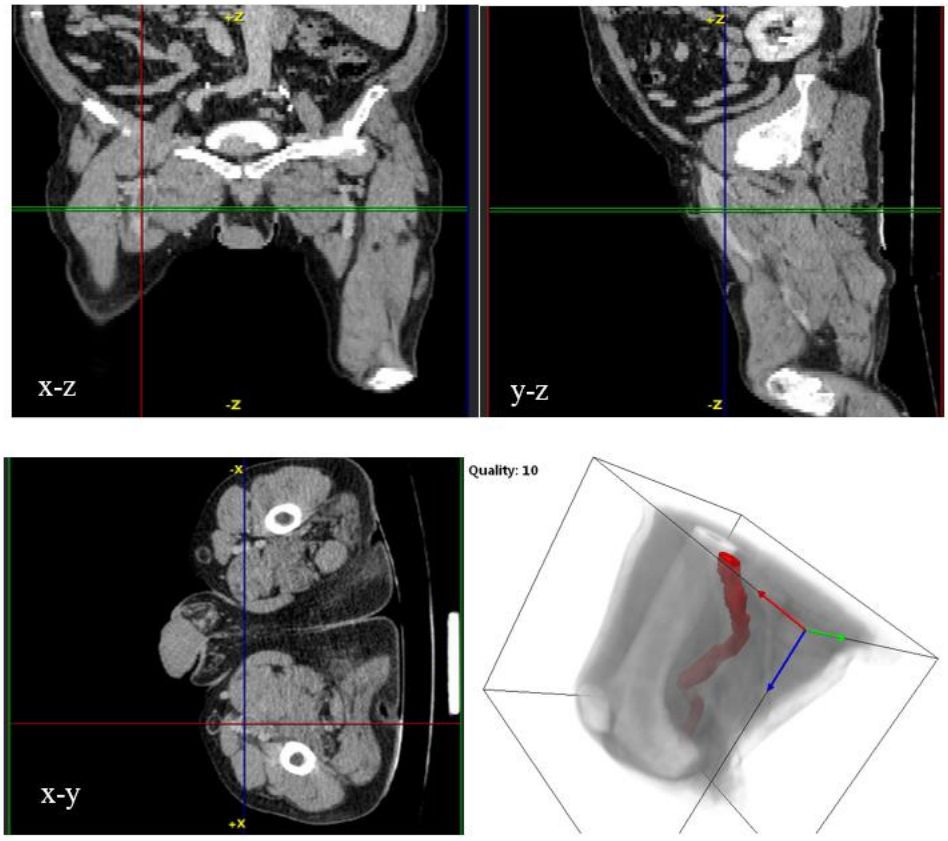

Figure 5.25: Image slices in planes x-y, x-z and y-z generated by Simpleware. CFV identified shown on each plane at the point of intersection of lines on the planes. Note the difference in pixelation, threshold value at these points is used on all slices to define the CFV.

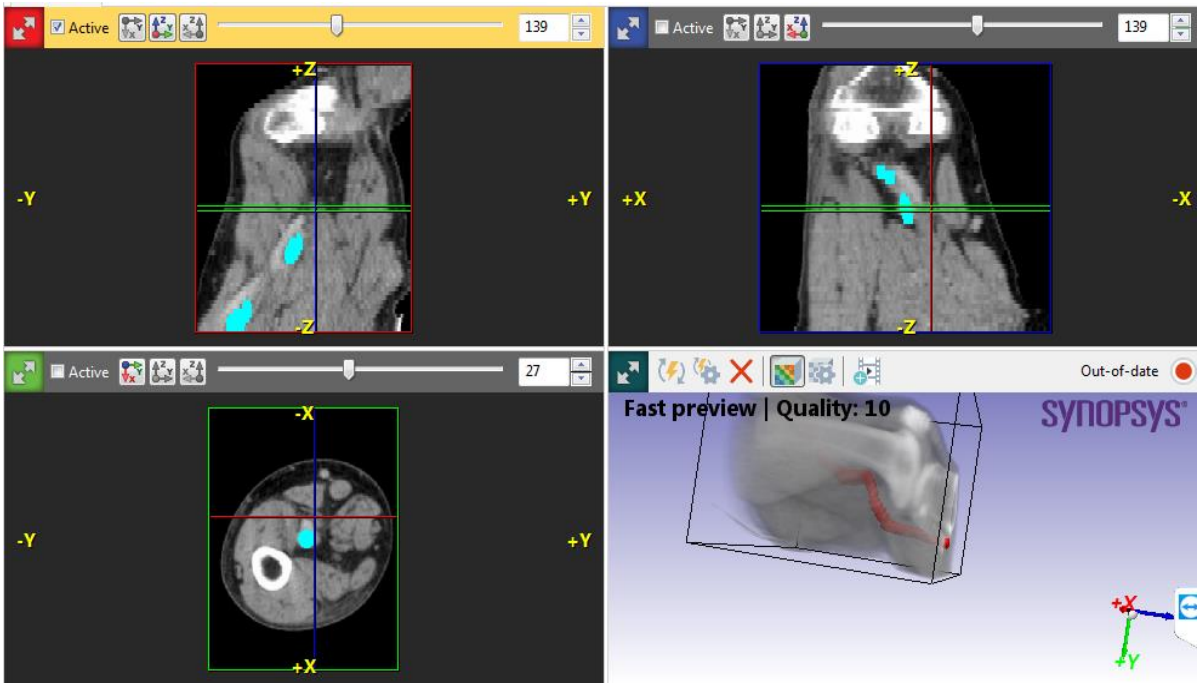

Figure 5.26: Image slices in planes x-y, x-z and y-z generated by Simpleware with CFV defined and generated.

For analysis, the clot was also developed using the threshold method. Figure 5.27 and Figure 5.28 shows the right and left CFV on the x-y plane and the clot present in the left CFV. On vein and clot surfaces, a Fourier smoothing function of order 10 was applied to eliminate the ragged finish generated as a result of the high segmentation spacing. The final geometries developed is shown in Figure 5.29.

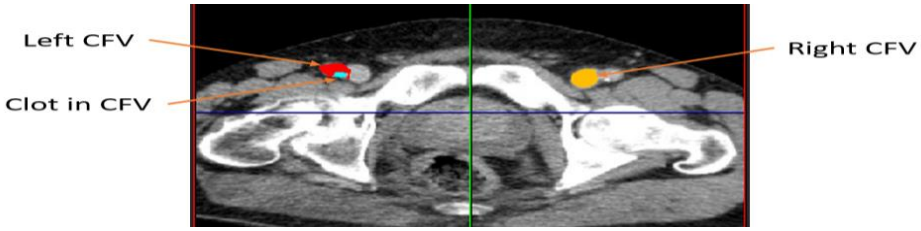

Figure 5.27: Showing the right (red) and left (yellow) CFV on the x-y plane. Also, clot formed (blue) in the left CFV is shown.

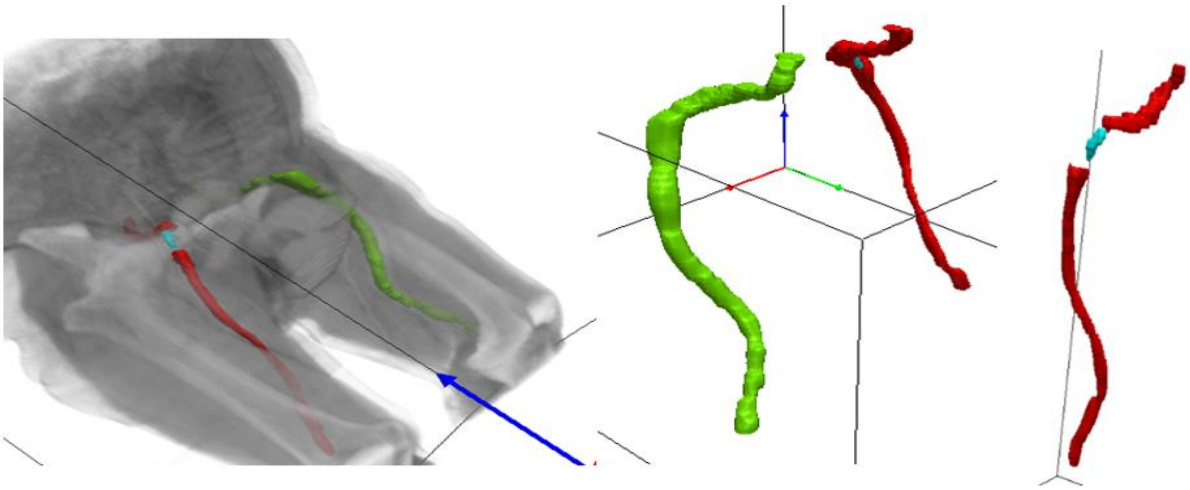

Figure 5.28: Showing the 3-D left and right CFV with the location and size of clot formed in the left CFV.

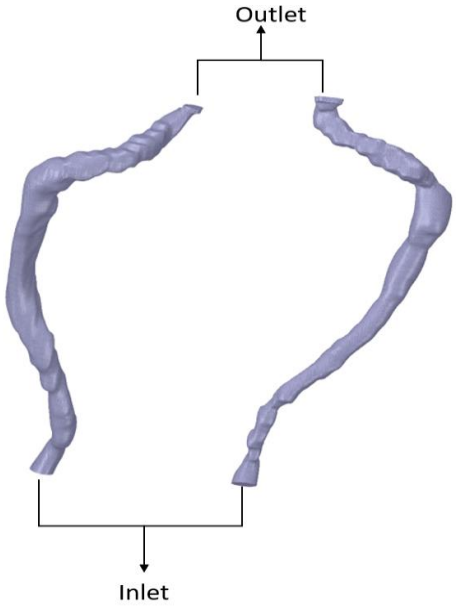

Figure 5.29: Segmented right and left CFV model after smoothening

5.6. Patient-Specific Geometry Results

According to Virchow's triad, the three factors that lead to clot initiation include hypercoagulability, Stagnation and injury to the vessel wall. In the patient-specific case studied in this work, there is no available information regarding the biochemical species in the blood. Also, no injury is identifiable on the vein wall. The evaluation performed in this section is purely qualitative and assumption are made in order to have the most physiological results. To begin the evaluation, clot initiation was determined by the blood flow pattern in the geometry. Areas with low velocity, stagnation or recirculation were studied.

5.6.1. Steady-State Simulation

A steady-state simulation is carried out on the left common femoral vein. based on the grid independence study in the idealised geometry, and the similarity of sizes, a grid of one million elements is used, which is one refinement level higher than the idealised geometry. Blood with density 1050 kg/m^3 and viscosity $4 \times 10^{-3}\ kg/ms$ enters the geometry through the inlet shown in Figure 5.29. To attain physiological conditions, a steady flow of velocity 0.1388 m/s was applied at the inlet and zero pressure at the outlet [51]. The wall is rigid, and a no-slip condition was applied. The same solvers and methods used in the idealised model were used in this model.

Due to the complex nature of the geometry, multiple planes were needed to visualize the flow in the vein. Figure 5.30 showing the velocity streamline from the steady-state simulation was used to determine the "areas of interest". These are zones where the flow has an unusual pattern, relatively low velocity, recirculation or stagnation.

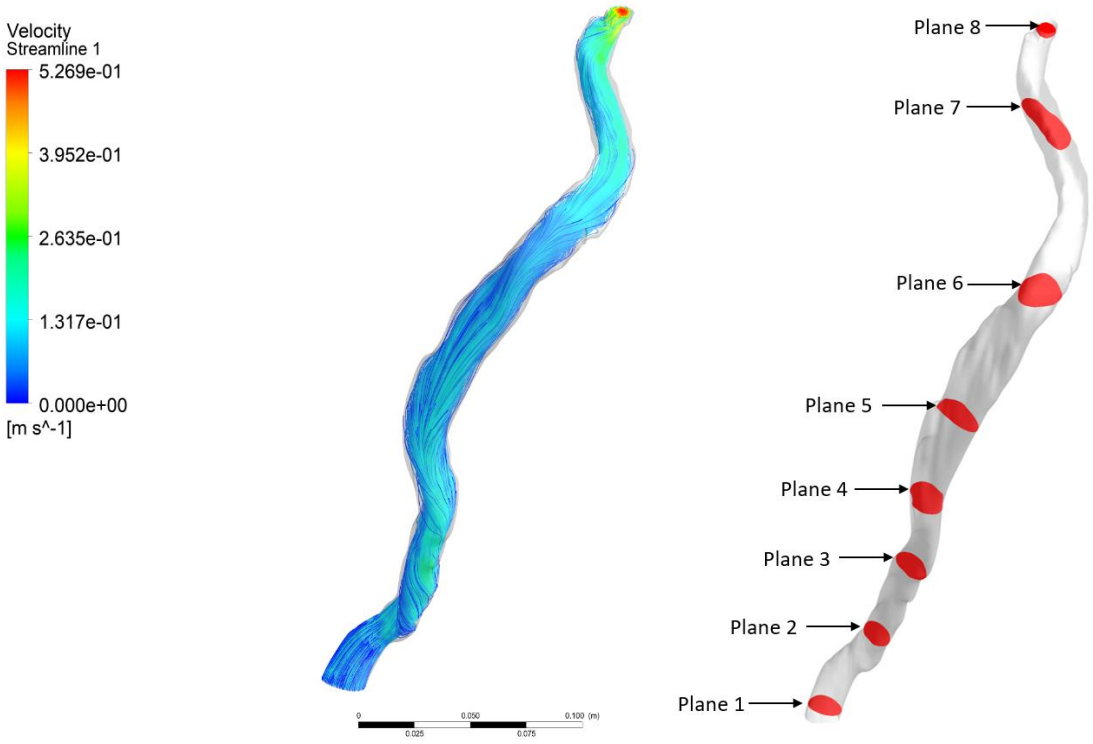

Figure 5.30: Left-Steady-state simulation velocity streamline. Right- Planes positioned at the "areas of interest"

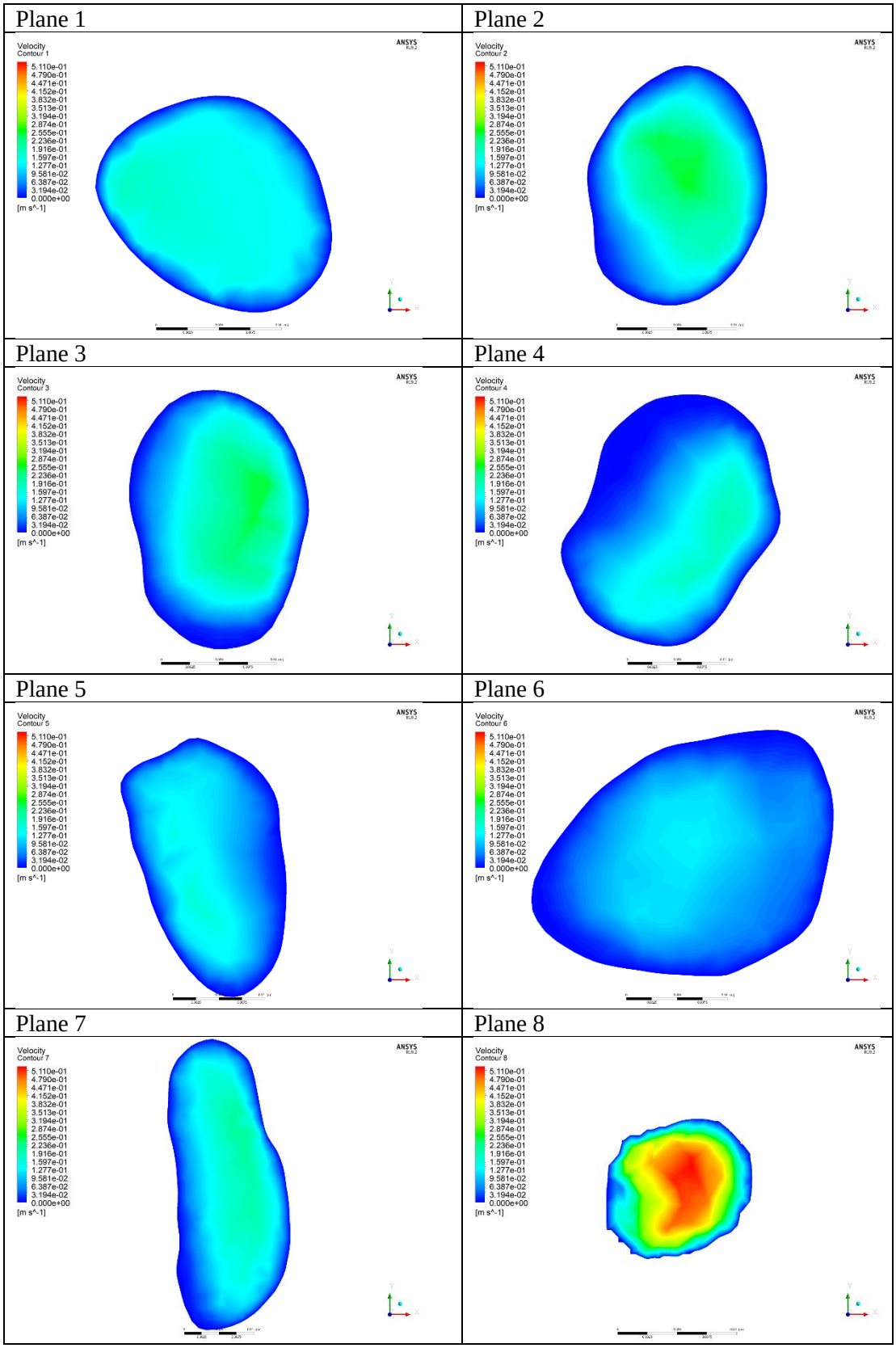

Figure 5.31: Velocity contours at planes of interest.

A study was performed evaluating the velocity contours at each of the planes. As expected, the peak velocity value on each plane was inversely proportional to the area of the plane shown in Figure 5.31. The pattern of flow and the position of the peak velocity on the planes were investigated. Planes 4 and 6 showed low velocity in a large area closest to the wall relative to other planes and clot initiation is predicted to occur in these areas. Figure 5.32 indicate the areas with low velocity, stagnation and recirculation on planes 4 and 6. Attention is paid to these areas in order to determine the initiation zone to be used in the transient simulation.

The other factor used to determine area, where the clot initiates, is strain rate. Ouared et al. proposed that platelet activation and fibrin formation will likely occur when the strain rate is below a threshold value of $100s^{-1}$ [135]. This threshold value is used to plot the strain rate contours in Figure 5.32 and Figure 5.33 where the colour legend is peaked at $100s^{-1}$, where areas with a strain rate higher than this threshold are depicted as red. The strain rate contour indicates the prediction that clot will initiate in areas around plane 4 and plane 6 is accurate. Plane 4 shows a large area on the wall with a strain rate close to zero and has a relatively large area with a strain rate above the threshold. On Plane 6, the strain rate is below the threshold in a large percentage of the area. There are also areas close to the vein wall with almost zero strain rates. These areas are chosen as the initiation zone for clot.

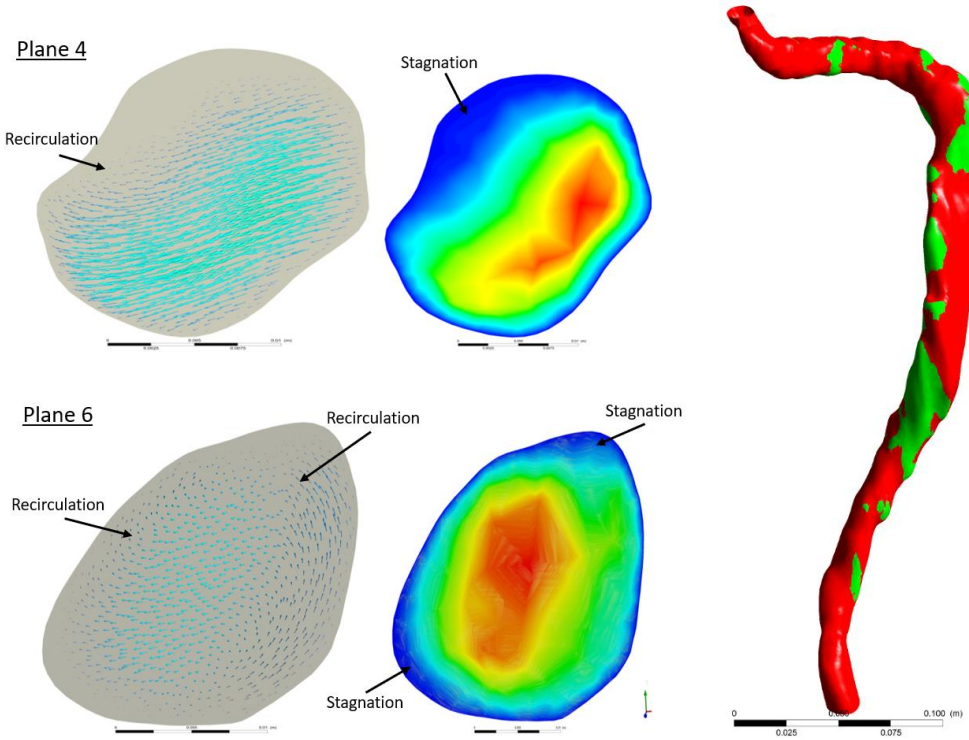

Figure 5.32: Right: Velocity vectors and local contours on plane 4 and 6, showing areas with stagnation and recirculation. Left: strain rate contour showing areas on the wall with strain rate less than the threshold $100s^{-1}$. These are areas where clot is likely to initiate.

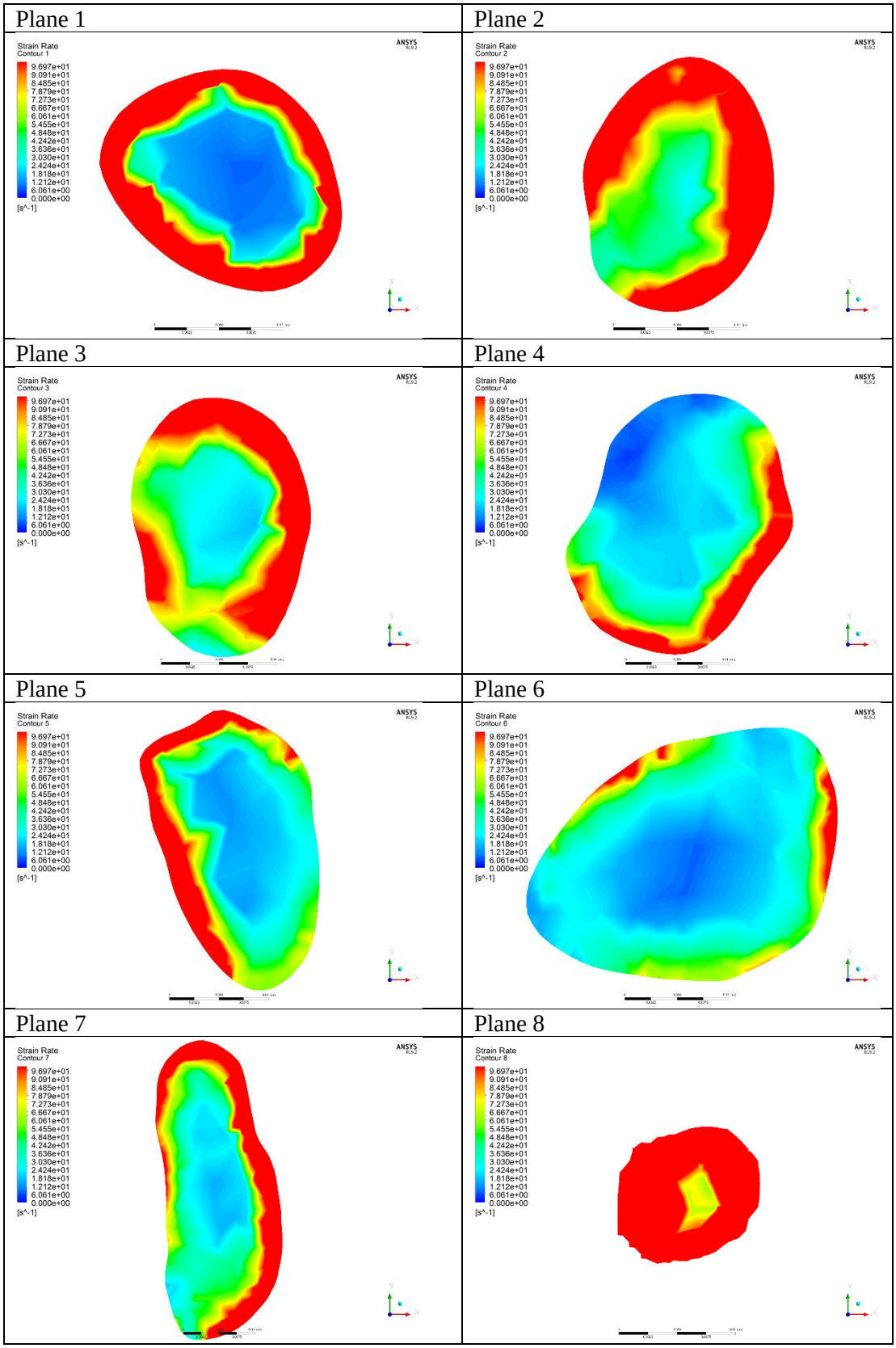

Figure 5.33: Strain rate contours on the planes of interest.

5.6.2. Transient-State Simulation

To reduce computational expense and to increase the accuracy of the results, the geometry was sliced to focus on the area around the clotted region, shown in Figure 5.35. After determining the areas that are likely to support clot initiation and propagation in the vein geometry, the model is applied to the geometry. This ensures that a more stable blood flow is attained at the injury site. To achieve this, the injury zone where thrombin is introduced into flow is designated. Figure 5.34 shows the selected injury zone for this transient simulation. This decision was supported by the location of the clot formed in the patient from the CT scan as shown in Figure 5.34. This was done to allow for comparison between the *in silico* and the *in vivo* clot.

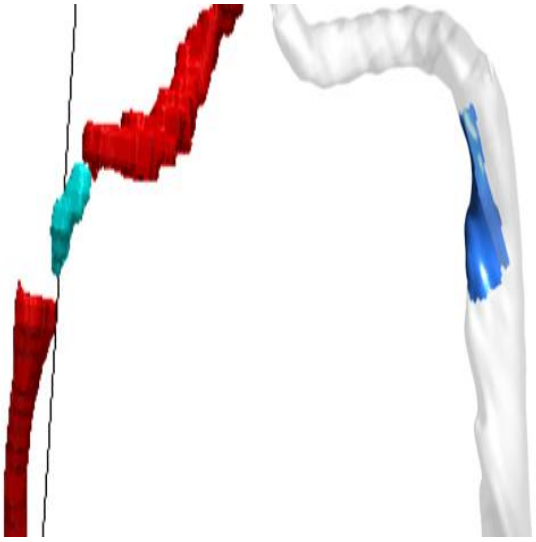

Figure 5.34: Illustration showing the size and location of clot formed in vivo (Left) and position of injury zone used for simulations (Right).

Fibrinogen of concentration 7000 nMol was introduced with blood at the inlet. It is understood that the *in vivo* clot formed under physiological conditions over an unknown period. Also, the shape and size of this clot have been under the influence of factors that are not accounted for by the model such as clot erosion, change in blood pressure/heart rate, and change in hormonal levels of the patient. Furthermore, it is understood that the vein is a flexible vessel and the geometry of the vein changes as the patient moves. However, this study assumes a fixed geometry in predicting the size and shape of clot when the patient is in that position. To reduce the computational cost, the simulation was performed over 100s. The clot formed after this time is used for evaluation in this study.

The velocity and strain rate are studied in pre-clot formation. Figure 5.35 shows the planes used for this initial study. After clot initiation, more attention is paid to the injury zone. Figure 5.36 shows the velocity and strain rate contours at the planes of interest at t = 10s when the flow is stable, but clot is yet to initiate. The peak velocities and strain rate on these planes are also indicated.

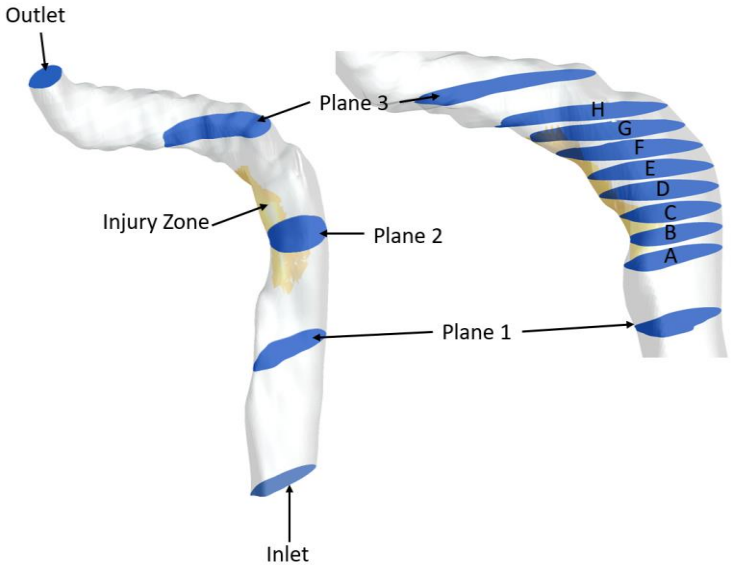

Figure 5.35: Illustration indicating planes of interest used for result analysis. Planes 1,2,3 are used to study the mechanical properties and planes A-H focussed on studying the clot formation.

	Velocity Contours	Strain Rate Contours	
Inlet Peak Velocity: 4.6 cm/s	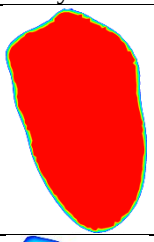	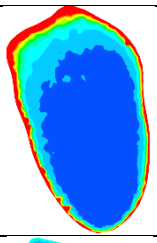	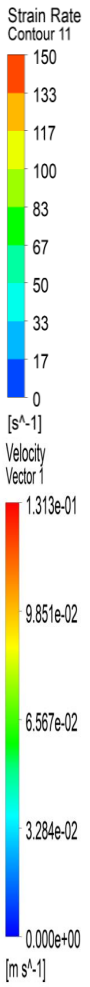
Plane 1 Peak Velocity: 6.4 cm/s	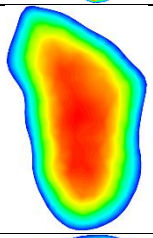	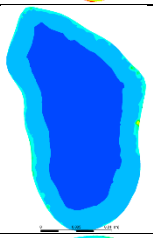	
Plane 2 Peak Velocity: 7.11 cm/s	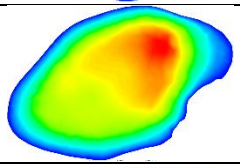	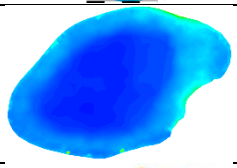	
Plane 3 Peak Velocity: 11.6 cm/s	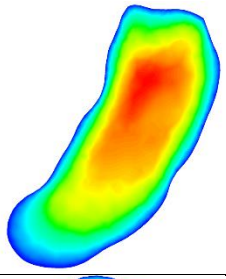	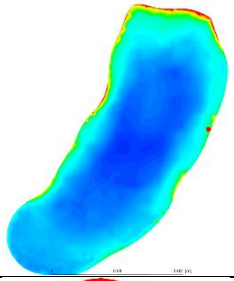	
Outlet Peak Velocity: 16.0 cm/s	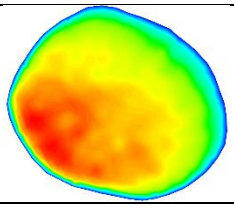	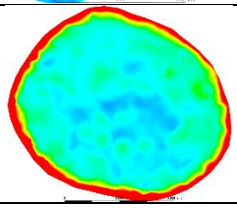	

Figure 5.36: Velocity and strain rate contours on planes of interest at t = 10s. Peak velocity on each plane also indicated.

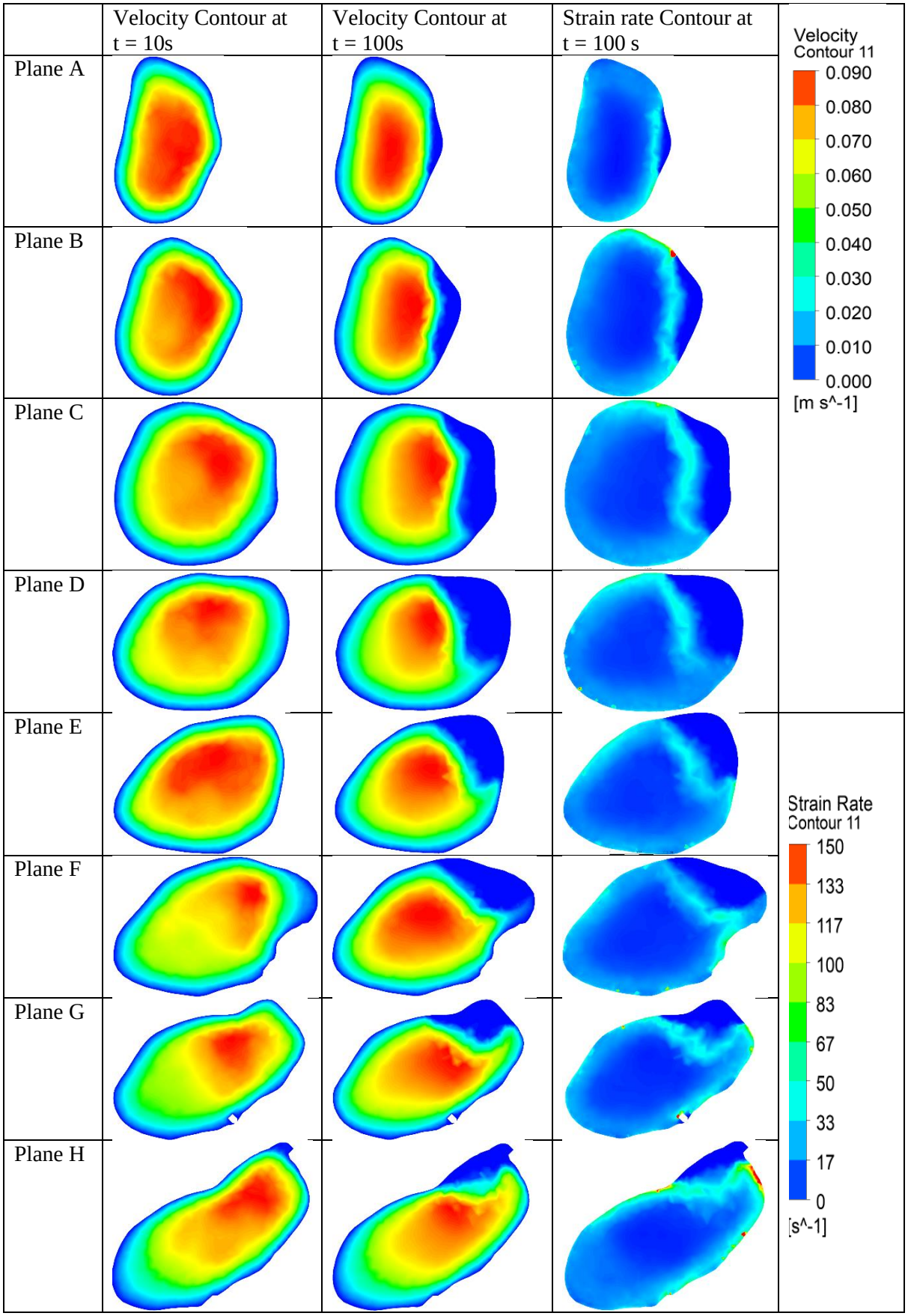

Figure 5.37: Contours comparing velocities at plane before (t = 10s) and after (t = 100s) clot formation. Strain rate contours showing increased strain rate on clot surface.

Figure 5.37 illustrates the flow velocity in the vein before and after clot formation on the planes of interest at the injury zone. The clot in the area obstructs flow and increase the peak velocity. The strain rate on these planes is also illustrated in Figure 5.37. The strain rate in the clotted region reduced to zero. However, the strain rate on the surface of the clot increased, but the value remains below $100s^{-1}$ indicating clot propagation still possible. Increased strain rate in noticed on Plane H which is closest to the clot tail. This is possibly a result of recirculation at the clot head, trapping thrombin and encouraging clot propagation.

The maximum thrombin and fibrin concentration in the vein over 100s are shown in Figure 5.38. Thrombin concentration increases steadily following the generation profile, however, the growing clot prevented most of the thrombin from getting transported away from the injury site by flow. Maximum fibrinogen stayed at 7000nMol. Fibrin concentration also increases steadily until a peak value of 13600nMol is reached. The volume of the clot was the only quantitative property that was investigated. The clot growth is similar to the thrombin concentration increase. Figure 5.38 shows the similarities between the *in vivo* clot and the one formed *in silico* after 100s. The clot growth over 100s is illustrated in Figure 5.39. The clot volume derived during segmentation was 2277.3 mm^3 and the in-silico clot had a volume of 2373.05 mm^3 after 100s.

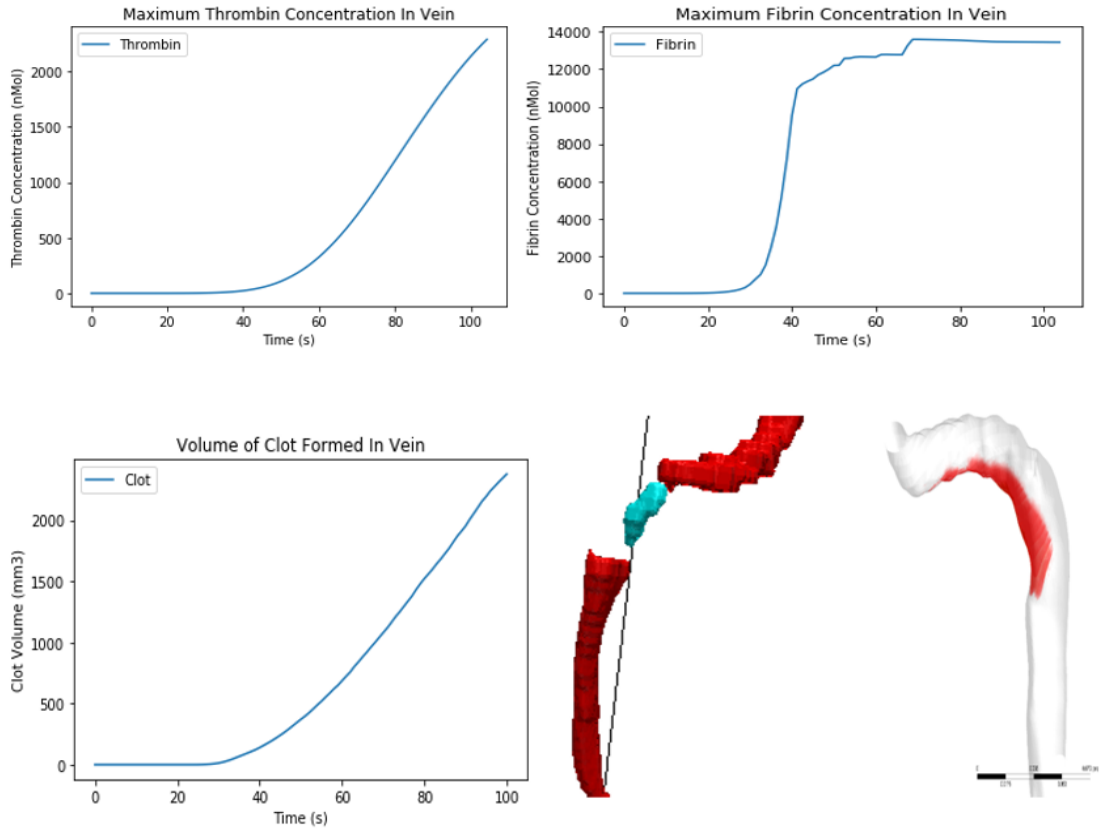

Figure 5.38: Top: Maximum thrombin and fibrin concentration in the vein over 100s. Bottom: Volume of clot formed in vein over 100s. Comparison between in vivo and in silico clot.

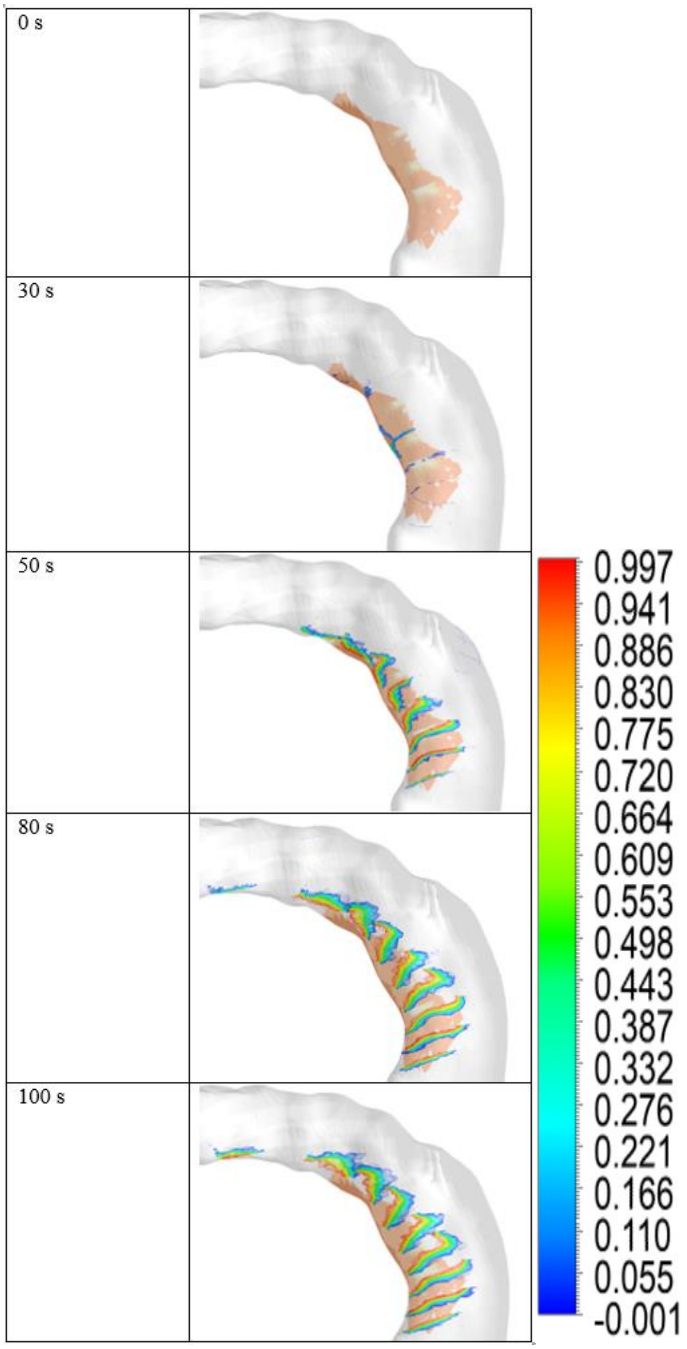

Figure 5.39: Contour showing clot growth over t = 100 s. Scalar = 1 for clot core, and > 0.5 for clot shell.

5.7. Discussion

This chapter describes a DVT model in an idealized three-dimensional geometry. The model accounts for the blood flow properties and a portion of the biochemical cascade that leads to clot formation in the vein. Computation methods were used to achieve this, where the biochemical species were introduced into the flow as scalars. The model development process helps elucidate the clotting process in DVT at different complexity levels of the model. Complicating the model will increase the computational expense and make the model less easy to use. The effects of the size of endothelial damage are investigated to some extent. The study of the relationships between biochemical factors and the blood mechanical factors, and how they affect clot formation helps us better understand Virchow's coagulation triad [71].

As explained in the earlier section of this chapter, blood flow plays a major role in the initiation and propagation of clot [79]. The clot was developed under steady and pulsatile flow. The flow was also modified to simulate the valve activity at the vein inlet. Before clot initiation, the blood flow was as expected. The parabolic steady flow was maintained in the steady flow model and parabolic pulsatile flow in the pulsatile models. The maximum strain rate was constant when the flow was steady. Pulsatile strain rates were seen in cases with pulsatile flow. The maximum strain rate value was almost 3 times higher in the model with valve activity than in the model with just pulsatile flow. This is due to the change in flow diameter as the valve opens and closes, causing divergence inflow at the inlet and recirculation around the inlet. Reversed flow caused by deceleration of blood due to clot stenosis and valve malfunction also caused a little increase in maximum strain rate value when clot initiates [93]. However, this increase was not noticed in some of the cycles. Further investigation would be required to understand this phenomenon more.

It has been elaborated in Chapter 4 that the peak velocity magnitude has a major effect on clot initiation. Results from this chapter show that changing the velocity profile but keeping the peak velocity the same does not have a significant effect on the initiation of clot. Clot under steady flow initiated about a second later than under pulsatile flow, this was the desirable outcome [73], [79], [87]. Reconfirming the claims in Chapter 4 that the main driving factor determining clot initiation is the biochemical concentrations, in this case, thrombin [45], [67].

A noticeable feature of the clot propagation is the erratic pattern whereby the growth rate increases then begin to decrease, and the cycle continues until the peak clot size is reached. The period of increase is the same as that of the decrease. The increase and decrease do not have the same period as the pulsatile blood flow. Although further investigation is required to understand why this occurs, this is predicted to be linked to the thrombin concentration. The low diffusivity value of thrombin does not allow thrombin transportation far down into flow. The erratic pattern noticed is a result of thrombin concentration exceeding the threshold value in the next vertical cell layer and the growth continues

horizontally. For the thrombin-based models, the propagation rate slows down after the thrombin peak concentration has been reached.

For the thrombin and fibrin-based models, the largest clot is formed when the blood velocity is pulsatile, and the valve is not present as proposed by Mori et al [78]. The smallest clot is formed under steady blood flow. The clot surface is under constant strain when the flow is steady as shown in Figure 5.13 and Figure 5.20. Thrombin gets transported away from the injury site and this limits the clot propagation. In the case with exclusively pulsatile flow, the strain rate increases and reduces to values closer to zero when the flow slows down. This improves thrombin diffusion and hence clot growth. Due to the maximum strain rate in the models with the valve activity being higher, the clots formed are smaller than in purely pulsatile cases this is as expected under the circumstances [101], [102].

Even though the clot initiation times and rate of propagation are similar, clots formed when the concentration of fibrinogen and fibrin are included in the model are about 5 times larger than when these biochemical species are not considered. This is due to continuous fibrin formation even after the thrombin concentration had dropped below the threshold value. The inclusion of fibrin in the model makes fibrin concentration the most important factor since fibrinogen concentration is constant as defended by Weisel et al. model [76]. The thrombin, fibrinogen and fibrin concentration in the vein changes over time in the same manner as derived by Bodnar and Sequira [94]. A slower thrombin dissipation rate was noticed when compared to the set profile. This is due to trapped thrombin inside the clot needing more time to get transported away from the injury site as noticed in Bodnar and Sequira's model [94].

The time taken for the fibrin-based model to reach the peak clot size is higher when compared to the thrombin-based models. The pulsatile cases have clot formed before t = 1000s but the clot in the steady case grows at a rate that is determined to be computationally expensive given the time available. The time step size can be increased to evaluate when the clot propagation will end, however, inaccurate clot size will be derived. The continuous growth is a result of steady fibrinogen supply and trapped thrombin getting diffused into the flow, slowing down the clot propagation. The models with valve activity reach their peak clot size first, followed by the purely pulsatile cases. This questions the assumption that the coagulation process can be simplified by accounting for just thrombin concentration in the model [122]. Since the predicted clot size and the propagation time is significantly less when the model is made thrombin based, it can be inferred that the assumption will not give an accurate prediction on the size and timing of the clot formed, though it can predict how clot forms and the shape of the clot [94].

The clot shape is based on the flow properties. The same shape is noticed when in the thrombin-based and the fibrin-based models with the same blood flow characteristics. Clotting under steady flow propagates in the same manner as Kadri et al [136]. Where an asymmetrical clot thinner closest to the inlet and grows thicker towards the outlet. For pulsatile cases, the clots were more symmetrical as a

result of isotropic diffusion when the velocity gets closer to zero. Also, clot formation towards the inlet occurred due to reversed flow. These models did not give a lot of information about the clot surfaces, but further investigations could be done to study these properties.

Interpreting the steady flow applied at the phantom's inlet to the computational vein's inlet was successful. Although there is no way to quantitatively examine the flow pattern in the phantom, it is presumed that the plug flow gradually developed into a Poiseuille flow as in the experiment. The strain rate at the vein wall was less than 100 s^{-1}, encouraging clot growth in that area. Since no quantitative properties could be used to compare the clot formation process, the size and shape of the clot are evaluated qualitatively [134].

Comparing the experimental study results to the results from the simulation, there are some observable differences in the shape and size of the clots. The experimental clot's height is higher than the computational clot. A rough estimation of this difference is done by drawing a line across the clot peak and measure the height of the clot relative to the vein diameter, as shown in Figure 5.22 and Figure 5.23. There is approximately a 24% (1.8 mm) difference between the heights of the formed clots.

A major assumption made in the simulation was that the vein wall was rigid, and a no-slip condition was applied as in most computational model [72], [83]–[85]. This does not correlate with the experimental study. The no-slip condition in the simulation ensured that the velocity at the wall is always zero and this allowed clot to stick to the wall. In the experimental study, clots formed in the initial trials got transported away from the injury site with the flow. To prevent this, a form of friction or tether was required around the injection to hold the clot in place. This was achieved by pushing the injection needle into the flow domain a bit. the needle disrupts the flow and holds the clot in place. This was not accounted for in the simulation and may explain the difference in height of the clot. Also, the clot of the computational clot propagates more towards the outlet. Ideally, since the same amount of biochemicals is pumped into both systems, the volume of the clots formed should be the same. Observations of clot migration in-vitro suggest that haemodynamic-induced forces exceeded tethering force on the (relatively smooth) phantom surface. This process was not considered in the in-silico model and any comparison seems flawed.

The experiment was limited mainly by the quantity of biochemicals available. Few trials were performed, and this did not allow the optimisation of the experiment. Ideally, multiple tests would have been done with varying parameters. Furthermore, ideally, the sensitivity of the experiment would have been tested on cases with the pulsatile flow or valval activity. Varying the inlet velocity would improve our understanding of how accurate the proposed model is over a range of inlet velocities. The inability to study the flow pattern in the experimental study prevents an in-depth discussion of the accuracy of the model or the clot formation process. For the scope of this research, this chapter proves that the

developed model predicts how and shape of clots formed to an extent, more research is required to investigate the qualitative properties of the formed clot.

The CT scan derived from the patient was segmented and the right and left CFV were derived. the similarities between these geometries encouraged the assumption that similar clot would form in both veins under the same conditions. The steady-state simulation is used to study the blood flow in the left CFV. This was used to determine the areas that support clot initiation based on the presence of low velocity or recirculation in the area. Figure 5.31 shows that there is increased stagnation around Plane 4 and 6. This area became the area of interest and the strain rate around the area is studied. Large area on the walls of Plane 4 and 6 had strain rate below $100s^{-1}$ which allow clot formation.

Figure 5.32 shows the vein geometry, wherein an increase in vein diameter occurred after the inlet leading to a decrease in diameter towards the outlet as also seen in Fortuny et al. [100]. This increased cross-sectional area is predicted to be the sinus of a venous valve, which was reinforced by clot formation around the area as predicted by Simao et al [98]. The developed model was then applied to the geometry after determining the area to represent the injury zone. Clot initiated in areas with increased cross-sectional area which agrees that support the claim that clot formation in the veins mostly occur around the valves [101], [103]–[105]. Clot initiation occurred at t = 25.325s and clot propagated to cover the injury zone. The biochemicals followed the same pattern as in the idealized geometry, however higher concentration was experienced as a result of stagnation zones trapping the biochemicals and increasing the concentrations.

Although thrombin generation had significantly reduced after 100s, clot propagation continues. The volume of the clot that formed in the patient was about 4% smaller than that formed in the simulation. This difference is a result of unaccounted for factors that occurred over time to the patient. Assumptions such as rigid walls and generalized biochemical concentrations also might have led to this difference. The 4% margin however falls within the acceptable margin for error determined in the clot growth experiment. The shape of the in-silico clot is the same as the in-vivo clot. A sharp increase in height and a slower decrease towards the outlet as shown in Figure 5.38. The other difference aside from the size of the clot is that the in-silico clot propagates more towards the outlet which explains the volume difference. The propagation may have been eliminated *in-vivo* by the patient movement which will change the geometry and shape of the clot.

A major limitation of using this model on patient-specific geometries is the computational cost incurred. Applying pulsatile flow at the inlet is expensive and was not applied with the model on this geometry. Although the clot is predicted to form in the valve's sinus, the model does not include the valve activity in order not to overly complicate the already complex flow. A more efficient code could increase the speed of the simulation and hence give room for increased simulation time and complexity. This method

should be implemented in many more geometries of other vessels in the body to determine improve the sensitivity of the model.

6. CONCLUSION AND RECOMMENDATIONS

This chapter provides a summary of the project aim of developing a mechano-chemical computational model of deep vein thrombosis. It discusses the methods taken to achieve this. The results from the developed model are summarized. Each chapter and the contribution they make to the developed model is discussed. It then recommends areas that should be focused on by future works.

6.1. Conclusion

Deep vein thrombosis is a common cardiovascular disease affecting over 200,000 people in South Africa yearly with over 60% of DVT cases leading to embolism which can be fatal. The mysterious nature of most DVT cases makes understanding, diagnosis and treatment problematic for clinicians. Improvement to the visualization, diagnosis and treatment of DVT is vital. Introducing CFD modelling gives the ability to investigate the physical and biochemical properties of clot formation process during DVT. It has the potential to improve the usefulness of medical imaging as a tool for disease prevention and inform drug prescription when models are applied to patient-specific cases.

The overall objective of this thesis was to develop a computational model that simulates deep vein thrombosis in the femoral vein. The purpose of this model is to help further understand the clot formation process. It assists in visualizing how clots propagate in a patient-specific geometry. The model has the potential to assist in the diagnosis and treatment of DVT in different patients. The developed model can be used to test out hypotheses without being invasive and at a relatively low cost.

Chapter 1 introduces DVT, explains how it leads to PE, and its incidence in South Africa. It then motivates the need for this research by explaining the importance of introducing CFD into medical imaging. The chapter acknowledges previous models and states the assumptions made by these models. It also states some of the areas that are lacking in previous models that will be included in the developed model. The next section then stated the overall objectives of the thesis, and studies that are carried out using the developed model are stated. The chapter concludes by stating the research's scope and the thesis plan of development.

Chapter 2 presents an overview of the pathophysiology of DVT, its risk factors, the currently used detection, diagnosis and treatment techniques. It describes normal blood flow in a healthy femoral vein. Computations modelling methods used to predict blood clot formation are described. The chapter then

describes haemostasis models that implemented CFD techniques. The section concludes with a review of computational and experimental DVT models from literature.

Chapter 3 describes the theoretical approach taken to develop the model and achieve the aim of the thesis. It begins by describing the general stages involved with CFD modelling. The fluid flow governing equations and their reference frames are then discussed. The general transport equation was also expressed. The next section describes the finite volume method used to solve the fluid flow equations and the biochemical transport equation. The third section discusses the cell discretization methods and the pressure-based solvers used to complete the simulations. Finally, the chapter describes the methods used to account for biochemical introduction, transport, reactions and formation of porous media.

Chapter 4 details the development of a two-dimensional mechano-chemical DVT model in an idealized femoral vein. The model was developed to help understand the clotting process under a physiological condition before increasing the complexity of the model. After a successful grid independence study, the model is used to compare clot formation when thrombin is introduced into the flow as a flux versus a fixed concentration. The study showed that the maximum concentration is higher when the flux boundary condition is applied. However, physiological conditions are not attained when using fixed concentration. The study indicated that to use the flux boundary condition, the concentration should be divided by a factor k derived by multiplying the injury zone area by the time step size. The model is then used to perform a parametric study of the blood velocity, thrombin concentration and vein diameter. This study aims to understand the effect of changing these factors on the clot size and determining which factor had the most impact on clot initiation and propagation. It is discovered that increasing the velocity and vein diameter causes a reduction in clot size and, increasing the thrombin peak concentration increases the clot size. Thrombin concentration showed to be the sole factor determining when clot initiation occurs and driving factor determining the size of the clot. The work in this chapter concurs with the claim by Wolberg et al that higher thrombin concentration produces denser, larger clots [126]. The flow properties and vessel geometry have lower impact on the initiation and propagation of clot within physiological value range compared to thrombin concentration.

Chapter 5 improves on the model developed in Chapter 4 by applying it to three-dimensional geometry. An idealised three-dimensional cylindrical geometry is used to represent the femoral vein with an injury zone on the wall. This geometry is used to gradually develop the final model by adding features to the model developed in Chapter 3 and studying the shape and size of the clot formed. The first feature included in the model was changing the steady parabolic flow velocity at the inlet to a pulsatile velocity digitized from a doppler sonography. Adding this feature increases the clot size as strain rate at the walls reduced significantly when the pulsatile flow is applied which accommodates clot initiation and propagation. The model then takes the valve activity into account. This is achieved by changing the

flow area at the inlet as the velocity magnitude changes. This property reduces the clot size compared to the purely pulsatile cases. The last feature added to the model was accounting for clot formation using fibrin concentration instead of thrombin concentration. The clot formed in this final model was larger, covering 1.5% of the vein volume. The thrombin, fibrin and fibrinogen concentration followed the same pattern over time as seen in literature.

Chapter 5 continues by validating the developed final model by applying an experimental clot growth study. In this study, a clot of known concentration was pumped at a known flow rate into the flow phantom. Thrombin is pumped in at the injury site and flow was carried out for 30 seconds. The clot formed experimentally is compared to the computationally grown clot. After carrying out a visual comparison between both clots, there is an approximately 24% difference between the height of these clot with the experimental clot being the thickest. The volumes of the clots are however proposed to be approximately the same because the computational clot propagated more towards the outlet. This difference is a result of the increased haemodynamic-induced forces exceeding the tethering force to the wall of the computational vein. The section concludes that the model predicts the shape of the clot formed to an extend with better accuracy attained in predicting the size of the clot.

The validated model is then applied to a patient-specific geometry. The geometry is derived by segmenting the patient's CT scan and the left femoral vein is exported as a .stl file. A steady-state simulation is carried out on the geometry to determine areas with stagnation or recirculation. This helps determine areas that clot is likely to initiate. Areas with strain rate less than 100 s^{-1} are also focused on. This method proves to be efficient as the location that is most susceptible to clot formation is predicted and it is in the same position as the clot present in the patient's vein. The injury zone is selected, to allow the thrombin generation. After 100s, the model generates a clot that is identical in size and shape to the clot in the patient's vein. The propagation towards the outlet noticed in the experimental validation is also noticed in this geometry.

The novelty of this work includes developing a framework that predicts clot formation in a patient-specific three-dimensional femoral vein geometry using CFD techniques and biochemical reactions. The model takes account of the blood flow, venous valves and biochemical reactions with clot forming obstructing flow due to its different porosity and permeability values. The model developed in this thesis is validated using an experimental clot growth study. Up until now, previous DVT models are mainly flow-based, studying areas of stagnation and recirculation. Most of them have solid valve walls and sinus. This model avoids this complexity by simulating blood flow coming out of the valve and includes biochemical reactions on the desired injury zone, which allows for further investigation of the clot formation process. This process also helps us study the initiation and propagation of clot as opposed to just knowing regions of clot formation.

6.2. Recommendations

The model developed in this thesis applied cardiovascular CFD to obtain the desired results, it is however important to recognized that this research is not at the peak of its potential. Further studies can be carried out as well as potential improvements to the model development methodology. The recommendations for further investigation and model development include:

- Improvement of each stage of the data acquisition process. The CT scan used for this project gives the instantaneous report of the patient, nothing is known about the patient history and how long the clot has been present. A database that keeps track of individual patient's information and scans over a long period of time should be developed. this helps us track the clot propagation and helps in future model development. A thrombogram could also be done on each the patients to improve the patient specificity of the model.
- The segmentation stage could be made less time consuming. An automated segmentation method could be developed to significantly reduce the time taken on this stage.
- A study should be performed to explore the other solver methods available. This study should be aimed at developing a less bulky model with reduced runtime.
- More parameters such as mesh types and fibrinogen concentration could be included in the parametric study, giving a broader understanding on how these factors affect clot formation.
- Including a valve sinus to the idealised geometry to study its effect on the clot formed in the area. Future models should pay more attention to the valval activity. Although idea of modelling flow at the inlet is a great representation. Flow through physiological valve does not always follow a pattern. The unpredictable pattern should be accounted flow.
- The clot surface should be studied as well as the clot mechanical properties and compared with physiological clots. The CFD model should allow for extraction of the clot as a solid and test performed on it.
- Experiment can be optimised and improved to study the flow properties. The same setup could be done using a particle image velocimetry (PIV) setup so the blood flow could be studied. Extracting the clot can also be done to study the fibrin mesh.

- Finally, the experimental and CFD studies could be done in a micro-scaled geometry. This reduces the computational expense and provide clearer detailed clots, whose properties and surface could be easily studied.

7. REFERENCES

[1] S. M. Waheed and D. T. Hotwagner, “Deep Vein Thrombosis (DVT),” in *StatPearls [Internet]*, StatPearls Publishing, 2018.

[2] P. A. Kyrle and S. Eichinger, “Deep vein thrombosis,” *Lancet*, vol. 365, no. 9465, pp. 1163–1174, 2005.

[3] M. Di Nisio, N. van Es, and H. R. Büller, “Deep vein thrombosis and pulmonary embolism,” *Lancet*, vol. 388, no. 10063, pp. 3060–3073, 2016.

[4] M. T. Severinsen, “Risk factors for venous thromboembolism: Smoking, anthropometry and genetic susceptibility,” *2010*, 2010.

[5] R. H. White and C. R. Keenan, “Effects of race and ethnicity on the incidence of venous thromboembolism,” *Thromb. Res.*, vol. 123, pp. S11--S17, 2009.

[6] S. S. Africa, *Mortality and causes of death in South Africa: Findings from death notification*. Statistics South Africa, 2017.

[7] M. Cushman *et al.*, “Deep vein thrombosis and pulmonary embolism in two cohorts: the longitudinal investigation of thromboembolism etiology,” *Am. J. Med.*, vol. 117, no. 1, pp. 19–25, 2004.

[8] D. Awolesi, M. Naidoo, and M. H. Cassimjee, “The profile and frequency of known risk factors or comorbidities for deep vein thrombosis in an urban district hospital in KwaZulu-Natal,” *South. Afr. J. HIV Med.*, vol. 17, no. 1, 2016.

[9] A. L. Marsden and J. A. Feinstein, “Computational modeling and engineering in pediatric and congenital heart disease,” *Curr. Opin. Pediatr.*, vol. 27, no. 5, p. 587, 2015.

[10] S. D. Team, “SimVascular.” SimVascular Development Team, 2017.

[11] “Radiopedia.” [Online]. Available: https://radiopaedia.org/.

[12] G. E. Blecher, “Diagnosing DVT in the Emergency Department: Combining Clinical Predictors, D-dimer and Bedside Ultrasound,” Université d’Ottawa/University of Ottawa, 2013.

[13] C. D. Buescher, B. Nachiappan, J. M. Brumbaugh, K. A. Hoo, and H. F. Janssen, “Experimental studies of the effects of abnormal venous valves on fluid flow,” *Biotechnol. Prog.*, vol. 21, no. 3, pp. 938–945, 2005.

[14] A. M. Aquila, “Deep venous thrombosis,” *J. Cardiovasc. Nurs.*, vol. 15, no. 4, pp. 25–44, 2001.

[15] U. Parimi, “COMPUTATIONAL FLUID DYNAMICS ANALYSIS OF DEEP VEINS WITH

FOCUS ON DEEP VEIN THROMBOSIS (DVT),” 2010.

[16] K. J. Franklin, “Valves in veins: an historical survey.” SAGE Publications, 1927.

[17] I. Healthwise, “No Title,” 2020. [Online]. Available: https://wake.nc.networkofcare.org/mh/library/article.aspx?hwid=zm2346. [Accessed: 04-Mar-2020].

[18] P. A. Kyrle, F. R. Rosendaal, and S. Eichinger, “Risk assessment for recurrent venous thrombosis,” *Lancet*, vol. 376, no. 9757, pp. 2032–2039, 2010.

[19] C. Kearon *et al.*, “Categorization of patients as having provoked or unprovoked venous thromboembolism: guidance from the SSC of ISTH,” *J. Thromb. Haemost.*, vol. 14, no. 7, pp. 1480–1483, 2016.

[20] C. Kearon *et al.*, “Antithrombotic therapy for VTE disease: antithrombotic therapy and prevention of thrombosis: American College of Chest Physicians evidence-based clinical practice guidelines,” *Chest*, vol. 141, no. 2, pp. e419S--e496S, 2012.

[21] K. E. Hodkinson and J. N. Mahlangu, “Deep-vein thrombosis in the era of high HIV and tuberculosis prevalence: A prospective review of its diagnosis and treatment in a quaternary centre,” *South African Med. J.*, vol. 107, no. 10, 2017.

[22] R. Hughes, “Venous thrombo-embolism associated with long distance air travel,” ResearchSpace@ Auckland, 2006.

[23] R. J. Darwood and F. C. T. Smith, “Deep vein thrombosis,” *Surg.*, vol. 31, no. 5, pp. 206–210, 2013.

[24] A. T. Rocha, E. F. Paiva, A. Lichtenstein, R. Milani Jr, C. Cavalheiro-Filho, and F. H. Maffei, “Risk-assessment algorithm and recommendations for venous thromboembolism prophylaxis in medical patients,” *Vasc. Health Risk Manag.*, vol. 3, no. 4, p. 533, 2007.

[25] J. Hill and T. Treasure, “Reducing the risk of venous thromboembolism in patients admitted to hospital: summary of NICE guidance,” *Bmj*, vol. 340, p. c95, 2010.

[26] P. S. Wells *et al.*, “Value of assessment of pretest probability of deep-vein thrombosis in clinical management,” *Lancet*, vol. 350, no. 9094, pp. 1795–1798, 1997.

[27] P. S. Wells *et al.*, “Evaluation of D-dimer in the diagnosis of suspected deep-vein thrombosis,” *N. Engl. J. Med.*, vol. 349, no. 13, pp. 1227–1235, 2003.

[28] L. W. Tick *et al.*, “Practical diagnostic management of patients with clinically suspected deep vein thrombosis by clinical probability test, compression ultrasonography, and D-dimer test,”

Am. J. Med., vol. 113, no. 8, pp. 630–635, 2002.

[29] A. Cogo *et al.*, "Compression ultrasonography for diagnostic management of patients with clinically suspected deep vein thrombosis: prospective cohort study," *Bmj*, vol. 316, no. 7124, pp. 17–20, 1998.

[30] C. Kearon, J. S. Ginsberg, and J. Hirsh, "The role of venous ultrasonography in the diagnosis of suspected deep venous thrombosis and pulmonary embolism," *Ann. Intern. Med.*, vol. 129, no. 12, pp. 1044–1049, 1998.

[31] A. W. A. Lensing *et al.*, "Detection of deep-vein thrombosis by real-time B-mode ultrasonography," *N. Engl. J. Med.*, vol. 320, no. 6, pp. 342–345, 1989.

[32] R. Quintavalla *et al.*, "Duplex ultrasound diagnosis of symptomatic proximal deep vein thrombosis of lower limbs," *Eur. J. Radiol.*, vol. 15, no. 1, pp. 32–36, 1992.

[33] N. J. Langford, G. Stansby, and L. Avital, "The management of venous thromboembolic diseases and the role of thrombophilia testing: summary of NICE Guideline CG144.," *Acute Med.*, vol. 11, no. 3, pp. 138–142, 2012.

[34] P. A. Loud, D. S. Katz, D. A. Bruce, D. L. Klippenstein, and Z. D. Grossman, "Deep venous thrombosis with suspected pulmonary embolism: detection with combined CT venography and pulmonary angiography," *Radiology*, vol. 219, no. 2, pp. 498–502, 2001.

[35] F. C. Sampson, S. W. Goodacre, S. M. Thomas, and E. J. R. van Beek, "The accuracy of MRI in diagnosis of suspected deep vein thrombosis: systematic review and meta-analysis," *Eur. Radiol.*, vol. 17, no. 1, p. 175, 2007.

[36] P. A. Loud, Z. D. Grossman, D. L. Klippenstein, and C. E. Ray, "Combined CT venography and pulmonary angiography: a new diagnostic technique for suspected thromboembolic disease.," *AJR. Am. J. Roentgenol.*, vol. 170, no. 4, pp. 951–954, 1998.

[37] M. Das *et al.*, "Optimized image reconstruction for detection of deep venous thrombosis at multidetector-row CT venography," *Eur. Radiol.*, vol. 16, no. 2, pp. 269–275, 2006.

[38] G. Greisen, "Methods to assess systemic and organ blood flow in the neonate," in *Hemodynamics and Cardiology: Neonatology Questions and Controversies*, Elsevier, 2012, pp. 81–94.

[39] F. A. Anderson, W. W. Durgin, and H. B. Wheeler, "Interpretation of venous occlusion plethysmography using a nonlinear model," *Med. Biol. Eng. Comput.*, vol. 24, no. 4, pp. 379–385, 1986.

[40] R. M. Blumenberg, E. Barton, M. L. Gelfand, P. Skudder, and J. Brennan, "Occult deep venous

thrombosis complicating superficial thrombophlebitis," *J. Vasc. Surg.*, vol. 27, no. 2, pp. 338–343, 1998.

[41] E. Kesieme, C. Kesieme, N. Jebbin, E. Irekpita, and A. Dongo, "Deep vein thrombosis: a clinical review," *J. Blood Med.*, vol. 2, p. 59, 2011.

[42] C. S. Joels, R. F. Sing, and B. T. Heniford, "Complications of inferior vena cava filters," *Am. Surg.*, vol. 69, no. 8, p. 654, 2003.

[43] M. Naccarato, F. C. Grandi, M. Dennis, and P. A. G. Sandercock, "Physical methods for preventing deep vein thrombosis in stroke," *Cochrane Database Syst. Rev.*, no. 8, 2010.

[44] F. C. Grandi, P. Sandercock, M. Miccio, and R. M. Salvi, "Physical methods for preventing deep vein thrombosis in stroke," *Stroke*, vol. 36, no. 5, pp. 1102–1103, 2005.

[45] S. A. Smith, "The cell-based model of coagulation," *J. Vet. Emerg. Crit. care*, vol. 19, no. 1, pp. 3–10, 2009.

[46] C. D. Cheek and S. W. Day, "Evaluation of a numerical thrombosis model for a high shear rotating flow," in *ASME 2008 6th International Conference on Nanochannels, Microchannels, and Minichannels*, 2008, pp. 1621–1627.

[47] D. O'Neil, "Blood components," *San Marcos Palomar Coll.*, 2012.

[48] D. Elad and S. Einav, "Physical and flow properties of blood," *Stand. Handb. Biomed. Eng. Des. McGraw-Hill, New York*, pp. 1–3, 2003.

[49] M. A. Panteleev *et al.*, "Spatial propagation and localization of blood coagulation are regulated by intrinsic and protein C pathways, respectively," *Biophys. J.*, vol. 90, no. 5, pp. 1489–1500, 2006.

[50] P. Abraham, G. Leftheriotis, B. Desvaux, M. Saumet, and J. L. Saumet, "Diameter and velocity changes in the femoral vein during thermal stress in humans," *Clin. Physiol.*, vol. 14, no. 1, pp. 15–21, 1994.

[51] A. Fronek, M. H. Criqui, J. Denenberg, and R. D. Langer, "Common femoral vein dimensions and hemodynamics including Valsalva response as a function of sex, age, and ethnicity in a population study," *J. Vasc. Surg.*, vol. 33, no. 5, pp. 1050–1056, 2001.

[52] G. L. Moneta, G. Bedford, K. Beach, and D. E. Strandness, "Duplex ultrasound assessment of venous diameters, peak velocities, and flow patterns," *J. Vasc. Surg.*, vol. 8, no. 3, pp. 286–291, 1988.

[53] J. D. Coffman and J. A. Lempert, "Venous flow velocity, venous volume and arterial blood

flow.," *Circulation*, vol. 52, no. 1, pp. 141–145, 1975.

[54] C. R. Lattimer, M. Azzam, E. Kalodiki, X. Y. Xu, and G. Geroulakos, "Hemodynamic changes in the femoral vein with increasing outflow resistance," *J. Vasc. Surg. Venous Lymphat. Disord.*, vol. 2, no. 1, pp. 26–33, 2014.

[55] C. Jeanneret, K. H. Labs, M. Aschwanden, A. Bollinger, U. Hoffmann, and K. Jäger, "Physiological reflux and venous diameter change in the proximal lower limb veins during a standardised Valsalva manoeuvre," *Eur. J. Vasc. Endovasc. Surg.*, vol. 17, no. 5, pp. 398–403, 1999.

[56] T. Hayakawa and M. Abe, "Femoral venous flow velocity during passive ankle exercise in patients with chronic spinal cord injury," *J. Phys. Ther. Sci.*, vol. 31, no. 8, pp. 682–686, 2019.

[57] R. T. Eberhardt and J. D. Raffetto, "Chronic venous insufficiency," *Circulation*, vol. 130, no. 4, pp. 333–346, 2014.

[58] R. L. M. Kurstjens *et al.*, "Intravenous pressure changes in patients with postthrombotic deep venous obstruction: results using a treadmill stress test," *J. Thromb. Haemost.*, vol. 14, no. 6, pp. 1163–1170, 2016.

[59] C. G. Caro, T. J. Pedley, R. C. Schroter, and W. A. Seed, *The mechanics of the circulation*. Cambridge University Press, 2012.

[60] D. Kumar, R. Vinoth, and V. S. Raviraj Adhikari, "Non-Newtonian and Newtonian blood flow in human aorta: a transient analysis," 2017.

[61] H. E. A. Baieth, "Physical parameters of blood as a non-Newtonian fluid," *Int. J. Biomed. Sci. IJBS*, vol. 4, no. 4, p. 323, 2008.

[62] S. C. O. Noutchie, D. R. R. MARITZ, and S. B. O. GUTTO, "Flow of a Newtonian fluid: The case of blood in large arteries," *Master Sci. Univ. South Africa*, 2005.

[63] C. Tu and M. Deville, "Pulsatile flow of non-Newtonian fluids through arterial stenoses," *J. Biomech.*, vol. 29, no. 7, pp. 899–908, 1996.

[64] F. J. H. Gijsen, F. N. van de Vosse, and J. D. Janssen, "The influence of the non-Newtonian properties of blood on the flow in large arteries: steady flow in a carotid bifurcation model," *J. Biomech.*, vol. 32, no. 6, pp. 601–608, 1999.

[65] P. D. Ballyk, D. A. Steinman, and C. R. Ethier, "Simulation of non-Newtonian blood flow in an end-to-side anastomosis," *Biorheology*, vol. 31, no. 5, pp. 565–586, 1994.

[66] K. Perktold, R. Peter, and M. Resch, "Pulsatile non-Newtonian blood flow simulation through a

bifurcation with an aneurysm," *Biorheology*, vol. 26, no. 6, pp. 1011–1030, 1989.

[67] M. Hoffman, "Remodeling the blood coagulation cascade," *J. Thromb. Thrombolysis*, vol. 16, no. 1–2, pp. 17–20, 2003.

[68] N. Mackman, R. E. Tilley, and N. S. Key, "Role of the extrinsic pathway of blood coagulation in hemostasis and thrombosis," *Arterioscler. Thromb. Vasc. Biol.*, vol. 27, no. 8, pp. 1687–1693, 2007.

[69] J. H. Morrissey, "Plasma factor Vila: measurement and potential clinical significance," *Pathophysiol. Haemost. Thromb.*, vol. 26, no. Suppl. 1, pp. 66–71, 1996.

[70] J. A. Oliver, D. M. Monroe, H. R. Roberts, and M. Hoffman, "Thrombin activates factor XI on activated platelets in the absence of factor XII," *Arterioscler. Thromb. Vasc. Biol.*, vol. 19, no. 1, pp. 170–177, 1999.

[71] N. S. Wijeratne and K. A. Hoo, "An analytical approach to identify fluid flow separation and re-attachment in a collapsible channel," *Comput. Chem. Eng.*, vol. 31, no. 4, pp. 346–360, 2007.

[72] S. Yesudasan and R. D. Averett, "Recent Advances in Computational Modeling of Thrombosis," *arXiv Prepr. arXiv1801.02048*, 2018.

[73] Z. Xu, M. Kamocka, M. Alber, and E. D. Rosen, "Computational approaches to studying thrombus development," *Arterioscler. Thromb. Vasc. Biol.*, vol. 31, no. 3, pp. 500–505, 2011.

[74] K. Lo, W. S. Denney, and S. L. Diamond, "Stochastic modeling of blood coagulation initiation," *Pathophysiol. Haemost. Thromb.*, vol. 34, no. 2–3, pp. 80–90, 2005.

[75] M. F. Hockin, K. C. Jones, S. J. Everse, and K. G. Mann, "A model for the stoichiometric regulation of blood coagulation," *J. Biol. Chem.*, vol. 277, no. 21, pp. 18322–18333, 2002.

[76] J. W. Weisel and C. Nagaswami, "Computer modeling of fibrin polymerization kinetics correlated with electron microscope and turbidity observations: clot structure and assembly are kinetically controlled," *Biophys. J.*, vol. 63, no. 1, pp. 111–128, 1992.

[77] Z. Yang, I. Mochalkin, and R. F. Doolittle, "A model of fibrin formation based on crystal structures of fibrinogen and fibrin fragments complexed with synthetic peptides," *Proc. Natl. Acad. Sci.*, vol. 97, no. 26, pp. 14156–14161, 2000.

[78] D. Mori, K. Yano, K. Tsubota, T. Ishikawa, S. Wada, and T. Yamaguchi, "Simulation of platelet adhesion and aggregation regulated by fibrinogen and von Willebrand factor," *Thromb. Haemost.*, vol. 99, no. 01, pp. 108–115, 2008.

[79] I. V Pivkin, P. D. Richardson, and G. Karniadakis, "Blood flow velocity effects and role of

activation delay time on growth and form of platelet thrombi," *Proc. Natl. Acad. Sci.*, vol. 103, no. 46, pp. 17164–17169, 2006.

[80] S. Ravanshadi and M. Jahed, "Mathematical modeling of human blood clotting formation," in *2007 6th International Special Topic Conference on Information Technology Applications in Biomedicine*, 2007, pp. 273–276.

[81] J. D. Murray, *Mathematical biology: I. An introduction*, vol. 17. Springer Science & Business Media, 2007.

[82] A. A. Valencia, A. M. Guzmán, E. A. Finol, and C. H. Amon, "Blood flow dynamics in saccular aneurysm models of the basilar artery," 2006.

[83] E. N. Sorensen, G. W. Burgreen, W. R. Wagner, and J. F. Antaki, "Computational simulation of platelet deposition and activation: I. Model development and properties," *Ann. Biomed. Eng.*, vol. 27, no. 4, pp. 436–448, 1999.

[84] P. D. Goodman, E. T. Barlow, P. M. Crapo, S. F. Mohammad, and K. A. Solen, "Computational model of device-induced thrombosis and thromboembolism," *Ann. Biomed. Eng.*, vol. 33, no. 6, pp. 780–797, 2005.

[85] K. Leiderman and A. L. Fogelson, "Grow with the flow: a spatial--temporal model of platelet deposition and blood coagulation under flow," *Math. Med. Biol. a J. IMA*, vol. 28, no. 1, pp. 47–84, 2011.

[86] V. Govindarajan, V. Rakesh, J. Reifman, and A. Y. Mitrophanov, "Computational study of thrombus formation and clotting factor effects under venous flow conditions," *Biophys. J.*, vol. 110, no. 8, pp. 1869–1885, 2016.

[87] N. Filipovic, M. Kojic, and A. Tsuda, "Modelling thrombosis using dissipative particle dynamics method," *Philos. Trans. R. Soc. A Math. Phys. Eng. Sci.*, vol. 366, no. 1879, pp. 3265–3279, 2008.

[88] A. Tosenberger, F. Ataullakhanov, N. Bessonov, M. Panteleev, A. Tokarev, and V. Volpert, "Modelling of thrombus growth and growth stop in flow by the method of dissipative particle dynamics," *Russ. J. Numer. Anal. Math. Model.*, vol. 27, no. 5, pp. 507–522, 2012.

[89] A. Tosenberger, F. Ataullakhanov, N. Bessonov, M. Panteleev, A. Tokarev, and V. Volpert, "Modelling of thrombus growth in flow with a DPD-PDE method," *J. Theor. Biol.*, vol. 337, pp. 30–41, 2013.

[90] A. Tosenberger, N. Bessonov, and V. Volpert, "Influence of fibrinogen deficiency on clot formation in flow by hybrid model," *Math. Model. Nat. Phenom.*, vol. 10, no. 1, pp. 36–47,

2015.

[91] Z. Xu, N. Chen, M. M. Kamocka, E. D. Rosen, and M. Alber, “A multiscale model of thrombus development,” *J. R. Soc. Interface*, vol. 5, no. 24, pp. 705–722, 2008.

[92] H. Hosseinzadegan and D. K. Tafti, “Modeling thrombus formation and growth,” *Biotechnol. Bioeng.*, vol. 114, no. 10, pp. 2154–2172, 2017.

[93] S. C. Shadden and S. Hendabadi, “Potential fluid mechanic pathways of platelet activation,” *Biomech. Model. Mechanobiol.*, vol. 12, no. 3, pp. 467–474, 2013.

[94] T. Bodnar and A. Sequeira, “Numerical simulation of the coagulation dynamics of blood,” *Comput. Math. Methods Med.*, vol. 9, no. 2, pp. 83–104, 2008.

[95] N. K. G. Ramunigari and D. Roy, “Numerical simulations of thrombosis,” *Chronicles Young Sci.*, vol. 4, no. 2, p. 130, 2013.

[96] B. Savage, E. Sald\’\ivar, and Z. M. Ruggeri, “Initiation of platelet adhesion by arrest onto fibrinogen or translocation on von Willebrand factor,” *Cell*, vol. 84, no. 2, pp. 289–297, 1996.

[97] N. Ibrahim, N. S. A. Aziz, and A. N. A. Manap, “Vein mechanism simulation study for deep vein thrombosis early diagnosis using cfd,” in *Journal of Physics: Conference Series*, 2017, vol. 822, no. 1, p. 12040.

[98] M. Simão, J. M. Ferreira, J. Mora-Rodriguez, and H. M. Ramos, “Identification of DVT diseases using numerical simulations,” *Med. Biol. Eng. Comput.*, vol. 54, no. 10, pp. 1591–1609, 2016.

[99] S. Xu, Z. Xu, O. V Kim, R. I. Litvinov, J. W. Weisel, and M. Alber, “Model predictions of deformation, embolization and permeability of partially obstructive blood clots under variable shear flow,” *J. R. Soc. Interface*, vol. 14, no. 136, p. 20170441, 2017.

[100] G. Fortuny *et al.*, “Effect of anticoagulant treatment in deep vein thrombosis: A patient-specific computational fluid dynamics study,” *J. Biomech.*, vol. 48, no. 10, pp. 2047–2053, 2015.

[101] N. Noda, M. Nakano, H. Matsuura, T. Nemoto, and K. Koide, “Numerical analysis of blood flow in vessels,” in *First International Conference on Innovative Computing, Information and Control-Volume I (ICICIC’06)*, 2006, vol. 3, pp. 545–546.

[102] T. Ohashi, H. Liu, and T. Yamaguchi, “Computational fluid dynamic simulation of the flow through venous valve,” in *Clinical application of computational mechanics to the cardiovascular system*, Springer, 2000, pp. 186–189.

[103] A. J. Narracott, J. M. T. Keijsers, C. A. D. Leguy, W. Huberts, and F. N. van de Vosse, “Fluid-structure interaction analysis of venous valve hemodynamics,” in *4th International Conference*

on Computational & Mathematical Biomedical Engineering (CMBE15), June 29-July 1, 2015, Cachan, France, 2015, pp. 31–34.

[104] F. Lurie, R. L. Kistner, and B. Eklof, "The mechanism of venous valve closure in normal physiologic conditions," *J. Vasc. Surg.*, vol. 35, no. 4, pp. 713–717, 2002.

[105] Z. Hajati, F. S. Moghanlou, M. Vajdi, S. E. Razavi, and S. Matin, "Fluid-structure interaction of blood flow around a vein valve," *Bioimpacts*, vol. 10, no. 3, pp. 169–175, 2020.

[106] P. Jagadeeswaran, B. C. Cooley, P. L. Gross, and N. Mackman, "Animal models of thrombosis from zebrafish to nonhuman primates: use in the elucidation of new pathologic pathways and the development of antithrombotic drugs," *Circ. Res.*, vol. 118, no. 9, pp. 1363–1379, 2016.

[107] S. Wessler and M. T. Connelly, "Studies in intravascular coagulation. I. Coagulation changes in isolated venous segments," *J. Clin. Invest.*, vol. 31, no. 11, pp. 1011–1014, 1952.

[108] M. S. Runyon, M. A. Gellar, N. Sanapareddy, J. A. Kline, and J. A. Watts, "Development and comparison of a minimally-invasive model of autologous clot pulmonary embolism in Sprague-Dawley and Copenhagen rats," *Thromb. J.*, vol. 8, no. 1, p. 3, 2010.

[109] K. Kishore, "In vitro and in vivo screening methods for antithrombotic agents," *Am. J. Phytomed. Clin. Ther*, vol. 1, pp. 497–506, 2013.

[110] A. Narracott *et al.*, "Development and validation of models for the investigation of blood clotting in idealized stenoses and cerebral aneurysms," *J. Artif. Organs*, vol. 8, no. 1, pp. 56–62, 2005.

[111] M. V Ovanesov, N. M. Ananyeva, M. A. Panteleev, F. I. Ataullakhanov, and E. L. Saenko, "Initiation and propagation of coagulation from tissue factor-bearing cell monolayers to plasma: initiator cells do not regulate spatial growth rate," *J. Thromb. Haemost.*, vol. 3, no. 2, pp. 321–331, 2005.

[112] A. A. Onasoga-Jarvis, T. J. Puls, S. K. O'Brien, L. Kuang, H. J. Liang, and K. B. Neeves, "Thrombin generation and fibrin formation under flow on biomimetic tissue factor-rich surfaces," *J. Thromb. Haemost.*, vol. 12, no. 3, pp. 373–382, 2014.

[113] S. Prasad, R. S. Kashyap, J. Y. Deopujari, H. J. Purohit, G. M. Taori, and H. F. Daginawala, "Development of an in vitro model to study clot lysis activity of thrombolytic drugs," *Thromb. J.*, vol. 4, no. 1, pp. 1–4, 2006.

[114] K. B. Neeves, D. A. R. Illing, and S. L. Diamond, "Thrombin flux and wall shear rate regulate fibrin fiber deposition state during polymerization under flow," *Biophys. J.*, vol. 98, no. 7, pp. 1344–1352, 2010.

[115] A. Fluent, "ANSYS fluent theory guide 15.0," *Inc, Canonsburg, PA*, 2013.

[116] A. Soleimani, G. Sheikhzadeh, and R. Maddahian, “Improving the performance of the physical influence scheme (PIS) for cell-centred finite volume method,” *Modares Mech. Eng.*, vol. 16, no. 12, pp. 571–582, 2017.

[117] S. L. Diamond, “Systems analysis of thrombus formation,” *Circ. Res.*, vol. 118, no. 9, pp. 1348–1362, 2016.

[118] J. Fitzgerald, R. McMonnies, A. Sharkey, P. L. Gross, and K. Karkouti, “Thrombin generation and bleeding in cardiac surgery: a clinical narrative review,” *Can. J. Anesth. Can. d’anesthésie*, pp. 1–8, 2020.

[119] H. C. Hemker *et al.*, “The calibrated automated thrombogram (CAT): a universal routine test for hyper-and hypocoagulability,” *Pathophysiol. Haemost. Thromb.*, vol. 32, no. 5–6, pp. 249–253, 2002.

[120] R. M. W. Kremers, B. De Laat, R. J. Wagenvoord, and H. C. Hemker, “Computational modelling of clot development in patient-specific cerebral aneurysm cases: comment,” *J. Thromb. Haemost.*, vol. 15, no. 2, pp. 395–396, 2017.

[121] A. L. Marsden, “Optimization in cardiovascular modeling,” *Annu. Rev. Fluid Mech.*, vol. 46, pp. 519–546, 2014.

[122] M. N. Ngoepe and Y. Ventikos, “Computational modelling of clot development in patient-specific cerebral aneurysm cases,” *J. Thromb. Haemost.*, vol. 14, no. 2, pp. 262–272, 2016.

[123] J. J. Hathcock, “Flow effects on coagulation and thrombosis,” *Arterioscler. Thromb. Vasc. Biol.*, vol. 26, no. 8, pp. 1729–1737, 2006.

[124] D. F. Young, “Fluid mechanics of arterial stenoses,” 1979.

[125] S. Kattula, J. R. Byrnes, and A. S. Wolberg, “Fibrinogen and fibrin in hemostasis and thrombosis,” *Arterioscler. Thromb. Vasc. Biol.*, vol. 37, no. 3, pp. e13--e21, 2017.

[126] A. S. Wolberg, D. M. Monroe, H. R. Roberts, and M. Hoffman, “Elevated prothrombin results in clots with an altered fiber structure: a possible mechanism of the increased thrombotic risk,” *Blood, J. Am. Soc. Hematol.*, vol. 101, no. 8, pp. 3008–3013, 2003.

[127] M. Kopernik, “Modelling of blood thrombosis at the microscopic and mesoscopic scales,” *Comput. Assist. Methods Eng. Sci.*, vol. 25, no. 1, pp. 21–45, 2019.

[128] E. W. Davie and O. D. Ratnoff, “Waterfall sequence for intrinsic blood clotting,” *Science (80-.).*, vol. 145, no. 3638, pp. 1310–1312, 1964.

[129] R. G. Macfarlane, “An enzyme cascade in the blood clotting mechanism, and its function as a

biochemical amplifier," *Nature*, vol. 202, no. 4931, pp. 498–499, 1964.

[130] Z. Wu, Z. Xu, O. Kim, and M. Alber, "Three-dimensional multi-scale model of deformable platelets adhesion to vessel wall in blood flow," *Philos. Trans. R. Soc. A Math. Phys. Eng. Sci.*, vol. 372, no. 2021, p. 20130380, 2014.

[131] J. E. Selis and S. Kadakia, "Venous Doppler sonography of the extremities: a window to pathology of the thorax, abdomen, and pelvis," *Am. J. Roentgenol.*, vol. 193, no. 5, pp. 1446–1451, 2009.

[132] A. Rohatgi, "WebPlotDigitizer," *2010*. [Online]. Available: https://automeris.io/WebPlotDigitizer/.

[133] L. D. C. Casa, D. H. Deaton, and D. N. Ku, "Role of high shear rate in thrombosis," *J. Vasc. Surg.*, vol. 61, no. 4, pp. 1068–1080, 2015.

[134] N. M.N., T. E. Pretorius I.J, S. Z, V. Y, and H. W-H, "Thrombin-fibrinogen in vitro flow model of thrombus growth in cerebral aneurysms. Thrombosis and Haemostasis," *Thromb. Haemost. Open. 2021. Press*.

[135] R. Ouared, B. Chopard, B. Stahl, D. A. Rüfenacht, H. Yilmaz, and G. Courbebaisse, "Thrombosis modeling in intracranial aneurysms: a lattice Boltzmann numerical algorithm," *Comput. Phys. Commun.*, vol. 179, no. 1–3, pp. 128–131, 2008.

[136] O. E. Kadri, V. D. Chandran, M. Surblyte, and R. S. Voronov, "In vivo measurement of blood clot mechanics from computational fluid dynamics based on intravital microscopy images," *Comput. Biol. Med.*, vol. 106, pp. 1–11, 2019.

8. APPENDICES

8.1. User Defined Functions

8.1.1. Velocity Profile

8.1.1.1. Steady Parabolic Flow

```
#include"udf.h"

DEFINE_PROFILE(velocity, thread, position)
{
	/* the centroid of the boundary face (x0,y0,z0) */
	real x0 = 0.0;
	real y0 = 0.0;
	real z0 = 0.0;
	/* the maximum radius of the pipe and maximum centerline veloicty of the parabola */
	real Max_Radius = 0.00488; /* diameter of the pipe Max_Radius */
	real Peak_Velocity = 0.1388; /* maximum centerline velocity of the parabola
	/*****************************/
	/* Main Program */
	/*****************************/
	real x[ND_ND]; /* this will hold the position vector of the face/element centroid */
	real r; /* distance from the centre of the pipe */
	real Velocity_Profile; /* Velocity to be written to boundary */
	face_t f; /* f the hooked boundary face in fluent */
	begin_f_loop(f, thread)
	{
		F_CENTROID(x, f, thread); /* the coordinates of the current face/element centroid
		accessed by F_CENTROID */
		/* Radius from central axis of parabola is */
		if (ND_ND == 2) /* for 2D modelling */
		{
			r = pow(pow((x[0] - x0), 2) + pow((x[1] - y0), 2), 0.5);
		}
		if (ND_ND == 3) /* for 3D modelling */
		{
			r = pow(pow((x[0] - x0), 2) + pow((x[1] - y0), 2) + pow((x[2] - z0), 2), 0.5);
		}
		/* Write Profile in x */
		Velocity_Profile = Peak_Velocity * (1.0 - ((r * r) / (Max_Radius * Max_Radius)));
		/* Write velocity boundary condition */
		F_PROFILE(f, thread, position) = Velocity_Profile; /* Apply velocity profile to
selected boundary */
	}
	end_f_loop(f, thread)
}
```

8.1.1.2. Pulsatile Parabolic Flow

```
#include"udf.h"

DEFINE_PROFILE(velocity, thread, position)
{
	/* the centroid of the boundary face (x0,y0,z0) */
	real x0 = 0.0;
	real y0 = 0.0;
	real z0 = 0.0;
	real time = CURRENT_TIME;
	/* the maximum radius of the pipe and maximum centreline velocity of the parabola */
	real Max_Radius = 0.00488; /* diameter of the pipe Max_Radius */
	real peakV = (0.083*sin((7.8*time)+5.3)+0.022*sin((15.6*time)+5.8)+0.01*sin((7.8*time)+5.33))+0.06;
	real Peak_Velocity ;
	/*****************************/
	/* Main Program */
	/*****************************/
	real x[ND_ND]; /* this will hold the position vector of the face/element centroid */
	real r; /* distance from the centre of the pipe */
	real Velocity_Profile; /* Velocity to be written to boundary */
	face_t f; /* f the hooked boundary face in fluent */
	begin_f_loop(f, thread)
	{
		F_CENTROID(x, f, thread); /* the coordinates of the current face/element centroid accessed by F_CENTROID */
		if (peakV >= 0.0)
		{
			Peak_Velocity = peakV;
		}
		else
		{
			Peak_Velocity = 0.0;
		}

		/* Radius from central axis of parabola is */
		if (ND_ND == 2) /* for 2D modelling */
		{
			r = pow(pow((x[0] - x0), 2) + pow((x[1] - y0), 2), 0.5);
		}
		if (ND_ND == 3) /* for 3D modelling */
		{
			r = pow(pow((x[0] - x0), 2) + pow((x[1] - y0), 2) + pow((x[2] - z0), 2), 0.5);
		}
		/* Write Profile in x */
		Velocity_Profile = Peak_Velocity * (1.0 - ((r * r) / (Max_Radius * Max_Radius)));

		/* Write velocity boundary condition */
		F_PROFILE(f, thread, position) = Velocity_Profile; /* Apply velocity profile to selected boundary */
	}
	end_f_loop(f, thread)
}
```

8.1.1.3. Pulsatile Parabolic Flow with Valve Activity

```
#include"udf.h"

DEFINE_PROFILE(velocity, thread, position)
{
   real x0 = 0.0;
        real y0 = 0.0;
        real z0 = 0.0;
   real time = CURRENT_TIME;
   real Max_Radius = fabs(((0.083*sin((7.8*time)+5.3)+0.022*sin((15.6*time)+5.8)+0.01*sin((7.8*time)+5.33))+0.12)*(0.00488/0.1319419967782473));
        real Peak_Velocity;
   real x[ND_ND];
        real r;
        real Velocity_Profile;
   face_t f;
   begin_f_loop(f,thread)
        {
        F_CENTROID(x, f, thread);
        r = pow(pow((x[0]-x0),2)+pow((x[1]-y0),2)+pow((x[2]-z0),2),0.5);
        if (r > Max_Radius)
           {
           Peak_Velocity=0.0;
           }
        else
        {
                real peakV = (0.083*sin((7.8*time)+5.3)+0.022*sin((15.6*time)+5.8)+0.01*sin((7.8*time)+5.33))+0.06;
           if (peakV >= 0.0)
                {
                        Peak_Velocity = peakV;
                }
                else
                {
                        Peak_Velocity = 0.0;
```

```
                }
        }
        Velocity_Profile = Peak_Velocity*(1.0-((r*r)/(Max_Radius*Max_Radius)));

        F_PROFILE(f, thread, position) = Velocity_Profile;
        }
         end_f_loop(f, thread)

}
```

8.1.2. Thrombin Generation Profile

```
DEFINE_PROFILE(AneurysmWall,th,i)
{
 #if !RP_HOST
 face_t a;
 real h = 2.7272e0;
 real PEAK = 200.0e0;
 real TTP = 1.95e0;
 real ETP = 1648.0e0;
 real Line = ((-14540*CURRENT_TIMESTEP)+93550);  /* To be Recalculated for every geometry. This is for timestep size less than 1*/
 real Factor = (PEAK)/Line;
 begin_f_loop(a,th)
   {
            F_PROFILE(a,th,i)          =          (h*PEAK*exp(-h*((CURRENT_TIME/60.0e0)          - TTP))*(PEAK/ETP)*exp(-exp(-h*((CURRENT_TIME/60.0e0) - TTP))*(PEAK/ETP)))*Factor ;
/*
           if (CURRENT_TIME==0){
                  F_PROFILE(a,th,i)    =    (1e-09*h*PEAK*exp(-h*((CURRENT_TIME/60.0e0)    - TTP))*(PEAK/ETP)*exp(-exp(-h*((CURRENT_TIME/60.0e0) - TTP))*(PEAK/ETP)));  }

          else {
```

```
                F_PROFILE(a,th,i)    =    (1e-09*h*PEAK*exp(-h*((CURRENT_TIME/60.0e0)    -
TTP))*(PEAK/ETP)*exp(-exp(-h*((CURRENT_TIME/60.0e0)                                    -
TTP))*(PEAK/ETP)))/(CURRENT_TIMESTEP*153.0);   }
*/        }
 end_f_loop(a,th)
 #endif
}
```

8.1.3. Biochemicals Initialization

```
DEFINE_INIT(my_init_func, d)
{
        cell_t c;
        Thread* t;
        real xc[ND_ND];  /* loop over all cell threads in the domain */
        thread_loop_c(t, d)      /* loop over all cells */
        {
                begin_c_loop_all(c, t)
                {
                        C_CENTROID(xc, c, t);
                        C_UDSI(c, t, 1) = 7000.0; // all cells have 7000 nM of fibrinogen
                        C_UDSI(c, t, 2) = 0.0; ; // all cells initially have zero fibrin
                }
                end_c_loop_all(c, t)  } }
```

8.1.4. Fibrin Formation

```
DEFINE_SOURCE(Source_of_UDS2, c, t, dS, eqn)
{
        real kcat = 59.0;
        real Km = 3160.0;
        real Fnmax = 10000.0;
        real source2;
        real Fbng = C_UDSI(c, t, 1);
        real Thr  = C_UDSI(c, t, 0);
        real Fbrn = C_UDSI(c, t, 2);
        real gen =1050.0*kcat * Thr * Fbng / (Km + Fbng);
        if (Fbrn < Fnmax)
                source2 = gen;
        else
```

```
        source2 = 0.0;
    return source2;
}
```

8.1.5. Fibrinogen Consumption

```
DEFINE_SOURCE(Sink_of_UDS1, c, t, dS, eqn)
{
    real source1;
    real kcat = 59.0;
    real Km = 3160.0;
    real Fbng_min = 0.1;
    real Thr =  C_UDSI(c, t, 0);
    real Fbng = C_UDSI(c, t, 1);
    real Fbrn = C_UDSI(c, t, 2);
    real gen = 1050.0*kcat * Thr * Fbng / (Km + Fbng);
    if (Fbng > Fbng_min)
        source1 = (-gen);
    else
        source1 = 0.0;
    return source1;
}
```

8.1.6. Viscous Resistance

```
DEFINE_PROFILE(vis_resx, t, nv)
{
    real b;
    cell_t c;
    begin_c_loop(c, t)
    {
        //if (C_UDSI(c,t,0) >= 1.00e-9 && C_STRAIN_RATE_MAG(c,t) <= 100.0e0)
        if (C_UDSI(c, t, 3) != 1e0)
            b = 1.0e-12;
        else
            b = 1.0e+12;
        C_PROFILE(c, t, nv) = b;
    }
    end_c_loop(c, t)
}
```

8.1.7. Porosity Function

```
DEFINE_PROFILE(porosity_function, t, nv)
{
        real f;
        cell_t c;
        begin_c_loop(c, t)
        {
                real dudy;
                real dvdx;
                real visc;
                real stress;
                real fibrin;
           visc=C_MU_L(c,t); // using this instead of visc value just to try it
                dudy=C_DUDY(c,t);
                dvdx=C_DVDX(c,t);
                stress=visc*(dudy*dudy+dvdx*dvdx);
                if (C_UDSI_M1(c, t, 3) == 1.0)
                {
                        f = 0.75e0;
                        C_UDSI(c, t, 3) = 1.00e0;
                }
                else
                {
                        if (C_UDSI(c, t, 2) >= 1000.0 && stress < 5000)
                        { f = 0.75e0;
                                C_UDSI(c, t, 3) = 1.0e0;}
                        else
                        {
                                f = 1e0;
                                C_UDSI(c, t, 3) = 0e0;
                        }
                }
                C_PROFILE(c, t, nv) = f;
                // C_UDMI(c,t,0) = f;
        }
        end_c_loop(c, t)
}
```